SEMICLASSICAL TUNNELING CORRECTIONS FOR CLASSICAL DYNAMICS OF UNIMOLECULAR REACTIONS IN POLYATOMIC MOLECULES

By

YUE QIN

Bachelor of Science
Wuhan University
Wuhan, P. R. China
1982

Master of Science
Jilin University
Changchun, P. R. China
1986

Submitted to the Faculty of the
Graduate College of the
Oklahoma State University
in partial fulfilment of
the requirements for
the degree of
DOCTOR OF PHILOSOPHY
May, 1992

SEMICLASSICAL TUNNELING CORRECTIONS FOR CLASSICAL DYNAMICS OF UNIMOLECULAR REACTIONS IN POLYATOMIC MOLECULES

Thesis Approved:

Donald L. Thompson
Thesis Advisor

J. Paul Devlin

Lionel M. Raff

Paul Westhaus

Thomas C. Collins
Dean of the Graduate College

ACKNOWLEDGEMENTS

I would like to express my appreciation to my research adviser Dr. D. L. Thompson for his intelligent guidance, consistent encouragement and help in my graduate study. I would like to thank the other members of my committee, Drs L. M. Raff, J. P. Devlin and P. A. Westhaus, for taking the time to read my thesis, for their valuable suggestions and for many many helps.

I would like to thank Dr. Tommy Sewell, Candee Chambers, Ann Ratcliffe and Juan Zhang for taking time to read this thesis.

I would like to extend my thanks to my friends and colleagues who provided friendship, encouragement and sharing their knowledge through stimulating discussions, especially to Dr. Yuhua Guan, Dr. Huadong Gai, Dr. Tommy Sewell, Dr. Eric Wallis, Dr. Harold Schranz, Dr. Mel Zandler, Dr. David, Sahm, Karen Bintz, Candee Chambers, Marty Perry, Jeff Fuson, and Ann Ratcliffe.

I am grateful for the financial support throughout my graduate studies by the Department of Chemistry, the U. S. Army Research Office, and the Air Force office of Scientific Research.

I would like to express my thanks to my parents Baoshun Qin and Chaoping Zhang for their support and encouragement.

Finally, I would like to thank my wife Juan Zhang and our son Chen Qin for their love and support.

TABLE OF CONTENTS

LIST OF TABLES

LIST OF FIGURES

Figure Page

Figure Page

Figure Page

CHAPTER I

INTRODUCTION

It has been known for a long time that reactions involving hydrogen-atom transfer show different behavior than other chemical reactions. The classical theory of chemical reactions is based on the idea of an activated complex, which means that the reactants must have enough energy to surmount a potential barrier to reach the products configuration space. On the other hand, quantum mechanically, reactants with energy less than the classical threshold can tunnel through the potential barrier.

For one-dimensional problems, tunneling has been extensively studied.[1-2] The WKBJ semi-classical approximation[3] can be used to solve one-dimensional problems (analytically or numerically depending on the potential). However, one-dimensional models oversimplify real chemical processes, which are multi-dimensional. The tunneling problem is significantly more difficult for two or more dimensional systems, mainly because of the difficulty in defining the tunneling coordinate. Since all the modes of a real molecule are highly coupled, it is difficult to separate out the "tunneling coordinate". Therefore, understanding and developing new methods to treat multi-dimensional tunneling is an important challenge.

Various methods have been developed to study one-dimensional as well as multi-dimensional tunneling processes.[1-13,15-21] The variational transition-state theory (VTST),[4] is one of the more generally used methods. The method provides clear physical picture. In this method the tunneling is defined in terms of a transmission coefficient κ that is taken to be the ratio of the real quantum mechanical rate coefficient to the one obtained from a VTST calculation, which gives only the classical contribution, thus we have

$$\kappa = K_{real} / K_{VTST}, \tag{I–1}$$

where K_{real} is the real rate constant determined by a rigorous quantum mechanical calculation and K_{VTST} is the variational transition-state theory rate constant without considering tunneling. Thus, κ should take into account both tunneling and non-classical reflection. At low temperatures, however, the transmission coefficient κ, mainly accounts for the influence of tunneling.

The simplest and the most commonly used methods for approximate evaluation of tunneling effects in conventional transition-state theory were derived by Wigner[5] and Bell[6]. In both of these methods, a truncated parabola is used to approximately represent the potential energy along the minimum energy path in the neighborhood of the transition state. The transmission coefficient is obtained by Boltzmann averaging the semiclassical barrier penetration probabilities. Wigner's tunneling correction for the first-order approximation can be expressed as:

$$\kappa = 1+\frac{1}{24}\left(\frac{h\nu^*}{kT}\right)^2, \tag{I–2}$$

where k is the Boltzmann constant, T is the temperature, h is Planck's constant, and ν^* is the imaginary frequency of oscillation of a particle with effective mass m in a parabolic potential well; ν^* can be expressed as:

$$\nu^*=\frac{1}{2\pi}\sqrt{\frac{(-d^2V/dx^2)|_{x=x^*}}{m}}, \tag{I–3}$$

where $d^2V/dx^2)|_{x=x^*}$ is the second derivative of the potential energy evaluated at the transition state. If the correction is very small, less than a factor of 2 for most cases, this method is useful for approximately evaluating the tunneling contribution.

Bell,[6] in subsequent work, used another approach to the same problem to derive a more accurate expression for the tunneling correction:

$$\kappa = \frac{u^*}{2.0{*}\sin(0.5u^*)} - u^* y^{-(u^*/2\pi)}\left(\frac{y}{(2\pi - u^*)} - \frac{y^2}{(4\pi - u^*)} + \frac{y^3}{(6\pi - u^*)} - \ldots.\right), \qquad \text{(I–4)}$$

where $u^*=h\nu^*/(kT)$, $y=\exp(-E/h\nu^*)$, ν^* is the imaginary frequency defined by Eq. (I–3), and E is the barrier height for a simple parabolic potential. All the other terms are the same as in Wigner's tunneling correction, Eq. (I–2). Bell's correction has a large region of validity, but the expression is discontinuous and divergences if $u^*=2n\pi$ (n=integer number). Both Wigner's and Bell's tunneling corrections, however, oversimplify the problem. The rate constant calculated by Bell's method normally underestimates the tunneling probability due to neglect of the reaction path curvature effects.[1]

The first successful approximate expression that takes into account the effect of reaction path curvature on the tunneling probability was suggested by Marcus and Coltrin[7]. Since the imaginary component of the momenta provides a classical analogism to quantum mechanical tunneling, they introduced complex momenta into the classical mechanics to allow the trajectories to "pass through" the classically forbidden region. The vibrationally adiabatic approximation[9] was used to separate the effective Hamiltonian which describes the tunneling process. The WKBJ[3] one-dimensional tunneling treatment was employed to evaluate the tunneling probability. The tunneling probability P_{tun} is

$$P_{tun} = \frac{1}{(1+\exp(2\theta))}, \qquad \text{(I–5)}$$

where the θ is the action integral of the complex momentum

$$\theta = 2\pi\int_{s<}^{s>} 2[\mu(\,V(s) - E)]^{0.5} ds/h, \qquad \text{(I-6)}$$

s is the arc length along the tunneling path, and s> and s< are the outer and inner turning points, respectively. The V(s) is the potential along the tunneling path, E is the energy of the system, and h is Planck's constant. They searched for a path that minimizes the imaginary part of the action integral and provides the maximum of the tunneling probability for a family of curves. The optimal path was located at the concave side of the reaction path in the neighborhood of the tunneling region. This corresponds physically to the negative internal centrifugal effect. Their results are in excellent agreement with the accurate rate coefficient calculated by a rigorous quantum mechanical method, with the largest difference being only 14%.

Miller and co–workers[9-11] studied the tunneling contribution to chemical reaction by using a reaction path Hamiltonian model[9]. In their calculation, the reaction coordinate s is defined as the distance along the steepest descent path in mass-weighted Cartesian coordinates. The other internal vibrational coordinates of the system are treated by local harmonic normal modes that are orthogonal to the reaction path. The Hamiltonian of the system (for the total angular momentum equal to zero[11]) in these coordinates can be written as:

$$H=\frac{0.5\ (\ P_s - \sum_{k=1}^{3N-7}(Q_k p_{k'} B_{k,k'}(s)))^2}{(\ 1 + \sum_{k=1}^{3N-7}(Q_k B_{k,k'}(s)))^2} + V_0(s) + \sum_{k=1}^{3N-7}(0.5P_k^2 + 0.5\omega_k(s)^2 Q_k{}^2), \quad \text{(I-7)}$$

where (Q_k, P_k) (k=1, 2, ..., 3N-7) are the coordinates and momenta for the local harmonic modes perpendicular to the reaction path, $V_0(s)$ is the potential energy along the reaction path, and the function $\{B_{k,k'}(s)\}$ (k=1, 2, ..., 3N-7) describes couplings of the reaction coordinate (labeled mode k') with other vibrational modes. The primary effect of the curvature of the reaction path is the coupling of the reaction coordinate s to the other degrees of freedom. The coupling function $\{B_{k,k'}(s)\}$ may or may not be important in the tunneling calculation, depending upon the system. By incorporating this coupling function with Marcus and Coltrin[7] approximate tunneling model, the tunneling probability can be written as:

$$P_{tun}(E) = \exp(-2\theta_0)\prod_{j=1}^{3N-7}\exp[2\theta_j(E)], \qquad \text{(I–8)}$$

where $\theta_0(E)$ is the vibrationally adiabatic action integral

$$\theta_0 = 2\pi\int_{s<}^{s>}2[\mu(\ V_n(s) - E)]^{0.5}ds/h, \qquad \text{(I–9)}$$

μ is the reduced mass, s> and s< are the outer and inner turning points, respectively, and

$$V_n(s) = V_0(s) + \sum_{k=1}^{3N-7}h\omega_k(s)(\mathbf{n}_k + 0.5). \qquad \text{(I–10)}$$

The factor $\exp(-2\theta_0)$ is the zeroth-order tunneling probability. The action integrals $\{\theta_k\}$ take into account the influence of reaction path curvature:

$$\theta_j = |\int_{s<}^{s>} ds\ 2[\mu(\ V_n(s) - E)]^{0.5}\{(2n_j+1)/\omega_j(s)\}^{0.5}B_{j,F}(s)\ |. \qquad \text{(I–11)}$$

Obviously, the factor θ_j in general, increases the tunneling probability (see Eq. (I-8)). Applying this model to the well-studied $H+H_2 \longrightarrow H_2+H$ reaction in 3-dimensional space, they showed how the vibrationally adiabatic approximation can be improved by accounting for the reaction path curvature effects. When the reaction path curvature is included, the calculated tunneling probability for $H+H_2 \longrightarrow H_2+H$ reaction is less than a factor of two of the correct quantum mechanical value. However, when the reaction path curvature is neglected, the tunneling probability is a factor of 50–100 times too small compared to the quantum mechanical value. For the isomerization reaction

HNC-->HCN,[10] it was found that tunneling makes a dominant contribution to the isomerization process when energies are as much as 9-10 kcal/mol below the classical threshold. However, the nonseparable coupling elements (reaction path curvature) do not influence the tunneling rate very much.

Gray *et al.* [11] studied the tunneling in the unimolecular decomposition of formaldehyde. Large scale *ab initio* configuration interaction calculations were carried out for the decomposition of H_2CO in the gas phase on the ground-state potential energy surface. They calculated the microcanonical rate constant in the energy range near and below the classical threshold of the reaction. Their numerical results show that the decomposition rate constants are insensitive to the tunneling path curvature. The tunneling contribution was found to play an important role in the decomposition of formaldehyde. When the energy of the molecule is around 8 kcal/mol below the classical threshold, the tunneling rate is as large as to 10^5 s^{-1}.

Colwell and co-workers[12] investigated the effect of reaction path curvature for the isomerization CH_3O —> CH_2OH. In this study, they calculated the microcanonical rate constants for the three cases: (1) without tunneling, (2) with tunneling but without curvature, (3) with both tunneling and curvature. The numerical results indicate that at low temperatures, the reaction curvature plays an important role. The ratio of the thermal rate constant with and without the curvature effect is as large as 50-100 at T=100 K. However, for high temperatures the curvature effect is negligible.

Variational transition–state theory has been shown to be a very useful approach for studying of chemical reactions. Several methods have been developed by Truhlar and co-workers.[13,16-19] Skodje *et al.*[13] reported a small–curvature adiabatic approximation method. They employed a reaction path formalism to generate the curvature dependent "effective mass" which, in general, plays a role for the shortening of the tunneling path and minimizing the amount of exponential damping of the wave function in the passage through the classically forbidden region. For the collinear reactions $D+D_2 \rightarrow D_2+D$ and

$D+H_2 \rightarrow DH+H$, their results show that the small curvature approximation gives a quantitatively reliable description of tunneling processes for systems with small and intermediate reaction path curvatures. The largest deviation of transmission coefficient calculated by this approximation is less than a factor of two compared to the values obtained by rigorous quantum mechanical calculations.

The calculation of the energy splitting[14] in ammonia inversion is a challenging problem since it is very small (0.66 cm^{-1}, measured by experiment[15]). Brown *et al.*[16] used a semiclassical small-curvature adiabatic approximation to investigate this process. They determined the ground state vibrational energy level splitting for two different potential energy surfaces[15]. Both the potential energy surfaces have two symmetric minima separated by a maximum. The energy splitting ΔE caused by tunneling is 1.53 (surface I[15]) and 0.86 cm^{-1} (surface II[15]) caculated by the small-curvature approximation as opposed to 1.33 (surface I[15]) and 0.74 cm^{-1} (surface II[15]) obtained by a quantum mechanical calculation. They pointed out that the curvature effect can increase the tunneling splitting by more than 40%.

Garrett and Truhlar[17] developed the least-action ground-state tunneling method. In this method, the optimum tunneling path is obtained from a set of trial paths with a single adjustable parameter which controls the magnitude of the imaginary action. For a given pair of tunneling terminuses specified by an available system energy, the optimum tunneling path determined by a optimum parameter is the one that provides the least imaginary action and the maximum tunneling probability. They applied this method to various collinear atom-diatom systems and the results show that the least-action adiabatic approximation is useful for qualitatively estimating tunneling effects. The maximum deviation of the transmission coefficient calculated by this method is a factor of two on average when compared to quantum mechanically calculated values.

Lynch *et al.* [18] further tested the least-action and small curvature approximation methods. Again, the collinear and three-dimensional atom-diatom systems such as

H+BrH' –> HBr + H' and D + BrH–> DBr + H reactions were investigated. They showed that the small curvature approximation method leads to good agreement with accurate quantum mechanical results (the difference, in most of cases, is less than 10%). When the magnitude of the reaction path curvature increases, the small curvature method becomes worse. The least-action approximation algorithms (using either the minimum-energy path or the small curvature path as a reference path), however, give the best results in all the cases considered.

The extension of the variational transition state theory to surface problems have provided some interesting multidimensional tunneling results. Lauderdale and Truhlar[19] studied the diffusion of hydrogen atoms on the Cu (1 1 1) surface plane. Considering the phonon contribution to the tunneling, they allowed the surface copper atoms near the adatom to undergo small vibrations. They found that when the temperature is increased from 160 to 4000 K the associated Arrhenius activation energy increases from 6 to 11 kcal/mol. Additionally, they calculated the transmission coefficients using variational transition state theory with a small-curvature approximation. Their results show that the motions of the surface atoms can greatly increase the tunneling rate at the low temperature.

Rice, Raff, and Thompson[20] investigated hydrogen atom diffusion on the Si (1 1 1) surface with partial hydrogen coverage by incorporating tunneling into Monte Carlo variational phase-space theory. They assumed that the hydrogen can tunnel from continuum-to-continuum. Using a Metropolis Monte Carlo sampling technique and the WKBJ tunneling approximation, they calculated the tunneling rate of a hydrogen atom from the covalent Si-H bond to an interstitial threefold bonding site. For energies of the adatom less than the classical barrier, nine tunneling paths were calculated, and the path for the maximum tunneling probability was "counted". They found that tunneling is very important at room temperature. The tunneling rate is 275 times larger than the classical value at T=300 K. Furthermore, their results showed that the surface phonons can significantly enhance the tunneling rate.[19]

For reactions with large reaction path curvature, the adiabatic approximation breaks down. For instance, when a light atom is transferred between two heavy atoms or molecules, the reaction path curvature is large because of the path is almost a straight line. Garrett and co-workers[21] developed a large curvature algorithm to evaluate tunneling probabilities. Based on a linear reference path, the thermally averaged tunneling correction factors can be calculated directly. For a collinear atom-diatom reaction, the tunneling path assumed to be the most direct path (a straight line) connecting the reactant and product potential wells. Motion in the bound vibrational coordinate (instead of translational motion along the reaction coordinate) can also promote tunneling. Also, when the energy is the same the tunneling can occur at a wide range of geometries along the caustic parallel to the reaction coordinate from the asymptotic reactant region to the outer turning point in the adiabatic potential. They reported that this algorithm cannot only be used for ground state tunneling reactions but also be used to treat tunneling problems of an excited molecule. As an example, they examined the reactions of Cl + HBr—> HCl + Br, and Cl + HCl—> HCl + Cl . The numerical results are in excellent agreement with quantum mechanical calculations.

When the reaction coordinates involved two or more degrees of freedom the reaction path Hamiltonian model cannot be applied directly. Carrington and Miller[22] developed a reaction surface Hamiltonian approach to treat systems in which the reaction coordinates have more than one degree of freedom. The major difference between the reaction surface and the reaction path Hamiltonian theories is that the former theory is more general and also more difficult to apply than is the later theory. Instead of making the harmonic approximation for the 3N-7 degrees of freedom (in the reaction path model), they apply the harmonic approximation to m degrees of freedom (where $m \geq 2$ is the number of degrees of freedom strongly involved in the reaction) and the remainings of degrees of freedom (3N-m) are projected out on the reaction surface. They used this model to study the tunneling splitting due to the intramolecular hydrogen transfer in malonaldehyde:

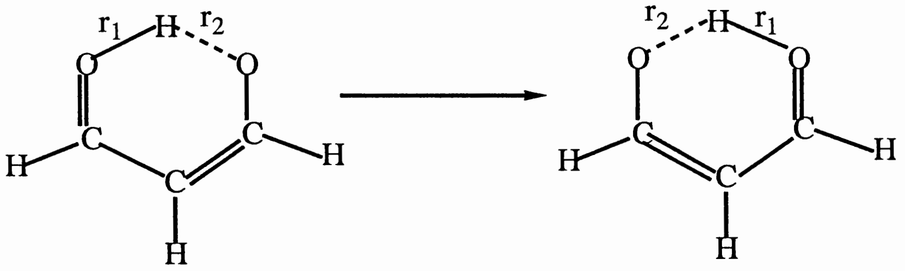

The two OH bond lengths (r_1 and r_2) are chosen as reaction coordinates and the rest of vibrational degrees of freedom are treated adiabatically by a local harmonic approximation. The two-dimensional reaction surface is constructed by minimizing the potential energy of the system with fixed values of r_1 and r_2. Instead of determining the rate of the hydrogen transfer from one well to another, they evaluated the energy difference of the two lowest vibrational states. The calculated tunneling splitting is 60 cm^{-1}, which overestimates the tunneling splitting by a factor of three (the experimental value [23] is 21 cm^{-1}) when a barrier of 4.3 kcal/mol (calculated by Frisch Scheiner Schaefer, and Binkley[24]) is used. After they rescaled the barrier height to 6.8 kcal/mol, they obtained a tunneling splitting of 17 cm^{-1}. They concluded that the barrier for the hydrogen transfer is between 6 and 7 kcal/mol.

Shida, Barbara, and Almlof[25] investigated multidimensional nuclear tunneling in malonaldehyde by using *ab initio* calculations. Three internal coordinates, two OH stretching and a OO stretching, were used to build up the reaction surface Hamiltonian. The effective tunneling path is taken to be the path with maximum probability in the classically forbidden region. They reported that when the potential barrier is 10.6 kcal/mol the calculated tunneling splitting of the ground vibrational state is 9 cm^{-1}, which is about a factor of two smaller than the experimental value[23]. The relative motion of the two oxygen atoms is found to significantly facilitate the tunneling splitting because of shortening of the tunneling path. Additionally, they found that tunneling splitting in vibrationally excited malonaldehyde is significantly larger than that of the ground state and is mode specific.

Bosch *et al.* [26] studied the hydrogen transfer in malonaldehyde and the hydrogenoxalate anion

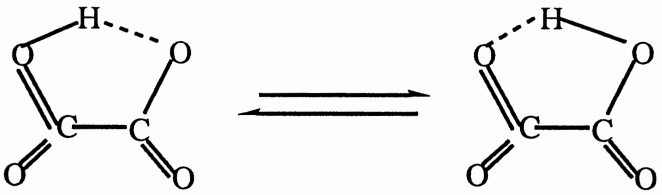

by using *ab initio* calculations. Both one-dimensional and two-dimensional model potential energy surfaces were constructed. It was found that the distance between the two oxygen atoms which are the hydrogen-donor and hydrogen-acceptor is a crucial factor for the hydrogen transfer. When the interaction between the O-O stretching motion and the hydrogen transfer motion is included, the value of the tunneling splitting is about 100 times larger than the value calculated using the one-dimensional model. The motions of the oxygen atoms can decrease the width of the effective barrier. By introducing the zero point energy, this tunneling splitting is increased another order of magnitude. In addition, they found that the tunneling splitting in malonaldehyde is greater than in hydrogenoxalate anion in all the levels of calculation. This is simply because the size of the ring through which the hydrogen transfer occurs in malonaldehyde is bigger than that of hydrogenoxalate anion.

Classical mechanics has provided a powerful method for studying the dynamics of large molecular systems[27], and by introduction of semiclassical corrections this method can be used to describe quantum mechanical tunneling effects. Waite and Miller[28] proposed a classical-plus-tunneling approach for a two-dimensional model unimolecular reaction. Whenever the trajectories encounter the classical barrier, the system is allowed to hop from one potential well to another. The local tunneling probabilities are computed by using the WKBJ approximation (Eqs. (I–5) and (I–6)). The survival probability is obtained by averaging over the vibrational phase. The results for both quantum mechanical and the classical-plus-tunneling calculations are in very good agreement.

Waite[29] extended the classical-plus-tunneling model to treat the unimolecular reaction HNC—>HCN. The vibrationally adiabatic zero-curvature approximation[8] (which assumes that all the curvature coupling coefficients $B_{k,k'}(s)$ of Eq. (I–7), are equal to zero) was employed thus the tunneling probability can be written as:

$$P_{tun}(E) = \frac{1}{1 + \exp(2\theta)}, \qquad \text{(I–12)}$$

where θ is defined by Eq. (I-9). The action integral is now a function of the reaction coordinate only. It was found that the CN stretching mode is very weakly coupled to the bending mode (which corresponds to the reaction coordinate). The results indicate that there is strong mode-specificity at low excitation energies. However, when the energy of the system is above the classical threshold, the mode-specificity is much less pronounced.

Llorente and Pollak[30] further extended the semiclassical model of Waite and Miller[28]. The step function is replaced by the tunneling probability in the microcanonical rate constant expression. Assuming the motion of the system is ergodic and translational motion is separable, then the phase space average is replaced by a time average. Incorporating the semiclassical tunneling correction into the expression for the unimolecular dissociation rate constant, they expressed the rate constant as:

$$k_{uni} = \lim_{T \to \infty} \frac{1}{T} \sum_{j=1}^{\infty} P_i, \qquad \text{(I–13)}$$

where T is the time and P_i is the individual tunneling probability which is evaluated by the WKBJ approximation[3]. They applied this model to the unimolecular decomposition of coplanar H_3^+. The computed results are in good agreement with the experimental photodissociation rates measured by Carrigton and Kennedy.[31]

Makri and Miller[32] recently developed a model for incorporating quantum mechanical tunneling into classical trajectory simulations of polyatomic molecules. The basic notion of their method is that a classical trajectory propagating in one classically allowed region of phase space will have a finite probability of tunneling to another classically allowed region of phase space and that the system will tunnel through a multidimensional barrier along a specified direction that minimizes the exponential damping of the wavefunction within the classically forbidden region. Based on representative calculations employing semiclassical wavefunctions, the tunneling direction was defined as the *shortest straight-line distance* between the initial and final states of the system. Direct application to several two-degrees-of-freedom systems designed to model prototypic unimolecular (and bi-molecular) isomerizations and unimolecular dissociation yielded good results compared to the corresponding quantum mechanical results.

The methods described above have been applied to reactions with a barrier separating the reactants and products. The reaction path curvature effect on tunneling probability has been found to be very important in many cases. For reactions with no barrier or barriers far into the reactants or products regions, it is possible to simplify the treatment of reaction path curvature. Illies and co-workers[33] proposed a tunneling model to describe the unimolecular fragmentations $CH_4^+ \longrightarrow CH_3^+ + H$ and $NH_3^+ \longrightarrow NH_2^+ + H$, which have loose transition states. They approximated the potential in the tunneling region by a dipole term plus a rotational barrier from free internal rotation of the molecular fragments and orbital rotation. This model gives a reasonable explanation of the experimental observation that a sharp increase in intensity and kinetic energy release occurs when the temperature is raised. As the orbital angular momentum is raised, the barrier changes shape from low and wide to high and narrow. This change results in an increase or decrease of the tunneling probability.

Heller and Brown[34] presented a method to estimate the energy dependence of radiationless transition rate between different electronic states of polyatomic molecules. Two electronic states the triplet state (T_1) and the singlet state (S_0) are included in their model potential energy surfaces. When the energy of the system is below the energy of the crossing point, the transition from T_1 to S_0 is classically forbidden, thus it must occur by tunneling. When the energy of the system is above the energy of the crossing point, the transition from T_1 to S_0 is determined by the Landau-Zener probability evaluated by using the Tully-Preston surface hopping method[35]. Heller and Brown pointed out that the positions of turning points in the potential energy surface dominate the tunneling, i.e., the distance between the two surfaces is a significant factor in determining the magnitude of the tunneling probabilities. The closer the two surfaces, the shorter the distance of the hydrogen transfer and the larger the tunneling probability.

The hydrogen atom transfer between a silicon atom and a water molecule is another system in which tunneling may be important. Tachibana and co-workers[36] carried out *ab initio* calculations to locate the transition state of the *trans*–HSiOH–>*cis*–HSiOH isomerization by 3-21G* basis sets. Their results show that HSiOH keeps C_s symmetry as the system goes from the reactant to the transition state. That is, the isomerization can proceed via the HOSi in–plane bending motion. The calculated activation energy is 10.79 kcal/mol at the CID+QC/6-31G**//HF/3-21G* level and 5.47 kcal/mol at HF/3-21G* level, respectively. They also reported that when the concept of tunneling instability is employed, each isomer can be described as a "cell" in the (3N-6)-dimensional mass-weighted configuration space. The "cell" of the *trans* isomer shows a much great isotope effect than does that of the *cis* isomer. The frequency difference between the *trans* and *cis* isomers of HSiOH is significantly larger than that in HSiOD. Thus, the potential energy surface is more symmetric for HSiOD than it is for HSiOH. Since the localization of the wave function is directly related to the asymmetry of the potential, the vibrational wave function of HSiOH is localized mainly in the *trans* well. This indicates that the *trans*–

HSiOH will be a dominant product. The *cis–>trans* isomerization by tunneling was found to be an important factor at low temperature.[36] This result is in good agreement with the experimental observations.[37] However, there are some disparities regarding the geometry of the transition state. Two possible isomerization pathways, the HOSi in-plane bending and internal rotation, were reported. Kudo and Nagase[38] studied isomerization of hydroxysilylene using *ab initio* calculations with a HF/631-G* basis set. The dihedral angle was identified as the isomerization coordinate with a potential barrier of 11 kcal/mol. Later, Sakai and Jordan[39] reported calculations that supported this result but caculated a potential barrier of 14.3 kcal/mol. They also reported the geometries and the vibrational frequencies of HSiOH.

Siebrand and co-workers[40] presented a different approach for studying hydrogen transfer. Considering the tunneling process to be analogous to electron transfer, they used the Golden rule to calculate the tunneling effects. In their model, the initial and final states of the transfer are taken to be vibrational eigenstates of the non-interacting reactants and products, respectively. When the coupling is turned on, hydrogen transfer can occur. The rate of transfer is proportional to the square of the matrix elements of the interaction operator between the initial and final states. Considering the adiabetic effect, they used the localized reactant and product wave functions to construct the "natural" basis set for describing the hydrogen transfer. They studied AH(D) + B—> A + H(D)B reactions, where A and B are C, N, or O atoms. They found that this model gives better quantitative results for certain types of reaction than do conventional adiabatic tunneling treatments.

There are a lot of experimental data available on tunneling effects. Miyazaki and Lee[41] studied the tunneling reaction of HD + D—> H + D_2. In this experiment, they irradiated D_2-HD mixtures and monitored the products by electron spin resonance spectroscopy. It was found that the quantity of H atoms increases gradually, while the concentration of D atoms decreases complementarily. Since the threshold energy for the reaction is about 10 kcal/mol[42], the reaction cannot proceed thermally at the temperature

(4.2 K) of the experiment. Therefore, they believe that this result is direct evidence for tunneling in the reaction.

Robie and co-workers[43] studied the tunneling effect in the O(^{3}P) + HD reaction. They used a discharge-flow/laser-induced fluorescence apparatus to measure the ratio of steady-state concentrations of OH and OD in a reactive mixture of O(^{3}P) + HD. The intramolecular kinetic isotope effect was detected for the reactions:

$$O + HD \longrightarrow OH + D \quad \text{and} \quad O + DH \longrightarrow OD + H.$$

The branching ratio of products (OH/OD) has a strong negative temperature dependence. This significant primary isotopic effect implies that tunneling plays an important role in the reaction. They suggested that tunneling dominates the rate of the reaction of O(^{3}P) + HD at temperatures below 450 K.

Carrington and Kennedy[31] investigated the unimolecular decomposition of H_3^+, D_3^+, D_2H^+, and DH_2^+. They used a beam of H_3^+ ions aligned collinear with an infrared laser beam. The center of mass kinetic energies of H_3^+, which corresponds to individual resonance lines, were measured. Many of the resonance lines are associated with a relatively small energy release. They suggested that such a small energy release is related to either rotational predissociation or tunneling through a centrifugal barrier. In addition, they obtained the lifetimes of H_3^+ and deuterated species. Llorente and Pollak[30] reported a theoretical analysis that confirms that the dissociation rate is determined by tunneling through total angular momentum barriers.

Reid and co-workers[44] studied the reaction Mu + H_2 (where Mu $=\mu^+e^-$ is an isotope of hydrogen with mass 1/9 of proton mass) over the temperature range 473–843 K. They measured the rate constants for both Mu + H_2 and Mu + D_2. It was found that the isotope effects are significant with decreasing temperature indicating large tunneling effects. Their results are in excellent agreement with accurate quantum mechanical predictions,[45] but in somewhat less agreement with results calculated by the least–action variational transition state theory.[46]

Kirchner and Bowers[47] investigated the process for loss H_2 in ion cluster H_5^+, H_5^+, H_7^+, and H_9^+ by using high-resolution reverse geometry mass spectrometry. They found that the lifetimes of the ions are about 10^{-6} s. Detailed reproducible structure was obtained in the kinetic energy distributions for the H_5^+, D_5^+, and H_7^+ ions. In addition, they developed a theoretical model for H_5^+ by combining an *ab initio* potential energy surface with a high-order WKBJ tunneling method. This model nicely reproduced the observed structure and predicted that the lifetimes of this reaction is 10^{-6} s. They suggested that the structure was due to superposition of tunneling from various bound vibrational levels of the H_3^+-H_2 stretch for different angular momentum states of the H_5^+ ion.

Wilson and co-workers[22] carried out a series of microwave spectroscopic studies of malonaldehyde. They measured the splitting of the ground state due to intramolecular tunneling between the two equivalent unsymmetric planar equilibrium configurations. Fast hydrogen transfer from one oxygen atom to another via tunneling is observed. Significant perturbations were found in the microwave spectra of a number of isotopically substituted species of malonaldehyde. The barrier height for deuterium tunneling was determined to be 4.0–5.0 kcal/mol. They also quantitatively determined the equilibrium structure of malonaldehyde by analyzing the microwave spectra of a couple of isotopic species. The tunneling splittings and rotation-vibration coupling constants were calculated for different isotopic species. They measured the energy difference due to the tunneling to be 21 cm^{-1} for the normal species. The centrifugal distortion coefficients were found to play a great role in tunneling quenching.

The *cis–trans* isomerization of HONO has been the subject of several experimental[48-50] and theoretical studies[51-56]. Baldeschwieler and Pimentel[48] first reported the infrared-induced photoisomerization of HONO in a cryogenic nitrogen matrix with light in the range 3200-3600 cm^{-1}. In their experiments, they observed large isotopic substitution effects, even $HO^{18}NO^{18}$ showed a significant mass effect on the isomerization rates. They interpreted these results as evidence for non-classical behavior. The isomerization was found to be too slow to be detected in the DONO. They suggested that tunneling may play an important role. Hall and Pimentel[49] studied the isomerization using a Nernst glower as a light source. They estimated the interconversion barrier height to be 9.7 to 10 kcal/mol. The initial rate of *cis–>trans* isomerization of HONO is about 10 times larger than that of DONO. More recently, Shirk and co-workers[50] reported experimental results for infrared laser-induced isomerizations of HONO in solid Ar and nitrogen matrices. They found that the excitation of the OH stretch in *cis*–HONO is much more effective in promoting interconversion than is OH excitation in the *trans* isomer. The isomerization rate is significantly larger (about two orders of magnitude) for the *cis–>trans* than that of *trans–>cis* conversion. This indicates that the OH stretching mode in the *cis*–isomer is more strongly coupled with the torsional coordinate than it is in the *trans*–isomer. The rate of isomerization does not depend on the temperature. Guan *et al.*[52,53] studied the intramolecular energy transfer, mode-specificity and the influence of rotation in *cis*↔*trans* isomerization of HONO by using classical trajectory methods. They found that the rate of the interconversion for the *cis–>trans* is significantly larger than the rate of the *trans–>cis*. Excitation of the HON bending mode yields the largest rate coefficient, and excitation of the OH stretching model yields the lowest rate coefficient in both *cis*↔*trans* processes. The orientation of the rotation plays an important role in the intramolecular energy transfer. The favored direction of rotating HONO in promoting the IVR is the direction which is coincidental to torsional motion. Their results are in qualitative agreement with the experimental results[48-50].

In order to gain a better knowledge of the preparation of ultrapure semiconductor materials for the electronics industry, Ismail and co-workers[37] carried out experiments of reaction of silicon atoms with water molecules in a solid argon matrix. They mixed the triplet ground state of atomic silicon $Si(^3P)$ with water. The mixture (silicon and water) quickly forms silicon-water adducts, Si:H_2O, at 15 K in the argon matrix. After 7 hours, they found that the silicon-water adducts rearranged and formed the insertion products of hydroxysilylene (HSiOH) by a hydrogen transfer process. They detected only the *trans*-isomer when H_2O was used. On the other hand, both *cis* and *trans* isomers were detected by the IR spectrum when HDO was used. They suggest that tunneling effects may be important in this reaction.

CHAPTER II

THEORETICAL METHODS

Classical Trajectories

The calculation of classical trajectories involves the numerical solution of Hamilton's equations of motion for a given potential energy surface and set of initial conditions.[27] A fourth-order Runge-Kutta-Gill integrator was employed to solve the equations of motion. The selection of initial conditions are done by Monte Carlo techniques.

Hamilton's Equations of Motion

The classical Hamiltonian for a system of N particles can be written as H=T+V, where T is kinetic energy and V is the Born-0ppenheimer potential energy. When the potential energy is not an explicit function of the velocities of the particles, the equations of motion are[57]

$$\frac{\partial H}{\partial p_i} = \dot{q}_i$$

$$-\frac{\partial H}{\partial q_i} = \dot{p}_i \qquad (i=1, 2,..., 3N), \qquad (II\text{–}1)$$

where q_i and $\dot{q}_i$ are the generalized coordinates and velocities, respectively, and p_i are the conjugate momenta of the q_i. Equations (II-1) are a set of 6N first-order differential equations. The solutions of Equations (II-1) describe the motion of the N particles in the system.

Selection of Initial Conditions

It is necessary to specify the initial values of the momenta and coordinates of the system in order to carry out the integration of Eqs. (II-1). The Monte Carlo method was used to randomly pick the initial coordinates and momenta from 6N-dimensional phase space. Since the normal mode representation is a good approximation to describe the ground state molecular vibrational energy, normal mode analyses were performed before the trajectory started. Normal mode analysis has been addressed in depth by many authors,[58,59] therefore, we only give a brief outline here. In the ground state, the deviations of the Cartesian coordinates from the equilibrium geometry are small, the potential energy therefore can be approximately represented by a quadratic form

$$V=\frac{1}{2}\tilde{\mathbf{W}}\mathbf{F}\,\mathbf{W}, \tag{II-2}$$

where the **F** is Hessian matrix with elements $f_{ij}=\frac{\partial^2 v}{\partial w_i\,\partial w_j}$, the second derivative of the potential energy surface, and **W** is a vector of the 3N mass-weighted Cartesian coordinates. Normal mode analysis is performed by finding a 3Nx3N orthogonal matrix which diagonalizes the Hessian matrix

$$\mathbf{L}^{-1}\mathbf{f}\mathbf{L} = \Lambda, \tag{II-3}$$

where Λ is a diagonal matrix with elements $\lambda_i=4\pi^2\nu_i^2$ (i=1, 2, 3, ..., 3N), which are the normal mode frequency parameters; ν_i are the normal mode frequencies. The 3N-6 non-zero eigenvalues correspond to vibrational motion; six zero eigenvalues correspond to the rotational and translational motions.

The zero-point energy assignment is accomplished by a "normal mode partition method". The energy of each normal mode can be written as

$$E_i=(n_i+\frac{1}{2})h\nu_i \qquad (i=1, 2, ..., 3N\text{-}6), \qquad \text{(II-4)}$$

where n_i is the quantum number of mode i (for the ground state $n_i=0$), h is Planck's constant and ν_i is vibrational frequency of mode i.

The initial phase of each of the normal modes was selected by using a Monte Carlo method,[27]

$$R=R_e-(R_e-\rho_-)\sin(\frac{\pi}{2}+\pi\zeta), \qquad \text{(II-5)}$$

where R_e is the equilibrium displacement, ρ_- is the classical inner turning point, and ζ is a random number between zero and one. It is computationally convenient to perform the trajectory integrations in Cartesian coordinates. Thus, we used the transformation equations between the Cartesian displacements and normal coordinates. If **Q** represents a set of orthogonal vectors of normal coordinates, the transformation from normal coordinates to Cartesian coordinates can be accomplished by

$$\mathbf{X}=\mathbf{L}\,\mathbf{M}^{1/2}\mathbf{Q}, \qquad \text{(II-6)}$$

where **L** is the eigenvector of Eq (II-3), and **M** is a diagonal matrix whose elements are the atomic masses. The potential energy is evaluated in Cartesian coordinates following the transformation of Eq. (II-6). The kinetic energy in each mode is therefore determined by subtracting the potential energy of the mode. The $\dot{\mathbf{Q}}_i$ are given by

$$\dot{Q}_i=\pm\sqrt{E_i-V_i}\,, \tag{II-7}$$

where the E_i is calculated from Eq. (II-4) and V_i is the potential energy contributed by the ith mode. Since the normal modes are separable, the zero-point energy can be partitioned into each mode independently. If the potential energy of a given mode exceeds the total energy of the mode due to the anharmonicities of the potential, the initial coordinates are rejected and the above procedure is repeated.

We wish to excite the molecule in a fashion such that it can be related to available experimental work, thus both the normal and local mode excitations were used in our calculations. Excitation energy was assigned in a way analogous to that used to assign the zero-point energy to the molecule. The energy of the excited normal mode i is determined by Eq. (II-4). The procedures of selection of the coordinates and momenta of the excited mode is the same as when we partitioned the ground state energy to the molecule. The local mode excitation is, however, different from the normal mode partition.

The energy in an excited X-H bond (X=O, Si) is calculated by a local mode approximation,[60]

$$E_k=\frac{P_{XH}^2}{2\mu}+V_{XH}\,, \tag{II-8}$$

where the μ is the reduced mass of X-H bond, the P_{XH} is the momentum of the X-H bond and is defined as:

$$P_{XH}=\frac{P_X}{m_X}-\frac{P_H}{m_H}\,. \tag{II-9}$$

The phase of the X-H bond is chosen by

$$R = R_e + \beta^{-1}\ln[\frac{1- (E_v/D_e)^{1/2}\cos(2\pi\zeta)}{1-(E_v/D_e)}], \qquad \text{(II-10)}$$

where D_e and β are the Morse well-depth and exponential parameter, respectively. The E_v is energy in the X-H bond which is calculated by Eq. (II-9). R_e is the bond length at the equilibrium configuration. Again ζ is random number with value from 0 to 1.

The process of summing the displacements and momenta along the normal mode coordinates introduces a molecular angular momentum that must be subtracted out.[61-62] Since we are more interested in the microcanonical rate, we need to fix the total energy. This is done by scaling the momenta and the coordinates by[61-62]

$$q_i' = \sqrt{\frac{E_{des}}{E_{rel}}(q_i-q_i^o)} + q_i^o \qquad \text{(II-11)}$$

and

$$\dot{q}_i' = \sqrt{\frac{E_{des}}{E_{rel}}}\ \dot{q}_i, \qquad \text{(II-12)}$$

where q_i and $\dot{q}_i$ are the Cartesian coordinates and the velocities, respectively. The E_{des} is the desired total energy, E_{rel} is the actual energy calculated from Hamiltonian of the system, and the q_i^o are the equilibrium coordinates.

An ensemble of trajectories are calculated for each set of initial conditions. The trajectories are propagated in a lab-fixed Cartesian coordinate system. The integration is performed using a fourth-order Runge-Kutta-Gill routine with a fixed stepsize of 9.78×10^{-17} s.

Classical-Plus -Tunneling Models

In order to incorporate the tunneling corrections into the classical trajectory calculations, we employed the classical-plus-tunneling model developed by Waite and

Miller.[28,29] The basic idea is that whenever a classical trajectory experiences a classical turning point in the proper "direction", a semiclassical (WKBJ) tunneling probability is calculated from the local properties of the trajectory at that instant in time. The survival probability (that is, the probability of having not tunneled) can be expressed as[28]

$$P^{i}_{surv}(t)= (1-P^{i}_{j(t)})(1-P^{i}_{j-1}).....(1-P^{i}_{2})(1-P^{i}_{1}), \tag{II-13}$$

where $P^{i}_{j(t)}$is the individual tunneling probability that the particle experiences the jth classical turning point of the ith trajectory; and j(t) is the number of the turning points which has happened in that trajectory by the time t. In the case of a classically reactive trajectory (that is, one that crosses over the top of the barrier), the survival probability for all times subsequent to reaction is identically zero.

When the tunneling probability is small, i.e., $P_j<<1$, Eq. (II-13) is numerically difficult to evaluate, so it is computationally convenient to calculate the cumulative tunneling probability $P_{tun}(t)$:

$$P_{tun}(t) = 1- P_{surv}(t). \tag{II-14}$$

The relationship between P_{tun} and P_j is

$$P_{tun}=\sum_{j=1}^{N}P_j(1-P_{j-1})(1-P_{j-2})(1-P_{j-3})...(1-P_2)(1-P_1). \tag{II-15}$$

Averaging over the initial phase of the vibrational motion in the reactant well, we can write the average survival probability as:

$$<P_{surv}(t)>=1-<P_{tun}(t)>. \tag{II-16}$$

The tunneling probability P_k is given by the WKBJ approximation[3]

$$P_k = \frac{1}{(1+\exp(2\theta_k))}, \tag{II-17}$$

where the θ_k is the classical action integral through the classically forbidden barrier region,

$$\theta_k = \mathrm{Im}\, \frac{2\pi}{h}\int_{x<}^{x>} p(x)dx. \tag{II-18}$$

The variable of integration in Eq. (II-18) denotes the arc length along the tunneling path, p(x) is the component of the momentum along the path, h is the Planck's constant, and x< and x> are the classical turning points. In a purely classical rate calculation, the P_k is equal to 1 when the particle crosses over the barrier and zero otherwise.

How to find the tunneling path and how to evaluate the individual tunneling probability along the path, P_j, is the critical part of this semiclassical approach. The most rigorous treatment would be to integrate the classical equations of motion along the classically forbidden region for which the particle tunnels through the potential barrier.[63] However this method is much more complicated to implement. In order to simplify this problem one has to introduce approximations, such as a sudden approximation[64] (which assumes that the phase space variables perpendicular to the tunneling degree of freedom remain frozen during the tunneling process), vibrationally adiabatic zero curvature[9] (which primarily assumes that the curvature couplings between the 3N-7 vibrational degrees of freedom and the tunneling degree of freedom are zero), and other approaches.[13,16-18].

Makri and Miller[32] recently developed a model by using the "tunneling direction" approach. The key part of this method is to select the correct tunneling path which is guided by the tunneling direction. Based on representative calculations employing semiclassical wavefunctions, the tunneling direction is defined as the *shortest straight-line distance* between the initial and final states of the system. However, it is difficult, in practice, to visualize the "*shortest straight-line distance*" between the two configurations (*cis* and *trans* for example) in the full-dimensional potential energy surface when the system involves more than three degrees of freedom. An alternative way to deal with such a system is to assume separability of the tunneling modes from the rest of the vibrational modes (vibrationally adiabatic zero curvature approximation) during the tunneling process. When there are no potential couplings between the tunneling mode and the rest of the vibrational modes, the direction of tunneling is naturally along the direction of the tunneling coordinate. In this case, the tunneling direction in the Waite-Miller[28] method is coincident with that in the Makri-Miller[32] approach.

The Hamiltonian of the system in internal coordinates may be written as:[59]

$$H=\frac{1}{2}\Sigma\Sigma p_j G_{jk} p_k + V(r_1, r_2, r_3, \ldots r_n) \qquad (n=1,2,\ldots,3N-6), \qquad \text{(II-19)}$$

where the p_j and p_k are the conjugate momenta of the internal coordinates, r_j, r_j and G_{jk} are the Wilson G-matrix elements.[58,59] That is, whenever a trajectory experiences a maximum or minimum in the motion along the tunneling coordinates we exploit the assumed vibrational motion separability between the system Hamiltonian and the Hamiltonian describing the tunneling process and write the latter by the reaction path formula as:

$$H_\alpha = p_\alpha G_{\alpha\alpha} p_\alpha + V_0(\alpha) + \sum_{i=1}^{3N-7}(n_i+\frac{1}{2})\frac{h\omega_i(\alpha)}{2\pi}, \qquad \text{(II-20)}$$

where α represents the tunneling coordinate and the $G_{\alpha\alpha}$ is the Wilson G-matrix element for the internal coordinates α; p_α is the momentum conjugate to the α, and $V_0(\alpha)$ is the potential along the reaction coordinate. The $\{n_i\}$ are the quantum numbers that describe the rest of the 3N-7 degrees of the freedom normal to the tunneling coordinate and the $\omega_i(\alpha)$ are the frequencies which is a function of the tunneling coordinate. If we write the effective energy along the tunneling coordinate as:

$$V_{eff}(\alpha) = E - \sum_{i=1}^{3N-7}(n_i+\frac{1}{2})\frac{h\omega_i(\alpha)}{2\pi}, \qquad \text{(II–21)}$$

where the E is the total energy of the system, the tunneling integral has the form:

$$\theta_k = \frac{2\pi}{h}\int_{\alpha<}^{\alpha>} d\alpha \sqrt{2G^{-1}_{\alpha\alpha}(V_0(\alpha) - V_{eff}(\alpha))}\ , \qquad \text{(II-22)}$$

where $\alpha<$ and $\alpha>$ correspond to the outer and inner classical turning points, respectively. Of course, the G-matrix element for the tunneling coordinate, $G_{\alpha\alpha}$, and $V_{eff}(\alpha)$ are normally functions of the time and the tunneling coordinate. The classical trajectories are propagated by using the full Hamiltonian in Cartesian representation; the approximate Hamiltonian in Eq. (II-20) is used for evaluating an approximate tunneling probability only.

The calculated tunneling probability is averaged over the vibrational phase of the tunneling coordinate to minimize the statistical fluctuations. The cumulative tunneling probability function $P_{tun}(t)$, Eq. (II-15), versus time t is simply a "stepping function". A sketche of the typical form of $P^{i}_{j(t)}$ is shown in Fig. 1.

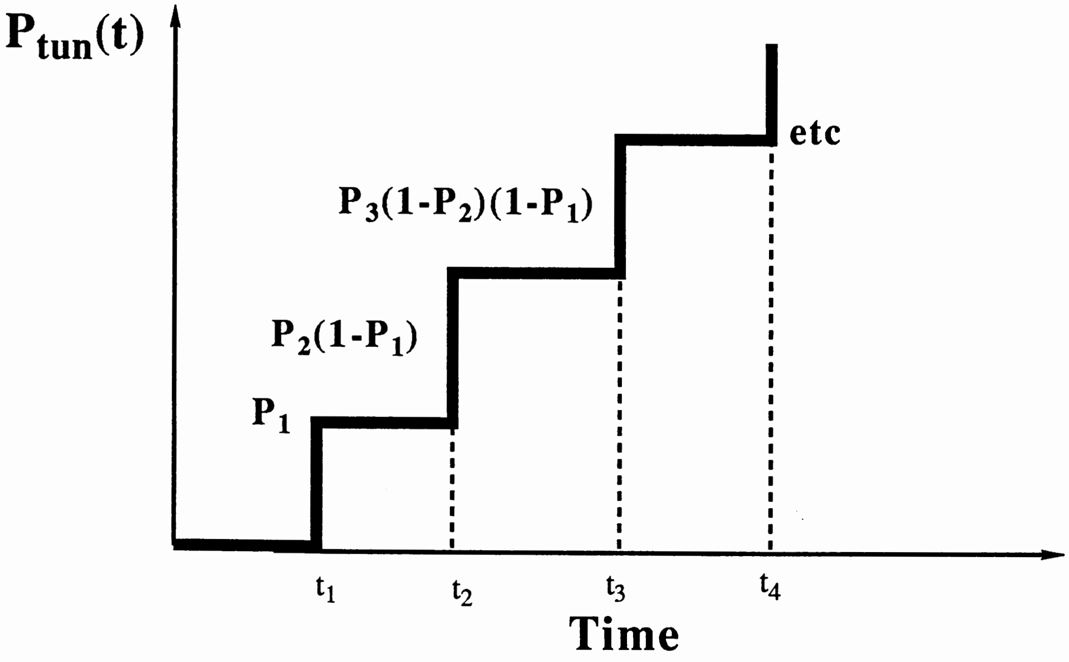

Figure 1. Sketch of the Cumulative Tunneling Probability.

The $P^{i}_{tun}(t)$ can be written as:

$$P^{i}_{tun}(t) = \sum_{j=1}^{N} \phi^{i}_{\varphi}\,\eta(t-t^{i}_{tun}(t)), \tag{II-23}$$

where the quantity ϕ^{i}_{j} is defined by

$$\phi^{i}_{j} = P^{i}_{j}(1-P^{i}_{j-1})(1-P^{i}_{j-2})(1-P^{i}_{j-3})\ldots\ldots(1-P^{i}_{2})(1-P^{i}_{1}), \tag{II-24}$$

and the η is the unit step function defined by

$$\eta(t) = \begin{cases} 1 & t>0 \\ 0 & 0<t\ . \end{cases} \tag{II-25}$$

By using the time average over the tunneling coordinate and Monte Carlo average over the 3N-7 degrees of freedom which are perpendicular to the reaction coordinate, the average tunneling probability is obtained by[28,29]

$$\langle P_{tun}(t)\rangle = \frac{1}{N}\sum_{i=1}^{N}\frac{1}{t^{i}_{1}}\int_{0}^{t^{i}_{1}} (P^{i}_{tun}(t+t'))dt', \tag{II-26}$$

where N is the total number of trajectories and t^{i}_{1} is the time required for the first turning point. The solution of Eq. (II-26) is arrived at by introducing the following function:

$$\zeta_j^i(t)=\frac{1}{t_1^i}\int_0^{t_1^i} h(t+t'-t_j^i)dt' = \begin{cases} 1 & t > t-t_j^i \\ 1+(t-t_j^i)/t_1^i & t_k^i - t_1^i < t < t_j^i \\ 0 & t<t_j^i - t_1^i \end{cases} \qquad \text{(II-27)}$$

so that the average tunneling probability is given by

$$<P_{tun}(t)> = \frac{1}{N}\sum_{i=1}^{N}\sum_{k=1}^{M}\zeta_k^i(t)\phi_k^i(t). \qquad \text{(II-28)}$$

The evaluation of the average survival probability, Eq. (II-16), is now given by Eq. (II-28).

The purely classical unimolecular rate calculation is analogous to the above except that the tunneling probabilities $\{P_{tun}(t)\}$ are set equal to 1 when the trajectory crosses over the top of the barrier and 0 otherwise. Thus, Eq. (II-16) is reduced to

$$< P_{surv}(t) > = 1- <P_{tun}(t)> =1- \frac{1}{N}\sum_{i=1}^{N}\zeta^i(t), \qquad \text{(II-29)}$$

where the $\zeta^i(t)$ is defined by

$$\zeta^i(t)=\frac{1}{t_1^i}\int_0^{t_1^i} h(t + t'- t^i)dt' = \begin{cases} 1 & t > t - t^i \\ 1+(t-t^i)/t_1^i & t^i - t_1^i < t < t^i \\ 0 & t< t^i - t_1^i \end{cases} \qquad \text{(II-30)}$$

t_1^i is, as above, the time for the first oscillation along the tunneling direction at the turning point.

Intramolecular Energy Transfer

It is most convenient to integrate the equations of motion in lab-fixed Cartesian coordinates. However, we are interested in calculating quantities in physically meaningful internal coordinates so that we can "see" directly how the bond lengths and angles change and how the energy flows from bonds to bonds, from bonds to angles, and from angles to angles, *etc*. Thus, we need to find the transformation from the Cartesian coordinates to the internal coordinates.

Let s_k represent an internal coordinate. The general relation between the time derivative of s_k and the Cartesian velocities can be written as:

$$\dot{s}_k = \sum_{j=1}^{3N} \frac{\partial s_k}{\partial q_j} \dot{q}_j \qquad (k=1, 2, ..., 3N-6), \qquad \text{(II-31)}$$

where the $\{q_j\}$ are the Cartesian coordinates and the $\{\dot{q}_j\}$ are the Cartesian velocities. It is easy to recognize that the derivative of the internal coordinate s_k with respect to the Cartesian coordinate q_j is exactly the well-known B-matrix element.[58,59] If we use $\dot{\mathbf{s}}$ to represent the vector whose components are the velocities of internal coordinates and $\dot{\mathbf{q}}$ for the vector whose components are the velocities of Cartesian coordinates, Eq. (II-31) can be written in matrix notation:

$$\dot{\mathbf{s}} = \mathbf{B}\,\dot{\mathbf{q}}, \qquad \text{(II-32)}$$

where the **B** is the B–matrix whose elements are the derivatives of the internal coordinates with respect to the Cartesian coordinates. Note that the B-matrix is not, in general, a square matrix but has dimensions (3N-6,3N). Thus, it cannot be inverted. In order to get the inverse of **B**, we used Blom and Pulay's approach.[65] Let **A** denote a (3N,3N-6) matrix and **I** denote a (3N-6,3N-6) unit matrix whose off-diagonal elements are zero and all the diagonal elements are one. It is easy to construct a matrix **A** with the property

$$\mathbf{BA} = \mathbf{I}(3N\text{-}6,3N\text{-}6) \tag{II-33}$$

by

$$\mathbf{A} = \mathbf{UB}'(\mathbf{BUB}')^{-1}, \tag{II-34}$$

where **U** is a (3N,3N) unitary matrix (can be any unitary matrix, in practice, we used the inverse of the masses matrix $\mathbf{M}^{-1}$). Obviously matrix **A** is a (3N,3N-6) matrix. The vector $\dot{\mathbf{q}}$ can be obtained by projection of the vector $\dot{\mathbf{s}}$ to matrix **A** and written as:

$$\dot{\mathbf{q}} = \mathbf{A}\dot{\mathbf{s}}. \tag{II-35}$$

The potential energies in general are written in the forms of the internal coordinates in our calculation.[66] The expressions of the kinetic energies in terms of internal coordinates are accomplished by introduction of Eq. (II-32). Let T denote the kinetic energy of the system, and again let **M** denote a diagonal matrix whose elements are the atomic masses, total kinetic energy T can then be written as:

$$T = \frac{1}{2}(\dot{\mathbf{q}})'\mathbf{M}\dot{\mathbf{q}}\,, \tag{II-36}$$

where $\dot{\mathbf{q}}'$ is the transpose of Cartesian velocities $\dot{\mathbf{q}}$. Substituting Eq. (II-35) into Eq. (II-36) we have

$$T = \frac{1}{2}(\mathbf{A}\dot{s})'\mathbf{M}(\mathbf{A}\dot{s}) = \frac{1}{2}\dot{s}'\mathbf{A}'\mathbf{M}\mathbf{A}\dot{s} = \frac{1}{2}\dot{s}'(\mathbf{A}'\mathbf{M}\mathbf{A})\dot{s}, \qquad \text{(II-37)}$$

where the matrix (**A'MA**) is actually equal to the inverse of the G-matrix,[58,59] which is correlated to the kinetic couplings of the system. We write the total energy of the system in the internal coordinate representation as:

$$E = \sum_{i=1}^{3N-6}\sum_{k=1}^{3N-6}(\dot{s}_i G^{-1}_{ik}\dot{s}_k + V(s_i,s_k)), \qquad \text{(II-38)}$$

where the $\{V(s_i,s_k)\}$ are the potentials in terms of the internal coordinates. There is no approximation in the derivation, so Eq. (II-38) is an accurate expression for both the kinetic and total energies of the system, and it is not restricted to small displacements. Thus Eq (II-38) is valid even for highly excited molecules. In practice, it is fairly easy to implement this analysis because the quantities required are only the first derivatives of the internal coordinates with respect to the Cartesian coordinates and the derivatives are calculated when the equations of motion are propagated.

Equation (II-38) can be divided into two parts:

$$E_{ii} = \sum_{i=1}^{3N-6}(\dot{s}_i G^{-1}_{ii}\dot{s}_i + V(s_i,s_i)) \qquad \text{(II-39)}$$

and

$$E_{ik} = \sum_{i=1}^{3N-6}\sum_{k=1}^{3N-6}(\dot{s}_i G^{-1}_{ik}\dot{s}_k + V(s_i,s_k)) \quad (i \neq k), \qquad \text{(II-40)}$$

where the E_{ii} represents the summation of all the diagonal terms of Eq. (II-38) and E_{ik} represents the summation of all the off-diagonal terms of Eq. (II-38). Obviously, the sum of the E_{ii} and E_{ik} is equal to total energy of the system. It is usually assumed that the off-diagonal of equation (II-38) is small and can be ignored. We found that the energies calculated by using E_{ii} Eq. (II-39) are about 10-25% off the true values (which is the sum of the E_{ii} and E_{ij}). However, it is a reasonable approximation to consider each diagonal term of Eq. (II-39) as the energy in that internal coordinate when the values of the diagonal terms are significantly larger than the off-diagonal terms. Therefore, the energy in the ith internal coordinate is approximately

$$E_i = 0.5\ \dot{s}_i G_{ii}^{-1} \dot{s}_i + V(s_i, s_i), \qquad \text{(II-41)}$$

where the s_i are internal coordinates corresponding to bond stretching, in-plane bending , out-of-plane wagging, and torsions. $V(s_i,s_i)$ is the potential energy for the ith internal coordinate.

Recently a new approach was developed by Raff[67] for monitoring intramolecular energy transfer. The method is based on the idea of projection of the instantaneous Cartesian velocities onto the normal mode vectors. Thus, the kinetic energy of the system is diagonalized by a set of 3N normal coordinates. The rate of the mode-to-mode energy transfer can be obtained by examining the "envelope function" of the individual mode kinetic energy.

Constrained Trajectories

The rate of the intramolecular energy transfer is an important factor in determining the magnitude of the tunneling probability. It is helpful to understand the details of the intramolecular energy transfer pathways and the *cis–trans* isomerization rates of HONO. To do this, we constrained certain modes to determined their influence. Constrained classical trajectories were calculated using methods which are discussed in detail elsewhere,[27] therefore, we only briefly outline the methods here.

Lagrange's equations of motion for an N-atom system are[57]

$$\frac{\partial L}{\partial q_i} - \frac{d}{dt}\left(\frac{\partial L}{\partial \dot{q}_i}\right) = 0 \qquad (i=1, 2, ..., 3N), \qquad \text{(II-42)}$$

where L is the Lagrangian of the system, q_i are the coordinates, and $\dot{q}_i$ are the velocities. The displacements ∂q_i in Eq. (II-42) are independent. The k constraints can be expressed as:

$$dA_j = \sum_{i=1}^{3N}\left(\frac{\partial A_j}{\partial q_i} dq_i\right) = 0 \qquad (j=1, 2, ..., k), \qquad \text{(II-43)}$$

where A_j is the jth constraint condition. Thus the ∂q_i are no longer independent variables. Therefore Lagrangian equations of motion with k constraints are given by

$$\frac{\partial L}{\partial q_i} - \frac{d}{dt}\frac{\partial L}{\partial \dot{q}_i} + \sum_{j=1}^{k} \sigma_j a_{ji} = 0 \qquad (i=1, 2, ..., 3N), \qquad \text{(II-44)}$$

where the σ_j are the Lagrangian multipliers and $a_{ji} = \frac{\partial A_j}{\partial q_i}$. Consequently, Hamilton's equations of motion with k constraints are

$$\left\{ \begin{aligned} \frac{\partial H}{\partial P_i} &= \dot{q}_i \\ -\frac{\partial V}{\partial q_i} + \sum_{j=1}^{k} \sigma_j a_{ji} &= \dot{P}_i \end{aligned} \right. \qquad \text{(II-45)}$$

The quantities of σ_j must be evaluated at every integration step. Differentiating Eq. (II-43), with respect to time gives

$$\sum_{i=1}^{3N} a_{ji}\,\ddot{q}_i + \sum_{i=1}^{3N} \dot{a}_{ji}\dot{q}_i = 0. \qquad \text{(II-46)}$$

Incorporating Eqs. (II-45) and (II-46) and using the fact that $\ddot{q}_i = \frac{\dot{P}_i}{m_i}$ (for the Cartesian coordinates) gives

$$\sum_{j=1}^{k} \sigma_j \sum_{i=1}^{3N} \frac{a_{ji}a_{li}}{m_i} - \sum_{i=1}^{3N} \frac{a_{ji}}{m_i}\frac{\partial V}{\partial q_i} + \sum_{i=1}^{3N} \dot{a}_{ji}\dot{q}_i = 0. \qquad (l=1, 2, \cdots, k). \qquad \text{(II-47)}$$

Thus the σ_j can be determined by solving a set of k linear equations.

In this study, we are interested in the effects of constraining either the torsional or one of the bending motions. That is, either τ or θ_i are held constant. The constraint condition therefore can be written as:

$$\frac{dA}{dt} = \sum_{i=1}^{12} \left(\frac{\partial A}{\partial q_i}\right) \dot{q}_i = 0, \qquad \text{(II-48)}$$

where $A=\tau$ or θ for the cases of torsional and bending constraints, respectively. Since we have only one constraint condition,the Lagrangian multiplier σ, from Eq (II. 47) is

$$\sigma = \frac{\left\{ \sum_{i=1}^{12} \frac{a_i}{m_i}\frac{\partial V}{\partial q_i} - \sum_{i=1}^{12} (\dot{a}_i \dot{q}_i) \right\}}{\left(\sum_{i=1}^{12} \frac{a^2_i}{m_i} \right)}, \qquad \text{(II-49)}$$

where $a_i = \frac{\partial A}{\partial q_i}$. Using the chain rule, the value of $\dot{a}_i$ can be evaluated

$$\dot{a}_i = \sum_{j=1}^{12} \frac{\partial^2 A}{\partial q_i \partial q_j} \dot{q}_j . \qquad \text{(II-50)}$$

When the dihedral angle is equal to zero or π, directly evaluating a_i and $\dot{a}_i$ leads to singularities. In order to circumvent this problem, we required that cos(ß)=constant (ß=τ, or θ) for the constraint condition. Furthermore, in order to evaluate Eq (II. 50), we need to calculate the second derivatives of the dihedral or bending angle with respect to the Cartesian coordinates at every integration step. This requires a large amount of CPU time. However, since we are interested in constraining the dihedral angle to its equilibrium value (0 or 180^0), we need only to require that the four atoms remain in a plane. Thus, the constraint condition can be expressed as:

$$\mathbf{r}_{N=O}\cdot(\mathbf{r}_{N-O}\mathrm{x}\mathbf{r}_{O-H})=0, \qquad \text{(II-51)}$$

rather than cos(τ)=1 (for *cis*) or cos(t)=-1 (for *trans*) where

$$\cos(\tau) = \frac{(\mathbf{r}_{N=O}\mathrm{x}\mathbf{r}_{N-O})\cdot(\mathbf{r}_{N-O}\mathrm{x}\mathbf{r}_{O-H})}{r^2_{N=O} r_{N-O} r_{O-H} \sin(\theta_{ONO})\sin(\theta_{HON})} . \qquad \text{(II-52)}$$

Using Eq. (II-51) rather that Eq. (II-52) significantly reduces the computation time. For the bending constraint, we require that cos(θ)=constant for the same reason.

Finally, Hamilton's equations of motion with a constraint are:

$$\begin{cases} \dfrac{\partial H}{\partial P_i} = \dot{q}_i \\[2ex] -\dfrac{\partial V}{\partial q_i} + \sigma a_i = \dot{P}_i \end{cases} \qquad \text{(II-53)}$$

where $a_i = (\frac{\partial A}{\partial q_i})$.

In the calculations described below, the constrained equations of motion Eq.(II-53) were numerically integrated.

Rate Constants

In computing the isomerization rates we choose a critical value for the reaction coordinate in order to determine the lifetime of the product. The lifetime of the molecule for the classical calculation is taken to be the time when the trajectory experiences the last inner turning point before it surmounts the potential barrier. The distribution of lifetimes can be fitted to the first-order equation[27]

$$\ln(N_t/N_0) = -kt, \tag{II-54}$$

where N_t is the number of "nonreactive trajectories" at time t and N_0 is the total number of trajectories in the ensemble. The isomerization rate coefficient k(E) is obtained by taking the slope of the $\ln(N_t/N_0)$ versus time plot.

The tunneling decay rate is calculated in a similar way. We assumed that the isomerization processes obeyed the first-order rate law. Therefore the rate constant k can be obtained by fitting the tunneling decay curve to the following equation:

$$\ln(1-\langle P_{tun}(t)\rangle)=-kt, \tag{II-55}$$

where $\langle P_{tun}(t)\rangle$ is the averaged tunneling probability.

When the isomerization of HSiOH was studied, the rate coefficients for the two isomerization channels, HOSi bending and internal rotation, were defined analogous to the classical case.[68,69] We computed the ratio of the average survival probability via HOSi in-plane bending, $<P_{HOSi}>$, and out-of-plane torsion, $<P_{\tau}>$. The ratio of the individual tunneling rate is correlated to the total decay rate in the following manner:

$$\frac{k_{HOSi}}{k_{\tau}} = \frac{<P_{HOSi}>}{<P_{\tau}>}, \tag{II-56}$$

$$k = k_{HOSi} + k_{\tau}, \tag{II-57}$$

where k_{HOSi} and k_{τ} are the rate coefficients for isomerization via HOSi bending and internal rotation, respectively.

Power Spectra

Power spectra were used to characterize intramolecular dynamics.[70] The motion of the classical trajectories is transformed from time domain to frequency domain since the qualitative behavior of dynamics is easier to analyze in the frequency domain. The spectra of quasiperiodic trajectories show a small number of sharp and isolated peaks, while those of chaotic trajectories have a large number of perks resulting in a "grassy" spectra.

The normalized autocorrelation function for a general dynamical variable of a classical trajectory is defined as[71]

$$C(\delta) = \frac{\int_0^{T->\infty} <\chi(t)><\chi(t+\delta)>\, dt}{\int_0^{T->\infty} <\chi(t)><\chi(t)>\, dt}, \tag{II-58}$$

where $\chi(t)$ is chosen as an individual internal coordinate (such as bond length, angle, dihedral, etc.), δ is a time interval, the variables $<\chi(t)>$ and $<\chi(t+\delta)>$ are the values of the time history (with the mean removed) at time t and t+δ respectively, and T is the observation time.

The power spectra were obtained by Fourier transformation of the autocorrelation function[71]

$$I(\nu) = \int_{-T}^{T} \chi(\delta)\exp(-i2\pi\nu\delta)\, d\delta, \qquad \text{(II-59)}$$

where ν is the vibrational frequency and T is the length of the trajectory. Since C(δ) is an even function[72], the integral of Eq. (II-59) can be replaced by the corresponding cosine Fourier transformation, with the result being multiplied by a factor of two. Equation (II-59) is evaluated by Simpson's algorithm.

CHAPTER III

POTENTIAL ENERGY SURFACES

A potential energy surface is essential for molecular dynamics calculations.[27] Great progress in quantum chemistry has led to accurate *ab initio* calculations of the potential energy surfaces for various systems.[73] However, calculations are very difficult and expensive for large molecules. An alternative way to get the potential energy surface is by using empirical or semi-empirical methods. This requires some physical intuition and chemical knowledge. A good potential energy surface should be able to display the available experimental and theoretical information such as spectroscopic data, the activation energy, the bond dissociation energies, and both of the equilibrium and the transition state geometry parameters. This is the principle to be followed when the potential energy surface is constructed. The experimental vibrational frequencies are used in deriving the valence force field which is directly related to the potential energy surface. The potential energy is described by a set of the internal coordinates because the internal coordinate representation is more physically meaningful than the Cartesian coordinate representation. The available experimental and theoretical results such as the initial values of the force constants, vibrational frequencies, and the molecular symmetry are used as initial "guessing" parameters. The least squares algorithm is adapted to our code[66] to adjust those parameters until the best fitting force constants are obtained. After the valence force field is determined, we selected a set of analytical potential function forms. The Morse potential is normally used to describe the bond stretch, the harmonic potential is employed to depict the in-plane-bending motions, and the truncated cosine series is used to describe the out-of-plane waging and the torsional motions to avoid the singularities of the first and second derivatives of the internal coordinates with respect to the Cartesian coordinates[66]. The parameters of those potential functions are determined by the force constants, bond dissociation energies, potential barrier heights, and both equilibrium and transition state geometries.

In order to make the potential energy smoothly change between reactants and products configurations, switching functions are employed. *Ab initio* calculations can provide guidance about changes in the force field along the reaction coordinate.[74] However, such calculations are expensive and sometimes not available. Alternatively, we choose some known types of switching functions which have been shown to provide correct asymptotic limits and reasonable prescriptions of the changes of the force constants.

HONO Isomerizations

The potential-energy surface used in this study is based on one by Guan and co-workers[52-53]. The three bond stretches are described by Morse potentials,

$$V_{stretch}(r_i) = \sum_{i=1}^{3} D_i\{1.0-\exp[-\alpha_i(r_i-r_i^0)]\}^2, \qquad \text{(III-1)}$$

where the D_i are the depths of the potential wells, r_i^0 are the equilibrium bond lengths, and α_i are the Morse parameters which are given by:

$$\alpha_i = \sqrt{\frac{2k_i}{D_i}}, \qquad \text{(III-2)}$$

where k_i are the force constants.

The two in-plane bending motions are depicted by harmonic functions:

$$V_{bend}(\theta_i) = \frac{1}{2}\sum_{i=1}^{2} k_i(\theta i-\theta_i^o)^2, \qquad \text{(III-3)}$$

where the θ_i^o are the equilibrium bending angles and k_i are bending force constants.

The torsion potential is represented by a truncated cosine series which are obtained by fitting to *ab initio* results,[52]

$$V_{torsion} = \sum_{i=0}^{5} a_i \cos(i\tau). \qquad \text{(III-4)}$$

The values of the geometry and potential parameters are given in Tabs. I and II of Guan *et al.*[52] except that the scale factors are obtained from Tab. I of Ref. 53.

A normal mode analysis was performed to get the fundamental vibrational frequencies. The frequencies calculated and measured are listed in the Tab II of Guan *et al*, Ref. 53.

Thompson's group[52,53] has done a series of studies of the intramolecular vibrational energy redistribution (IVR), *cis–trans* isomerizations and a single bond rupture reaction (to give HO + NO) in HONO. One of the principal conclusions of those investigations is that the IRV and isomerization rates are relatively independent of the potential. They claimed that the kinetic couplings played a dominant role in both IVR and isomerization processes. Thus, we have chosen a simple potential that neglects all the switching functions in our calculations.

Coffin and Pulay[55] reported an *ab initio* study of HONO recently. Fourth-order Moller-Plesset perturbation theory was employed to calculate the geometries, quadratic force fields and fundamental vibrational frequencies of *cis*- and *trans*- HONO. They also determined the force constants matrix along the *cis-trans* interconversion path. However, this data was not available at the time of our calculations.

HSiOH Isomerizations

Tachibana *et al.*[36] studied the *cis*→*trans* isomerizations of HSiOH and HSiOD by using IRC (intrinsic reaction coordinate) as a unique reaction coordinate. The HOSi bending coordinate was found to coincide with the reaction coordinate. Applying the concept of tunneling instability, they classified each isomer as a "cell" in the (3N-6)-dimensional mass-weighted configuration space. The "cell" of *trans*–isomer showed a much more significant isotope effect than the "cell" of *cis*–isomer due to the fact that the frequency difference between the *trans*–isomer and *cis*–isomer of HSiOH is significantly larger that that of HSiOD. Thus the potential energy surface is more symmetric for HSiOD than that for HSiOH. The localization of the wave function is directly related with the asymmetry of the potential, the vibrational wave function of HSiOH was found to be mainly localized in the *trans*-well. This indicates that *trans*-HSiOH is a dominant product. The *cis*–>*trans* isomerization by tunneling is found to be important at low temperature.

The potential-energy surface of HSiOH was constructed by using available experimental data such as fundamental vibrational frequencies, equilibrium geometries for both *cis* and *trans* configurations, force fields, and theoretical results.[36-39] Several papers report the equilibrium geometric parameters for *cis*-HSiOH and *trans*-HSiOH.[36-39] The structures used here were obtained from the *ab initio* calculations of Kudo and Nagase[38]. The geometric parameters are listed in Table I.

TABLE I

EQUILIBRIUM GEOMETRIES OF *CIS* AND *TRANS* HSiOH

Coordinate		*cis*-HSiOH[a]	*trans*-HSiOH[a]
Bond (Å):			
	Si-O	1.647	1.651
	O-H	0.947	0.948
	Si-H	1.526	1.508
Angle (deg):			
	HSiO	120.0	115.4
	SiOH	98.1	96.1
	HSiOH	0.0	180.0

a. T. Kudo and S. Nagase, ref. 38

We used the harmonic valence force field reported by Ismail and co-workers[37] to fit the normal mode frequencies, which are given by the Refs. 37 and 39, for *cis* and *trans* HSiOH, respectively. Since the off-diagonal force constants are relatively small with respect to the diagonal terms, we simply ignored all of the off-diagonal terms and re-adjusted the diagonal force constants until a set of force constants, which provided the best "matching" for both normal mode eigen-vectors and eigen-values, were obtained by the least squares fitting procedures.[66] The calculated normal frequencies are listed in Table II.

TABLE II

NORMAL MODE FREQUENCIES FOR HSiOH

vibrational mode	c-HSiOH expt[a]	c-HSiOH this work	t-HSiOH expt[b]	t-HSiOH this work
ν_1(O-H)	3655	3654	3650	3651
ν_2(Si-H)	1862	1862	1882	1873
ν_3(HSiO)	949	952	937	966
ν_4(Si-O)	817	863	850	846
ν_5(HOSi)	745	714	772	722
$\nu_6(\tau)$	607	607	595	595

a. The data taken from ref. 37.
b. The data taken from ref. 39.

The bonds stretches are represent by the Morse oscillator,

$$V_{\text{stretch}} = \sum_{j=1}^{3} D_{ej}[1-\exp(-\alpha_j(r_j-r_j^0))]^2, \qquad \text{(III-5)}$$

where the D_{ej} are the bond dissociation energies, α_j are the curvature parameters, and r_j^0 are the equilibrium bond lengths. The values of the dissociation energies, D_{ej}, of the three different kinds of bonds (H-Si, Si-O and O-H) were obtained from Guan[52], Walsh[75], and the thermodynamic enthalpy data for similar molecules.[76]

The HSiO bending potential is written as an harmonic oscillator,

$$V_{\text{HSiO}} = \frac{1}{2} k(\theta-\theta^0)^2, \qquad \text{(III-6)}$$

where the k is the force constant, and the θ^0 is the equilibrium value of the angle.

The torsional potential is represented by a six-terms cosine series,

$$V_{torsion} = \sum_{i=0}^{5} a_i \cos(\tau), \qquad \text{(III–7)}$$

where a_i are the coefficients determined by fitting the torsional frequencies, the location of the transition state (τ=94.1°), and the barrier height for the internal rotation. The dihedral angle is represented by τ. The value of the barrier height 11 kcal/mol was adapted from the *ab initio* calculation reported by Kudo and Nagase.[38] All the Morse potential parameters, HSiO bending force constant and the coefficients for the torsional potential are shown in Table III.

TABLE III

POTENTIAL PARAMETERS FOR STRETCH, BEND AND TORSION OF HSiOH

Morse potential Bond		*cis*-HSiOH	*trans*-HSiOH
	Si-O	111.2	111.2
D_e (kcal/mol)	O-H	79.0	79.0
	Si-H	70.0	70.0
	Si-O	1.5955	1.6798
α (Å^{-1})	O-H	2.6062	2.6043
	Si-O	1.4294	1.4377

HSiO Bending force constant (kcal/mol deg^{-2})	*cis*-HSiOH	*trans*-HSiOH
	155.5943	150.1092

Torsional potential parameters (kcal/mol)

a_0	a_1	a_2	a_3	a_4	a_5
5.1262	-0.1673	-5.3991	0.4211	0.4004	-0.1262

There have been some disparities regarding the reaction coordinate of the isomerization. Two possible reaction pathways, either the HOSi in-plane bend or the internal rotation, were reported. Kudo and Nagase[38] studied isomerization of hydroxysilylene by using *ab initio* calculations with HF/631-G* basis set. The dihedral angle was identified as the reaction coordinate with the minimum-energy-path; the potential barrier was calculated as 11 kcal/mol. Sakai and Jordan[39] also reported that the isomerization of HSiOH involved the rotational transition state, that potential barrier was, however, 14.3 kcal/mol.

Tachibana and co-workers[36] carried out the *ab initio* calculations in an effort to locate the vibrational transition state of the isomerization of *trans*-HSiOH–>*cis*-HSiOH with 3-21G* basis sets. Their results showed that HSiOH retained C_s symmetry[58,59] when the "reactant" approached the transition state. That is, the isomerization can be accomplished via the HOSi in-plane bending potential. The calculated activation energy is 10.79 kcal/mol by the CID+QC/6-31G**//HF/3-21G* and 5.47 kcal/mol by HF/3-21G*, respectively.

Since both HOSi in-plane bend and the out-of-plane torsion can lead to isomerization, the potential opens two "reaction" channels, HOSi in-plane bend and out-of-plane torsion. *Ab initio* calculations[38] indicated that the energy difference between the *cis*-configuration and *trans*-configuration is small, about 0.5 kcal/mol. Thus, we equally partitioned the 0.5 kcal/mol into the HOSi bend and torsional wells. That is, the energy difference in the bending potential for the *trans*-well is 0.25 kcal/mol lower than that for the *cis*-well. The torsional potential was treated the same as the HOSi bending potential. Consequently, the energy of the *cis*-well is 0.25 kcal/mol higher than that of *trans*-well for the torsional potential.

The HOSi bend is represented by an eleven term polynomial of θ'_{HOSi},

$$V_{HOSi} = \sum_{i=0}^{10} b_i(\theta'_{HOSi})^i \qquad \text{(III-8)}$$

where b_i are the coefficients of the polynomials determined by best fitting both of the normal mode frequencies and the barrier height of the HOSi bending potential. The angle θ'_{HOSi} is defined as

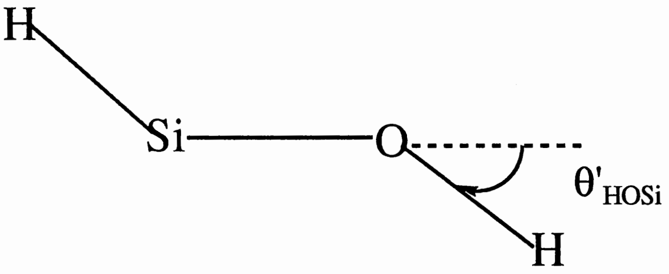

The potentials (in kcal/mol) for both the torsional and HOSi bends are plotted in Figs. 2 and 3 respectively, the units are kcal/mol. We should note that the transition state reported in Ref. 36 is located at θ_{HOSi}=176.4°. In a trial calculation, we did not observe isomerization for trajectories initiated in the *cis*-well surmounting the HOSi bending potential to the *trans*-well due to the centrifugal force which will be discussed in chapter IV. On the contrary, we found that some of trajectories initiated in the *trans*-well cross transition state via HOSi in-plane bend to the *cis*-well when the "true" transition was located θ_{HOSi}=176.4°. This result seems aphysical. Therefore, we assumed that the transition state is located at θ_{HOSi}=180°. We believed that this small "shift" made the potential more reasonable and physically correct. The coefficients for the HOSi bending potential are listed in Table IV.

TABLE IV

HOSi BENDING POTENTIAL PARAMETERS[a]

b_0	b_1	b_2	b_3	b_4	b_5
10.79	0.0	-21.8502	2.5560	13.0446	-5.0402
b_6	b_7	b_8	b_9	b_{10}	
0.0002	3.2216	-2.3254	-0.7262	0.6552	

a. Units are kcal/mol.

Two kinds of switching functions are used for smoothly attenuating the potential and geometrical parameters from reactant to product configurations. When the variable of the switching function is a dihedral angle, the switching function employed is of the form[53]

$$S_\tau=0.5*[1.0 - \cos(\tau)], \qquad \text{(III-9)}$$

where the τ is the dihedral angle. The S_τ takes care of changes of the instantaneous value of the potential parameters $Y((Y=\alpha_i$, and r_i^0 $i=1,3)$, and $\theta^0_{HOSi})$. The new potential parameters now are function of the dihedral angle with the form

$$Y_i=(Y^0{}_{cis})_i+[(Y^0{}_{trans})_i -(Y^0{}_{cis})_i]S_\tau, \qquad \text{(III-10)}$$

where the superscript 0 represents the equilibrium values and the $\{Y_i\}$ are the potential parameters defined previously.

When the switching function is a function of the bond length, a form which has been used for several molecular dynamics simulations[74] is selected,

$$Sr_i=1-\tanh[(a(r_i-r_i^0)(r_i-b)^8] , \tag{III-11}$$

the parameters are defined as $a=1.5313681\times10^{-7}$ Å^{-9}, and B=4.6696246 Å. The value of r_i^o is determined by Eq. (III-10).

The HSiO bending force constant is attenuated by the internuclear distances of adjacent bond ,i and j, and the dihedral angle,

$$k_{HSiO}=Sr_iSr_j\{(k^0_{cis})_{HSiO}+[(k^0_{trans})_{HSiO}-(k^0_{cis})_{HSiO}]\}S_\tau], \tag{III-12}$$

where the $(k^0_{cis})_{HSiO}$ and $(k^0_{trans})_{HSiO}$ are the HSiO bending force constants at the equilibrium geometries for the *cis*– and *trans*-HSiOH, respectively. The switching function, Sr_i, is defined by Eq. (III-11).

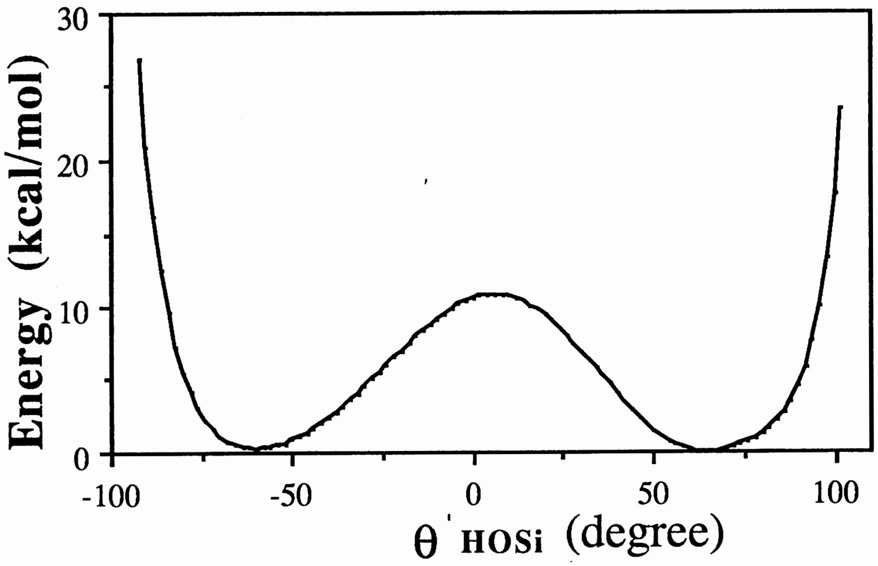

Figure 2. The HOSi Bending Potential for HSiOH.

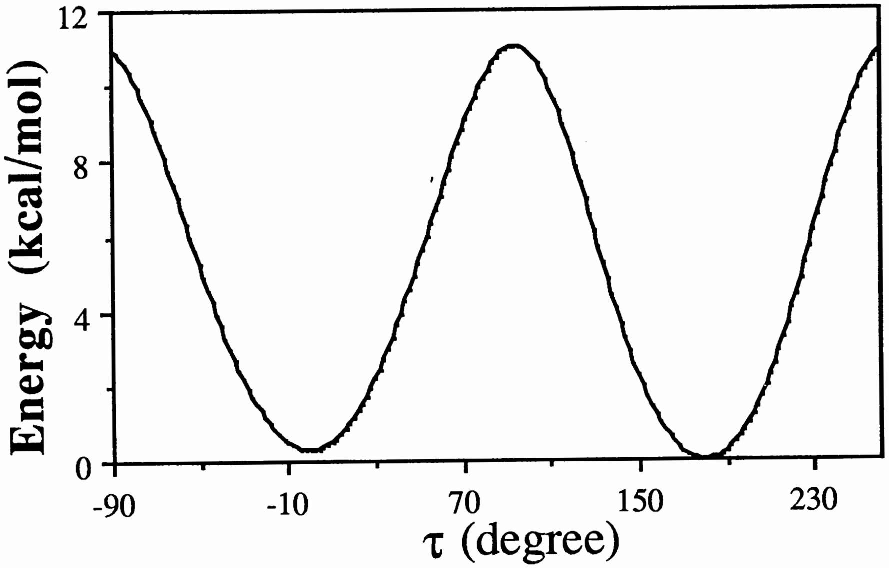

Figure 3. The Torsional Potential for HSiOH.

CHAPTER IV

SEMICLASSICAL TREATMENT OF TUNNELING EFFECTS IN HONO ISOMERIZATION

Classical trajectories have been carried out to study tunneling effects in HONO *cis–trans* isomerization, mode specificities, and intramolecular energy transfer. We calculated the classical and classical-plus-tunneling unimolecular isomerization rate coefficients as a function of total energy and initial distribution of energy. Several factors such as the effective mass of the tunneling coordinate, the rate of the energy flow into the tunneling coordinate and the tunneling frequency were investigated. The mechanism of the energy transfer for the highly excited HONO was also studied.

It is usually assumed that a problem associated with classical chemical dynamics calculations is the aphysical flow of the vibrational zero-point energy (ZPE). The argument is that the ZPE is not quantum mechanically available to contribute to the reaction rate directly, but it does contribute classically.[60,77-78] Thus, there is a concern that in reactions with low barriers classical flow of ZPE can lead to rates that are unrealistically high. The zero-point energy of HONO is about 12 kcal/mol, while the classical barriers to *cis–>trans* and *trans–>cis* isomerization are only 8.6 and 9.2 kcal/mol, respectively. Excitation of the OH stretching normal node to n=1 results in a total energy of 22 kcal/mol, over twice that required to surmount the barriers to isomerization. There is as yet no entirely suitable means of classically restricting the ZPE flow,[78] although methods have been proposed.[60,77-78] In the present study we focus on the effects of various initial energy distributions on tunneling. Our work can be divided into two parts. In the first we partitioned all the zero-point-energy into the molecule and then selectively excited the different modes of the molecule to study the way the tunneling rate was correlated with the mode that was excited. We also investigated the correlation between the excitation energy and the tunneling rate for the same initial condition in which the excitation energy is "equally" partitioned into all the vibrational modes except the reaction coordinate. In the second part of study we partition only a quarter of the ZPE into the system. Then we did similar calculations to those done in the first part so that we could circumvent the ZPE arguments to some extent. Of course, we realized that the second part this work was only a model calculation because we artificially removed most of the ZPE from the system. In reality the zero-point-energy of the molecule is an intrinsic attribute of the system and it is not removable.

The system Hamiltonian of HONO in the internal coordinates system can be expressed by[58,59]

$$H=\frac{1}{2}\sum_{j=1}^{12}\sum_{k=1}^{12}p_jG_{jk}p_k+V(r_{N=O}, r_{N\text{-}O}, r_{O\text{-}H}, \theta_{ONO}, \theta_{HON}, \tau) \qquad \text{(IV-1)}$$

where variables p_j, s_j, and G_{jk} are the same as Eq. (II-19). The potential, $V(r_{N=O}, r_{N\text{-}O}, r_{O\text{-}H}, \theta_{ONO}, \theta_{HON}, \tau)$, is the summation of the individual potential terms which were defined by Eqs. (III-1) to (III-4). We assumed that the vibrational zero curvature (VAZC) approximation[9] could be applied. Therefore, whenever a trajectory experiences a local extreme (minimum or maximum) in the motion along the dihedral angle, τ, we exploit the assumed separability between the system Hamiltonian and the Hamiltonian describing the reaction coordinate and write the latter as

$$H_\tau=p_\tau G_{\tau\tau}p_\tau + V(r_{N=O}, r_{N\text{-}O}, r_{O\text{-}H}, \theta_{ONO}, \theta_{HON}, \tau) \qquad \text{(IV-2)}$$

where $G_{\tau\tau}$ is Wilson G matrix element for the torsional motion, p_τ is the momentum conjugate to the dihedral angle τ. Since the potential used has no couplings, Eq. (IV. 2) can be simplified as

$$H_\tau = p_\tau G_{\tau\tau} p_\tau + V(\tau) \tag{IV-3}$$

where $V(\tau)$ is the torsional potential defined by Eq. (III-4). The tunneling integral can then be written as

$$\theta_k = \frac{2\pi}{h}\int_{\tau<}^{\tau>} d\tau \sqrt{2G_{\tau\tau}^{-1}(V(\tau) - E_\tau)} \tag{IV-4}$$

where the E_τ is the effective energy in the torsional mode, and its value can be evaluated by using the Eq. (IV-3). and $\tau<$ and $\tau>$ correspond the inner and outer classical turning points in the torsional direction. The G-matrix element for torsional motion, $G_{\tau\tau}$, can be represented as a function of the internal coordinates of the molecule.[71,72] The tunneling probability is then calculated by Eq. (II-17).

$$\begin{aligned}G_{\tau\tau} = {} & \left(\frac{1}{r_{N=O}\sin(\theta_{ONO})}\right)^2\left(\frac{1}{m_O}+\frac{1}{m_N}\right) + \left(\frac{1}{r_{H\text{-}O}\sin(\theta_{HON})}\right)^2\left(\frac{1}{m_H}+\frac{1}{m_O}\right)\\ & + \frac{1}{r^2_{N\text{-}O}}[\cot^2(\theta_{ONO})+\cot^2(\theta_{HON})]\left(\frac{1}{m_O}+\frac{1}{m_N}\right)\\ & + \frac{2\cos(\tau)}{r^2_{N\text{-}O}}\cot(\theta_{ONO})\cot(\theta_{HON})\left(\frac{1}{m_O}+\frac{1}{m_N}\right)\\ & - \frac{2\cos(\tau)}{r_{N\text{-}O}}\left[\frac{\cot(\theta_{HON})}{r_{O=N}\sin(\theta_{ONO})m_N}+\frac{\cot(\theta_{ONO})}{r_{H\text{-}O}\sin(\theta_{HON})m_O}\right]\\ & - \frac{2}{r_{N\text{-}O}}\left[\frac{\cot(\theta_{ONO})}{r_{O=N}\sin(\theta_{ONO})m_N}+\frac{\cot(\theta_{HON})}{r_{H\text{-}O}\sin(\theta_{HON})m_O}\right] \qquad \text{(IV-5)}\end{aligned}$$

It is obvious from Eq. (IV-5) that,

$$\begin{aligned}G_{\tau\tau} = {} & A(r_{N=O},r_{N\text{-}O},r_{H\text{-}O},\theta_{ONO},\theta_{HON}) +\\ & B(r_{N=O},r_{N\text{-}O},r_{H\text{-}O},\theta_{ONO},\theta_{HON})*\cos(\tau) \qquad \text{(IV-6)}\end{aligned}$$

where

$$\begin{aligned}A(r_{N=O},r_{N\text{-}O},r_{H\text{-}O},\theta_{ONO},\theta_{HON}) = {} & \left(\frac{1}{r_{N=O}\sin(\theta_{ONO})}\right)^2\left(\frac{1}{m_O}+\frac{1}{m_N}\right) +\\ & \left(\frac{1}{r_{H\text{-}O}\sin(\theta_{HON})}\right)^2\left(\frac{1}{m_H}+\frac{1}{m_O}\right) + \frac{1}{r^2_{N\text{-}O}}[\cot^2(\theta_{ONO})+\cot^2(\theta_{HON})]\left(\frac{1}{m_O}+\frac{1}{m_N}\right)\\ & - \frac{2\cot(\theta_{ONO})}{r_{N=O}r_{N\text{-}O}\sin(\theta_{ONO})m_N} - \frac{2\cot(\theta_{HON})}{r_{H\text{-}O}r_{N\text{-}O}\sin(\theta_{HON})m_O} \qquad \text{(IV-7)}\end{aligned}$$

and

$$B(r_{N=O},r_{N\text{-}O},r_{H\text{-}O},\theta_{ONO},\theta_{HON}) = \frac{2}{r^2_{N\text{-}O}}\cot(\theta_{ONO})\cot(\theta_{HON})\left(\frac{1}{m_O} + \frac{1}{m_N}\right)$$

$$- \frac{2\cot(\theta_{HON})}{r_{N=O}r_{N\text{-}O}\sin(\theta_{ONO})m_N} - \frac{2\cot(\theta_{ONO})}{r_{H\text{-}O}r_{N\text{-}O}\sin(\theta_{HON})m_O} \qquad \text{(IV-8)}$$

Ab initio calculations of the HONO torsional potential indicate that the bond lengths and bond angles do not change significantly along the minimum energy profile for rotation about the dihedral angle.[51] We assumed that all internal coordinates were fixed except the dihedral angle, (which is by definition the tunneling path) along the tunneling path. Further, numerical examination revealed that the value of the second term of the Eq.(IV-6) was negligible. Consequently, we were able to treat $G_{\tau\tau}$ as a constant along the tunneling path.

An Approximate Solution to the WKBJ Integral

The WKBJ tunneling integral [Eq. (IV-4)] can be evaluated numerically by using many means, for instance, Simpson's rule. However, this is quite expensive computationally. Thus we developed a more efficient means of calculating Eq. (IV-4). Realizing that Eq. (IV-4) is directly proportional to the "area" under the torsional potential (between the two isoenergetic turning points) we desired to find an approximation to the actual torsional potential Eq. (III-4) such that Eq. (IV-4) can be solved analytically.

The torsional potential was approximated by the quartic polynomial

$$V(\tau) \approx V_{app}(x) = a_0 + a_2x^2 + a_4x^4, \qquad \text{(IV-9)}$$

where $x=\tau-\tau^*$, τ^* =85.44 degree (the location of the maximum in the torsional potential), and a_0 is the barrier height, and a_2 and a_4 are adjusted to give the best fit to the actual torsional potential in the region of the barrier. After substituting Eq. (IV-9) into Eq. (IV-4) we have

$$\theta_k \approx \frac{2\pi}{h}\int_{x<}^{x>} dx \sqrt{2G^{-1}_{\tau\tau}[V_{app}(x) - E_\tau]} \qquad \text{(IV-10)}$$

where x< and x> correspond to the inner and outer turning points along the approximation potential, respectively.

Substitution of x by $y=\sqrt{\frac{2a_4}{a_2}}\,x$, Eq. (IV-10) becomes

$$\theta_k \approx c\int_{y<}^{y>} dy\sqrt{f-2y^2+y^4} \qquad \text{(IV-11)}$$

where $c=\frac{a_2}{2a_4}\sqrt{\frac{a_2}{G_{\tau\tau}}}$, $f=\frac{4a_4(a_0-E_\tau)}{a_2^2}$, and y< and y> are the corresponding inner and outer tunneling points. Let $a^2=(1+\sqrt{1-f})$, and $b^2=(1-\sqrt{1-f})$. It is easy to show that $(a^2-y^2)(b^2-y^2)=f-2y+y^4$. There are four roots available for equation $f-2y+y^4=0$, when $|f|<1$. They are $y_1=\sqrt{1+\sqrt{1-f}}$, $y_2=\sqrt{1-\sqrt{1-f}}$, $y_3=-\sqrt{1+\sqrt{1-f}}$, and $y_4=-\sqrt{1-\sqrt{1-f}}$. It is obvious that the roots y_2 and y_4 correspond to the outer and inner turning points of the potential, respectively. Substituting $y=b(\sin(q))$ into Eq. (IV. 11), we have

$$\theta_k \approx c\int_{y<}^{y>} dy\sqrt{(a^2-y^2)(b^2-y^2)} = 2cb^2a\int_0^{\pi/2}\sqrt{(1-\frac{b^2}{a^2}\sin^2(q))\cos^2(q))}\;dq \qquad \text{(IV-12)}$$

When the value of f is significantly smaller than 1, then

When the value of f is significantly smaller than 1, then

$$\sqrt{1-f} = 1 - \frac{1}{2}f - \frac{1}{8}f^2 - \frac{3}{48}f^3 - \frac{15}{384}f^4 - \ldots\ldots \qquad \text{(IV-13)}$$

and

$$\left(\frac{b}{a}\right)^2 = \frac{2-f-2\sqrt{1-f}}{f} = \frac{2-f-2(1-\frac{1}{2}f - \frac{1}{8}f^2 - \frac{3}{48}f^3 - \frac{15}{384}f^4 - \ldots\ldots)}{f}$$

$$= \frac{1}{4}f + \frac{3}{24}f^2 + \frac{3}{48}f^3 + \frac{15}{192}f^4 + O(f^5) \ldots\ldots \qquad \text{(IV-14)}$$

Since $|\sin(q)|<1$, and $f<<1$(our assumption), Eq. (IV-12) can be expanded in a Taylor series:

$$\theta_k \approx 2cb^2a\int_0^{\pi/2}\cos^2(q)\{1-\frac{1}{2}[(\frac{b}{a})^2\sin^2(q)] - \frac{1}{8}[(\frac{b}{a})^2\sin^2(q)]^2$$

$$- \frac{3}{48}[(\frac{b}{a})^2\sin^2(q)]^3 - \ldots\ldots\}dq \qquad \text{(IV. 15)}$$

Substituting Eq. (IV-14) into Eq. (IV-15) and integrating Eq. (IV-15), we finally get Eq. (IV-16) by expanding b^2a in a Taylor series:

$$\theta_k \approx \left(\frac{2\pi}{h}\right)\frac{\pi(a_0-E\tau)}{\sqrt{2G_{\tau\tau}a_2}}\left(1+\frac{3}{32}F+\frac{35}{1024}F2+\frac{1929}{196608}F3+\ldots\ldots.\right) \qquad \text{(IV-16)}$$

where $F=4a_4(a_0-E_\tau)/a_2^2$. The values of the coefficients in Eq. (IV-16) are: a_0=9.21628 kcal/mol, a_2= 0.35396 kcal/mol, a_4=0.097833 kcal/mol.

Thus, the tunneling integral of Eq. (IV-4) is represented approximately by an simple polynomial expression, and is easily evaluated. Note that the solution is only turning point, we can determine the value of E_τ and $G_{\tau\tau}$ by Eqs. (IV-3) and (IV-5) respectively. The tunneling integral can be evaluated by Eq. (IV-16) with negligible computational expense.

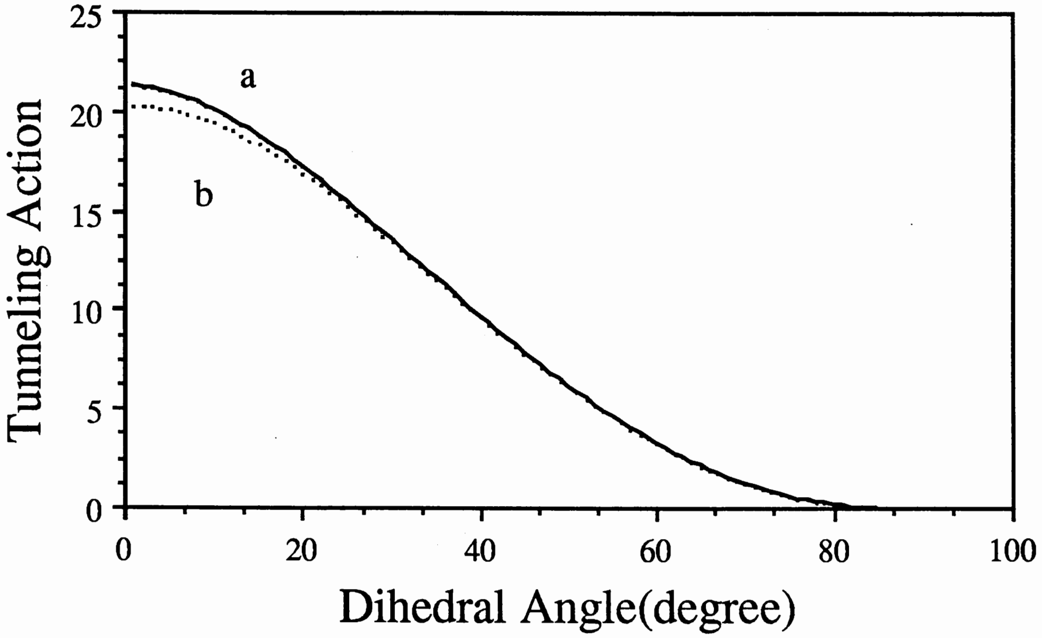

Figure 4. Tunneling Action Evaluated by Using "True" Torsional Potential and the Approximation as a Function of the Dihedral Angle. The Value of Effective Mass is Taken to be the *Cis*–HONO at Equilibrium Geometry. The Upper Curve is for the Approximate Analytic Solution and the Lower Curve is for "True" Numerical Solution.

A Plot of the tunneling integral Eq. (IV-4) using the actual torsional potential (lower curve) and the approximation Eq. (IV-16) (upper curve) as functions of the dihedral angle τ is shown in Fig. 4. The value of $G_{\tau\tau}$ is taken to be that for equilibrium *cis*-HONO. The two curves are in good agreement (there is less than 1% deviation from the "true" value) in the range $25^0 \leq \tau \leq 85.44^0$. When the value of the τ is less than 25^0, (corresponding to the reactant-like configurations), the deviations become large (and the tunneling action is underestimated), but this has little effect on the final result since the contributions due to such terms are too small to actually affect the averaged cumulative tunneling rate.

Figure 5 shows the natural logarithm of the survival probability evaluated using Eqs. (IV-4) and (IV-16) versus time for an ensemble of 800 trajectories. The initial excitation modes are for the OH stretch v_{OH}=0.5 and the torsional motion v_{τ}=3 and the total energy is 13 kcal/mol. The panel (a) of Fig. 5 is for trajectories initiated in the *cis* –well. The upper curve is a "real" result evaluated by Eq. (IV-4), and the lower curve is obtained by evaluating equation (IV-16). The slope ratio of the upper curve to lower one is 0.93. Panel (b) of fig. 5 is for trajectories initiated in the *trans* –well. The upper curve is an approximate result calculated by Eq. (IV-16) and the lower curve is obtained by evaluating Eq. (IV-4). The ratio of the decay rates evaluated by Eq. (IV-4) to the approximate one, Eq. (IV-16), is 1.3. This result indicates that the accuracy of Eq. (IV-16) will be much better when the system has large tunneling probability (see Tables V to IX). When the tunneling probability is small, Equation (IV-16) will result in large deviation, however the total tunneling effect is too small to be important.

The tunneling rate constants calculated by Eqs. (IV-4) and (IV-16) for both *cis→trans* and *trans→cis* with various initial excitations and total energies are listed in Tables V and IX. In general, the tunneling rate constants calculated by Eq. (IV-16) are in good to excellent agreement with those evaluated by Eq. (IV-4).

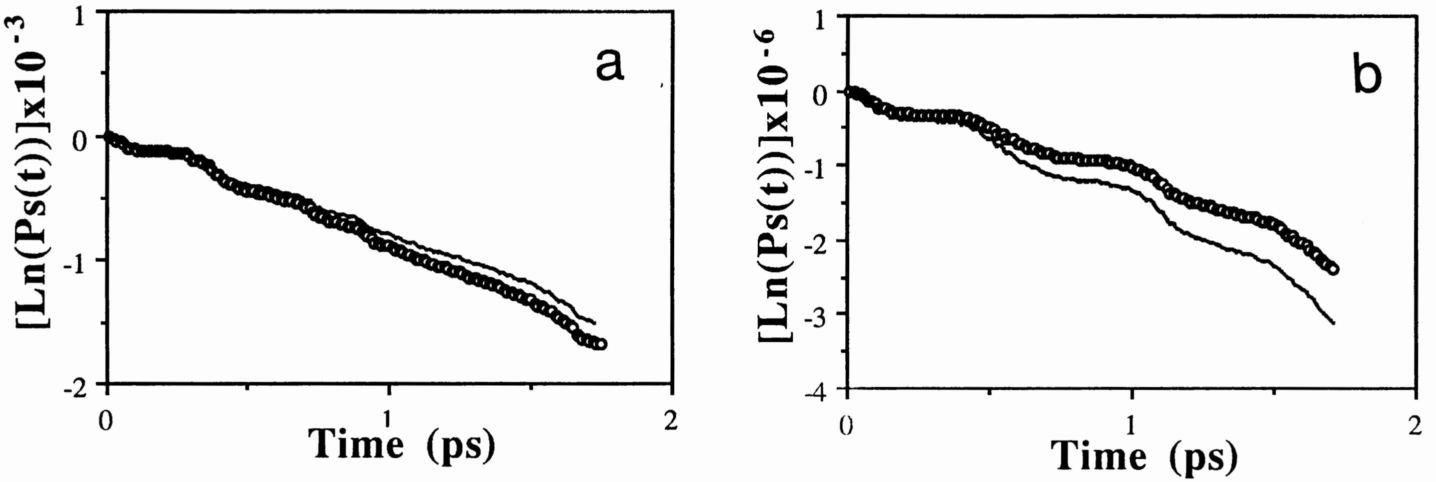

Figure 5. Plots of the Natural Logarithm of the Average Survival Probabilities as a Function of Time. The OH Stretch is Excited to $\nu_{OH}=0.5$ and the Torsional Mode is Excited to $\nu_{\tau}=3$ with Total Energy 13 kcal/mol. (a) Trajectories are Initiated in the *Cis*–well. The Upper Curve is a "True" Result and the Lower Curve is an Approximate Result. (b) Same as (a) Except that Trajectories are Initiated in the *Trans*–well and the Upper Curve is an Approximate Result and the Lower Curve is a "True" Result.

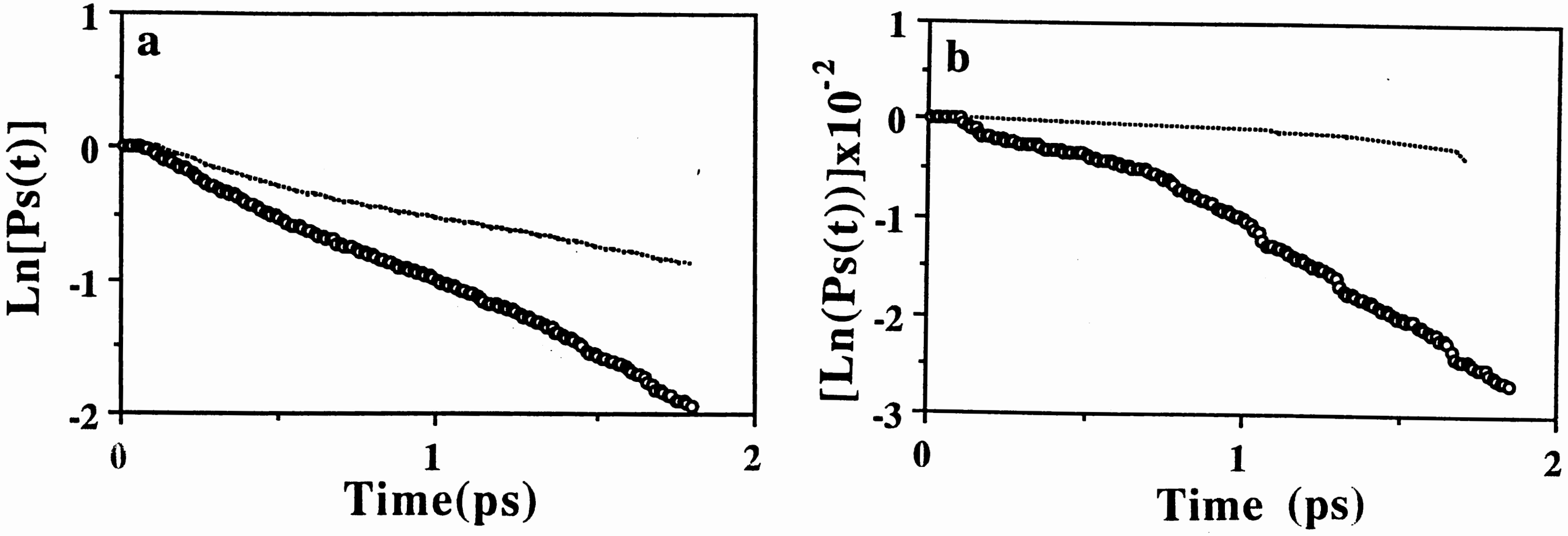

Figure 6. Plots of the Natural Logarithm of the Average Survival Probabilities as a Function of Time. The N-O Stretch is Excited to $\nu_{N\text{-}O}=1.7$ and the Torsional Mode is Excited to $\nu_{\tau}=3$ with Total Energy 13 kcal/mol. (a) Trajectories are Initiated in the *Cis*–well. The Upper Curve is the Purely Classical Decay Curve and the Lower Curve is for Classical-plus-tunneling Result. (b) Same as (a) Except for Trajectories Initiated in *Trans*-well.

The approximation saves CPU time by a factor of 180. Of course, as the tunneling probability becomes very small the error in Eq. (IV-16) becomes large; however, the largest ratio of the tunneling rate coefficient obtained by Eq. (IV-16) to one obtained by Eq. (IV-10) is less than 2. In the cases where the deviation is large the associated tunneling probability is vanishingly small. Finally, we note that the symmetric approximation to the asymmetric torsional potential more accurately fits the *trans* well than it does the *cis*.

Tunneling Effect Calculations with Full ZPE

The initial energy assignment is discussed in detail in the Chapter II. Briefly, each normal mode was assigned full zero point normal mode energy, then a normal mode (or some combination of normal modes) was selectively excited to the desired level (sometimes to non-quantal levels). Following the procedure of chapter II, the coordinates and momenta were then scaled to give the correct total energy. All trajectories were initiated in either the *cis* or *trans* minimum, i.e., all of the energy in the torsional mode was assigned initially in the form of kinetic energy.

Initial rates of *cis*→*trans* and *trans*→*cis* were computed for various initial energy distributions at fixed total energies in the range of 17 to 22 kcal/mol for ensembles of 800 to 1000 trajectories. Each trajectory was propagated until 50 turning points in the torsional coordinate were encountered.

TABLE V

COMPUTED RATE COEFFICIENTS WITH FULL ZERO-POINT-ENERGY FOR HONO *CIS–>TRANS* ISOMERIZATION

initial distribution							k (ps^{-1})		
$v_{O\text{-}H}$	$v_{N=O}$	v_{HON}	$v_{N\text{-}O}$	v_{ONO}	v_{τ}	Energy (kcal/mol)	k_{cla}	$k_{cla+tun}$	Eq. (IV-16)
0.5	0	0	0	0	0	17	0.0	$3.9x10^{-9}$	$4.7x10^{-9}$
0	1	0	0	0	0	17	0.0	$5.6x10^{-11}$	$6.2x10^{-11}$
0	0	1.5	0	0	0	17	$2.8x10^{-2}$	$3.5x10^{-2}$	$3.5x10^{-2}$
1	0	0	0	0	0	22	0.0	$1.3x10^{-7}$	$1.6x10^{-7}$

The classical and classical-plus-tunneling rate coefficients of *cis–>trans* isomerization are given in Tables V and VI. The results for mode selective excitations are given in Table V. Obviously, the decay rate is strongly dependent on the mode which is initially excited. For instance, when the O-H stretch is initially excited to v_{OH}=0.5, the tunneling rate is $3.9x10^{-9}$ ps^{-1} by rigorously evaluating Eq. (IV-4) and $4.7x10^{-9}$ ps^{-1} by Eq. (IV-16) for an ensemble of 900 trajectories. Excitation of the N=O stretch to $v_{N=O}$=1 yields the slowest tunneling rate, $5.6x10^{-11}$ ps^{-1} and $6.2x10^{-11}$ ps^{-1} evaluated by Eqs. (IV-4) and (IV-16), respectively. It is interesting to note that when the HON bending is excited the decay rate is significantly increased. The classical rate is $2.8x10^{-2}$ ps^{-1}, and the classical-plus-tunneling rate is $3.5x10^{-2}$ ps^{-1}, which is 1.25 times larger than the classical rate and 9 orders of magnitude larger than that of the N=O stretch excitation. When the total energy of the system is increased to 22 kcal/mol, the tunneling rate is $1.3x10^{-7}$ ps^{-1} for the O-H stretch excitation. Those results show that increasing the excitation energy will, of course, accelerate the reaction and enhance the tunneling rate. The "correct" excitation site seems to play an important role in determining the magnitude of the decay rate, once the total energy is the same.

In order to understand how the excitation energy affects the tunneling rate, we investigated the tunneling rate as a function of the excitation energy. Table VI shows those results.

TABLE VI

COMPUTED RATE COEFFICIENTS VERSUS TOTAL ENERGIES FOR HONO *CIS–>TRANS* ISOMERIZATION WITH FULL ZERO-POINT-ENERGY[a]

	k (ps^{-1})		
Energy (kcal/mol)	k_{cla}	$k_{cla+tun}$	Eq. (IV-16)
15	0.0	$1.2x10^{-7}$	$1.4x10^{-7}$
16	0.0	$1.1x10^{-4}$	$9.9x10^{-5}$
17	$2.3x10^{-3}$	$4.4x10^{-3}$	$4.7x10^{-3}$
18	$3.4x10^{-3}$	$4.9x10^{-3}$	$4.9x10^{-3}$
22	$6.5x10^{-2}$	$8.2x10^{-2}$	$8.2x10^{-2}$

a. The excitation energy is "equally" partitioned in all the six vibrational modes except the torsional mode.

Results of Table VI show that the decay rates are significantly increased by increasing the excitation energy of the system. For example, when the excitation energy is about 3 kcal/mol, the calculated tunneling rate is $1.2x10^{-7}$ ps^{-1}. However, when the excitation energy increases to 5 kcal/mol, the classical-plus-tunneling rate is 4.4×10^{-3} ps^{-1}, which is 4 orders of magnitude larger than the former case. The ratio of the the decay rate with and without tunneling correction is about a factor of 2. This result indicates that the tunneling is not a negligible factor. When the total energy of the system increases, the ratio of the classical to the classical-plus-tunneling rate will increase until it approaches unity (see Table VI). This is simply because the tunneling effect is "screened" by a large number of classical crossings.

In the above calculations, the full zero-point-energy of the molecule is included. Considering the fact that the zero-point-energy of the molecule is available to flow in the classical trajectories, a simple model calculation in which we arbitrarily removed 3/4 of ZPE from the system was carried out to reinvestigate the tunneling effects. In this way we can hopefully evade, to some extent, the effect of the ZPE flow on the tunneling rate. The advantage of this treatment is simple and direct. The disadvantage of this method is, of course, losing some of the reality of the molecule.

Tunneling Effect Calculations with 1/4 ZPE

In the following calculations, only a quarter of the ZPE (about 3 kcal/mol) is partitioned into the system and the total energy of the system is reduced to 13 to 15 kcal/mol as opposed 17 to 22 kcal/mol when the full ZPE is included. In order to increase the tunneling probability for most of the calculations in this part of the study, we excited the torsional mode to the second overtone state.

Initial rates of *cis*→*trans* and *trans*→*cis* were computed for various initial energy distributions at fixed total energies in the range of 13 to 15 kcal/mol for ensembles of 800 to 1000 trajectories. Again, each trajectory was propagated until 50 turning points in the torsional coordinate were encountered.

The effects of tunneling are illustrated by the results shown in Figure 6, which shows plots of the survival probability versus time in the *cis* (panel (a)) and *trans* (panel (b)) wells when the N-O stretching mode is excited to $v_{N\text{-}O}=1.7$ and the torsional mode to $v_{\tau}=3$. The total energy is 13kcal/mol. The upper curves in both plots are the purely classical results, and the lower curves are the classical-plus-tunneling results. The tunneling correction is about a factor of 2 for *cis–>trans* and about a factor of 3.3 for *trans–>cis*.

The classical and classical-plus-tunneling rates are given in Tables. VII, VIII, and IV. The molecule was assigned only one-fourth of the ZPE, and fraction quantum states were used to get desired total energy. Results for 15 kcal/mol total energy are given in Table VII.

TABLE VII

COMPUTED RATE COEFFICIENTS FOR HONO (*CIS–>TRANS*) ISOMERIZATION AT TOTAL ENERGY 15 KCAL/MOL AND 1/4 ZERO-POINT-ENERGY

initial distribution						k (ps^{-1})		
$v_{O\text{-}H}$	$v_{N=O}$	v_{HON}	$v_{N\text{-}O}$	v_{ONO}	v_{τ}	k_{cla}	$k_{cla+tun}$	Eq. (IV-16)
0.7	0	0	0	0	1	0.0	6.7×10^{-9}	9.5×10^{-9}
0	1.6	0	0	0	1	0.0	3.5×10^{-9}	4.8×10^{-9}
0	0	1.9	0	0	1	3.9×10^{-2}	5.2×10^{-2}	5.2×10^{-2}
0	0	0	2.7	0	1	7.7×10^{-2}	1.1×10^{-1}	1.1×10^{-2}
0	0	0	0	4.5	1	4.9×10^{-3}	7.1×10^{-3}	7.1×10^{-3}

Again, the decay rate varies with the initial excitation site; for example, the rates are 1.1×10^{-1} and 3.5×10^{-9} ps^{-1} for N-O and O=N stretch excitations, respectively. The N=O and O-H excitations yield the slowest decay rates while the N-O stretch excitation yields the largest. The ratio of the classical-plus-tunneling rate to the classical rate is about 1.4 on average. The results in Tables VIII and IX are for 13 kcal/mol total energy with the torsional mode being excited to the second overtone states.

TABLE VIII

COMPUTED RATE COEFFICIENTS FOR HONO (*CIS–>TRANS*) ISOMERIZATION AT TOTAL ENERGY 13 KCAL/MOL AND 1/4 ZERO-POINT-ENERGY

initial distribution					k (ps^{-1})		
$v_{H\text{-}O}$	$v_{N=O}$	v_{HON}	$v_{N\text{-}O}$	v_{ONO}	k_{cla}	$k_{cla+tun}$	Eq (IV-16)
0.5	0	0	0	0	0.0	8.4×10^{-4}	9.0×10^{-4}
0	0.7	0	0	0	2.3×10^{-2}	5.2×10^{-2}	5.2×10^{-2}
0	0	1.2	0	0	2.0×10^{-1}	2.8×10^{-1}	2.7×10^{-1}
0	0	0	1.7	0	0.49	1.1	1.1
0	0	0	0	3	2.0×10^{-2}	3.3×10^{-2}	3.4×10^{-2}

TABLE IX

COMPUTED RATE COEFFICIENTS FOR HONO (*TRANS→CIS*) ISOMERIZATION AT TOTAL ENERGY 13 KCAL/MOL AND 1/4 ZERO-POINT-ENERGY

initial distribution					Total energy	k (ps^{-1})		
$v_{H\text{-}O}$	$v_{N=O}$	v_{HON}	$v_{N\text{-}O}$	v_{ONO}	(kcal/mole)	k_{cla}	$k_{cla+tun}$	Eq. (IV-16)
0.5	0	0	0	0	13	0.0	1.7x10^{-6}	1.3x10^{-6}
0	0.7	0	0	0	13	0[a]	8.9x10^{-3}	8.5x10^{-3}
0	0	1.2	0	0	13	0[a]	2.7x10^{-3}	2.6x10^{-3}
0	0	0	1.7	0	13	4.6x10^{-3}	1.5x10^{-2}	1.5x10^{-2}
0	0	0	0	3	13	0	7.7x10^{-6}	7.0x10^{-6}
0	1	0	0	3	14	1.5x10^{-2}	3.5x10^{-2}	3.5x10^{-2}

a. We observed fewer than 4 trajectories that classically crossed over the barrier, out of an ensemble of 800 trajectories with 50 turning points.

The results in Table VIII are for the *cis→trans* isomerization and those in Table IX are for the *trans→cis*. There are several interesting things to be noted about the results. The rates for the *cis→trans* conversion are significantly larger (from a factor of 5 up to two orders of magnitude) than *trans→cis*. Excitation of the N-O single bond ($v_{N\text{-}O}$=1.7) gives the largest rate coefficients for both *cis→trans* ($1.1 ps^{-1}$) and *trans→cis* ($1.5x10^{-2} ps^{-1}$), respectively (see Tabs VIII and IX). The slowest rate coefficients are obtained, when the OH stretching normal mode corresponds to v_{OH}=0.5. for both *cis→trans* ($8.4x10^{-4} ps^{-1}$) and *trans→cis* ($1.7x10^{-6} ps^{-1}$).

These results also show that the tunneling effect plays an important role in the HONO isomerization. The largest ratio of the classical-plus-tunneling rate to the corresponding purely classical rate is 3.3. Furthermore, the rates depend on which modes are initially excited.

The tunneling rate depends on the vibrational frequency in the direction of the tunneling coordinate and the tunneling probability at that point. The individual tunneling probabilities depend upon local properties of the trajectory at the turning points, such as the effective energy in the tunneling coordinate, E_τ, and the "effective mass", $G_{\tau\tau}^{-1}$. In order to address questions such as "Why is the tunneling rate resulting from N-O stretch excitation significantly larger than the other normal mode excitations?" and "Which factors (such as energy , effective mass, or frequency of turning points along the tunneling direction) affect the tunneling probability most?" we have to examine these factors so that we gain an overall picture of the interplay between them.

We have attempted to do this by computing distributions of E_τ, the "turning period" (which we define as the time interval between the subsequent turning points), and $G_{\tau\tau}^{-1}$ for various initial excitations.

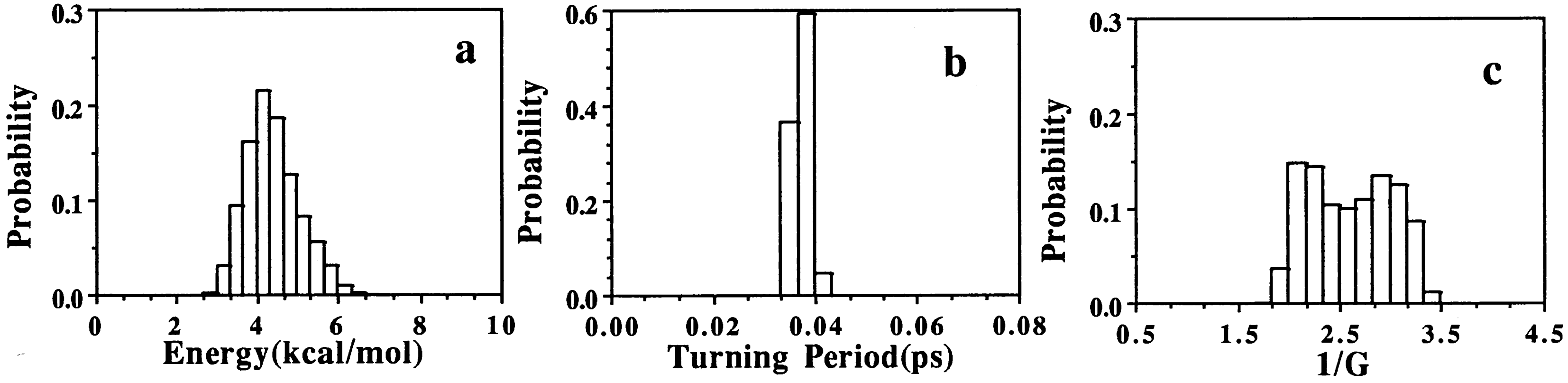

Figure 7. Plots of the Normalized Distributions for *Trans*–HONO Initially Excited to $v_{OH}=0.5$ and $v_{\tau}=3$ with Total Energy 13 kcal/mol. (a) Energy in the Torsional Mode at the Turning Points. (b) Same as (a) Except that the Distribution is for the Turning Period. (c) Same as (a) Except that the Distribution is for the Effective Mass.

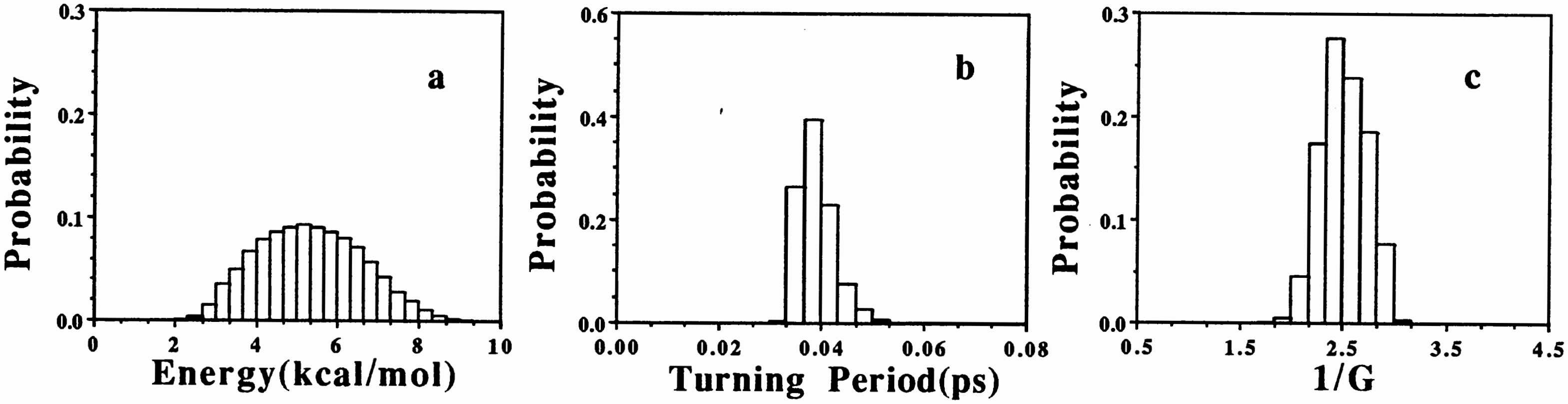

Figure 8. Same as Fig. 7 Except that the Initial Excitation is $v_{N\text{-}O}=1.7$

The results, shown in Figs. 7 and 8, are histogram plots of the values of these quantities at the torsional barrier turning points. The initial conditions of Fig. 7 correspond to the first row of Table IX (OH stretch excitation) while those for Fig. 8 are the same as the fourth row of Table IX (N-O stretch excitation). Both sets of results are for trajectories initiated in the *trans* well and for 13 kcal/mol total energy.

Although the total energies of the ensembles shown in Figs. 7 and 8 are the same, the tunneling rates differ by four orders of magnitude. Comparison of the individual panels of Fig. 7 with the corresponding ones in Fig. 8 aid in understanding the large disparity in the rates. Specifically, the distribution of the energy in the tunneling coordinate at the turning points (Fig. 7(a)) is relatively narrow compared with the analogous result in Fig. 8. The distribution in Fig. 8(a) is considerably broader than the one in Fig. 7(a) and includes substantially higher energies (recall that the classical barrier to isomerization is 9.2 kcal/mol). The most probable value of the energy in Fig. 7(a) is 4.3 kcal/mol compared with a value of 5.2 kcal/mol in Fig. 8(a). The largest energy bin populated in Fig. 7(a) is centered at 6.3 kcal/mol; that of Fig. 8(a) is centered at 8.5 kcal/mol. This suggests that the rate of energy transfer from bath modes to the tunneling mode for the ensemble of trajectories represented by Fig. 8 is significantly greater than that for Fig. 7(a). From Eq. (IV-4), we know that the greater E_τ is at the turning point, the greater the tunneling probability will be for that particular encounter with the barrier.

The distribution of times between individual turning points are shown in Figs. 7(b) and 8(b). Once again, the distribution in Fig. 7(b) is narrower than that in Fig. 8(b). The most probable values are, however, the same (0.038 ps). On average, the turning period is shorter in Fig. 7(b) than in Fig. 8(b). The narrow distribution of the turning period in Fig. 7(b) suggests that the motion in the dihedral well is regular and that there is little energy exchange between the torsional mode and the remainder of the molecule. By contrast, when the N-O stretch is initially excited, the resulting turning period distribution is broadened (Fig. 8(b)). There is a clear relation between panels (a) and (b) in Figs. 7 and

8. The torsional coordinate is anharmonic. Therefore, the frequency of vibration of the dihedral angle (the tunneling coordinate) is a function of the energy in the torsional mode. The distribution of energies in Fig. 7(a) correlates directly with the turning period distribution of Fig. 7(b). Similar remarks apply to Fig. 8. Since the tunneling rate is proportional to the turning frequency and the tunneling probability, the shorter the turning period, the larger the tunneling rate. However, the calculated tunneling rates are $1.7\text{x}10^{-6}$ ps^{-1} and $1.5\text{x}10^{-2}$ ps^{-1} (which is four orders of magnitude difference) corresponding to Figs. 7 and 8, respectively. This suggests that the tunneling probability plays a more important role in determining the tunneling rate than does the turning period.

The distribution of the "effective mass", $1/G_{\tau\tau}$, is given in panel (c) of Figs. 7 and 8. The distributions of $1/G_{\tau\tau}$ are somehow similar to the distribution of the turning period. The range of the $1/G_{\tau\tau}$ is 1.9 to 3.4 $(\text{au})^2\cdot\text{amu}$ and 1.9 to 3.1 $(\text{au})^2\cdot\text{amu}$ in Figs.7(c) and 8(c), respectively. The tunneling decay rate is approximately exponentially proportional to E_τ and inversely proportional to $G_{\tau\tau}$. The quantities of E_τ and $G_{\tau\tau}$ vary with time, as do individual tunneling probabilities. Thus, there may be an identifiable correlation between E_τ and/or $1/G_{\tau\tau}$ and individual tunneling probabilities, $P_k(i)$ (for the ith trajectory and kth turning point for an ensemble of trajectories). We accumulated results for 40000-50000 turning points per ensemble of trajectories. It is difficult to plot such a large number of points on a single graph. However, the range of $P_k(i)$ spans roughly 14 orders of magnitude [from $O(e^{-30})$ to 1]. Thus, we did not attempt to manipulate the full set of data since the contributions of many of the $P_k(t)$ to the tunneling rate are negligibly small. Instead, we chose the 1400 turning points having the largest tunneling probability (excluding the classical reaction for which the probability is unity) from an ensemble of trajectories and plotted them. The results are shown in Figs. 9 and 10. The initial conditions for the Figs. 9 and 10 are the same as for Figs. 7 and 8, respectively. Panel (a) of Fig. 9 is the natural logarithm of the tunneling probability, ln(Ptun), versus effective mass of the tunneling coordinate $1/G_{\tau\tau}$ for an ensemble of trajectories. The value of $1/G_{\tau\tau}$

ranges from 1.9 to 3.3 a.u.^{2}a.m.u. Similar results are obtained for an initial N-O stretch excitation (see Fig. 10(a)). The range of $1/G_{\tau\tau}$ in the latter case is 1.9 to 3.0 a.u.^{2} a.m.u. Although the arranges of $\ln(P_{tun})$ are quite different, $\ln(P_{tun})=-0.8 \sim -6.5$ (in Fig. 10) and $\ln(P_{tun})=-9.9 \sim -15$ (in Fig. 9).

When the turning points are close to the top of the potential barrier, the magnitude of the tunneling probability is controlled by the amount of energy populated into the tunneling coordinate at that instant time. In Figs. 9(b) and 10(b), we represented the natural logarithm of the tunneling probability as a function of E_τ for the different initial excitations. When the OH stretch bond was initially excited, Fig. 9(b) was obtained. Obviously, the value of the tunneling probability is not only dependent on the E_τ, but also on the reciprocal of $G_{\tau\tau}$. The competition between E_τ and $G_{\tau\tau}$ makes the distribution of the tunneling probability "chaos". When the the N-O stretch initially populated $\nu_{NO}=1.7$, ln(Ptun) was plotted as a function of E_τ (see Fig. 10(b)). The value of ln(Ptun) approximately monotonically increases with increasing E_τ. That is, the value of E_τ directly governs the magnitude of the tunneling probability, and effective mass $1/G_{\tau\tau}$ plays much less role in this case. The same qualitative characteristics were revealed when the isomerization undergoes the *cis→trans* process. Figures 11-14 are the same as Figs.7-10 except that the former are for *cis→trans*. The major differences between Figs. 11-14 and 7-10 are that the distribution of the E_τ, $1/G_{\tau\tau}$, and the turning period are more "spread" in Figs. 11-12 than in Figs. 7-8. That is simply because the rate of the IVR in *cis* -HONO is much faster than in *trans*-HONO as Guan *et al.*[52,53] reported.

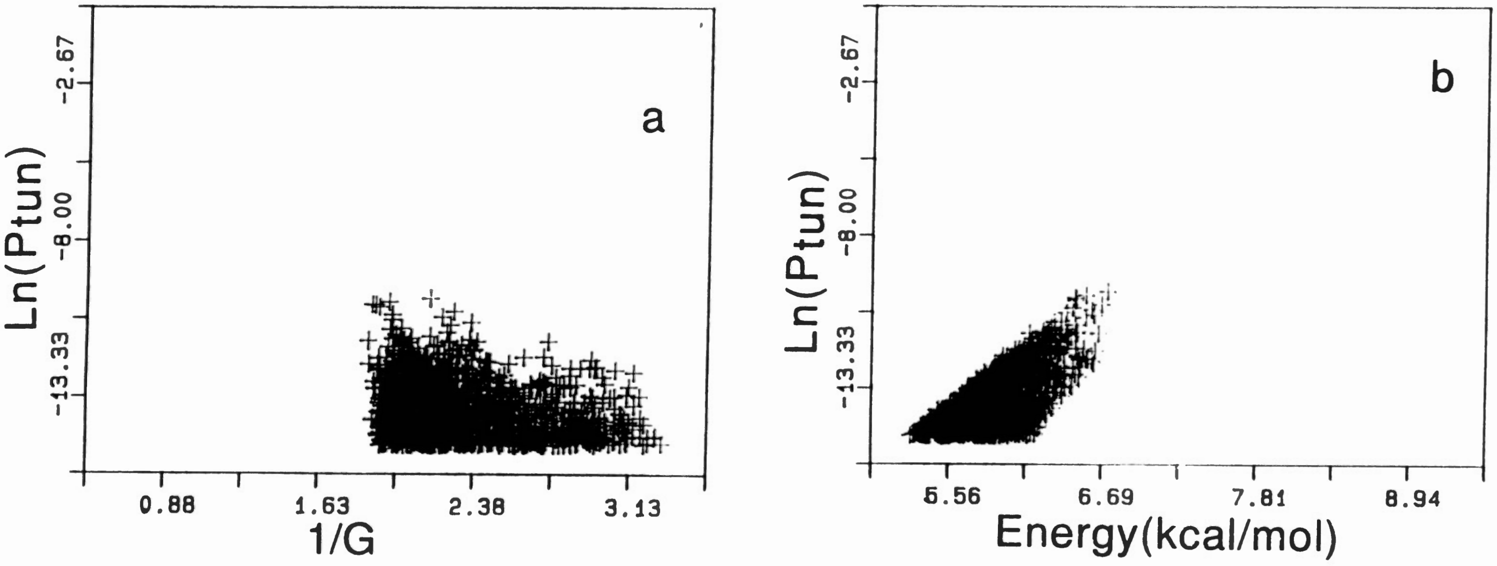

Figure 9. Scatter Plots for *Trans*–HONO Initially Excited to $\nu_{OH}=0.5$ and $\nu_{\tau}=3$ with Total Energy 13 kcal/mol. (a) Tunneling Probabilities versus Effective Mass. (b) Same as (a) Except that the Abscissa is the Energy in the Torsional Mode at the Turning Points.

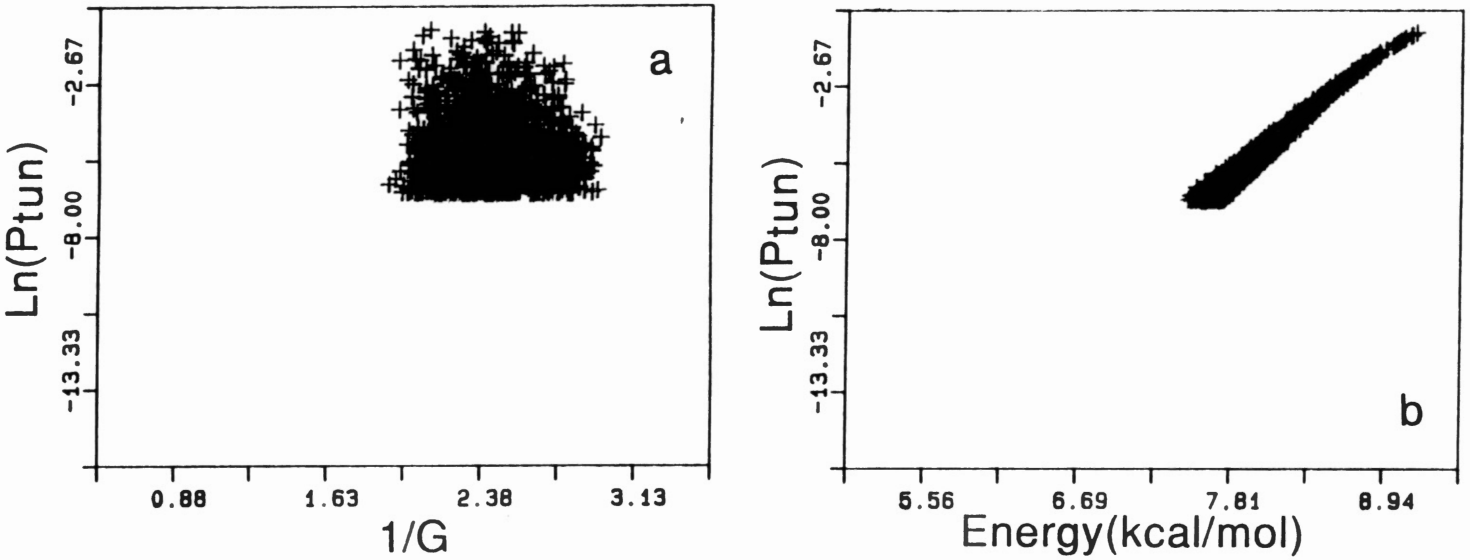

Figure 10. Same as Fig. 9 Except that Ensemble Trajectories are Identical to Fig. 8.

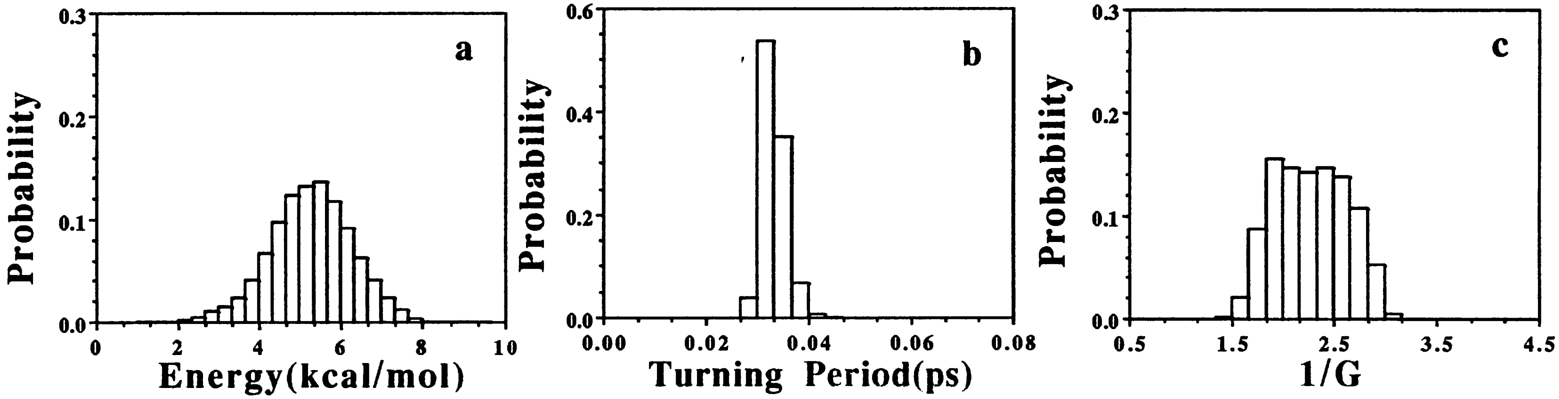

Figure 11. Same as Fig. 7 Except for *Cis->Trans* Process.

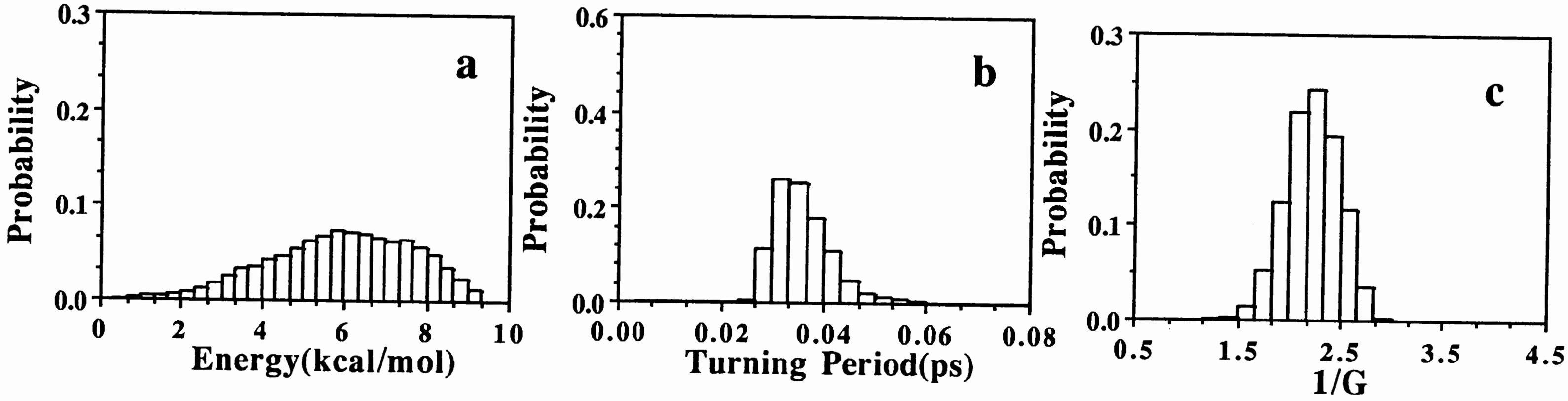

Figure 12. Same as Fig. 8 Except for *Cis–>Trans* Process.

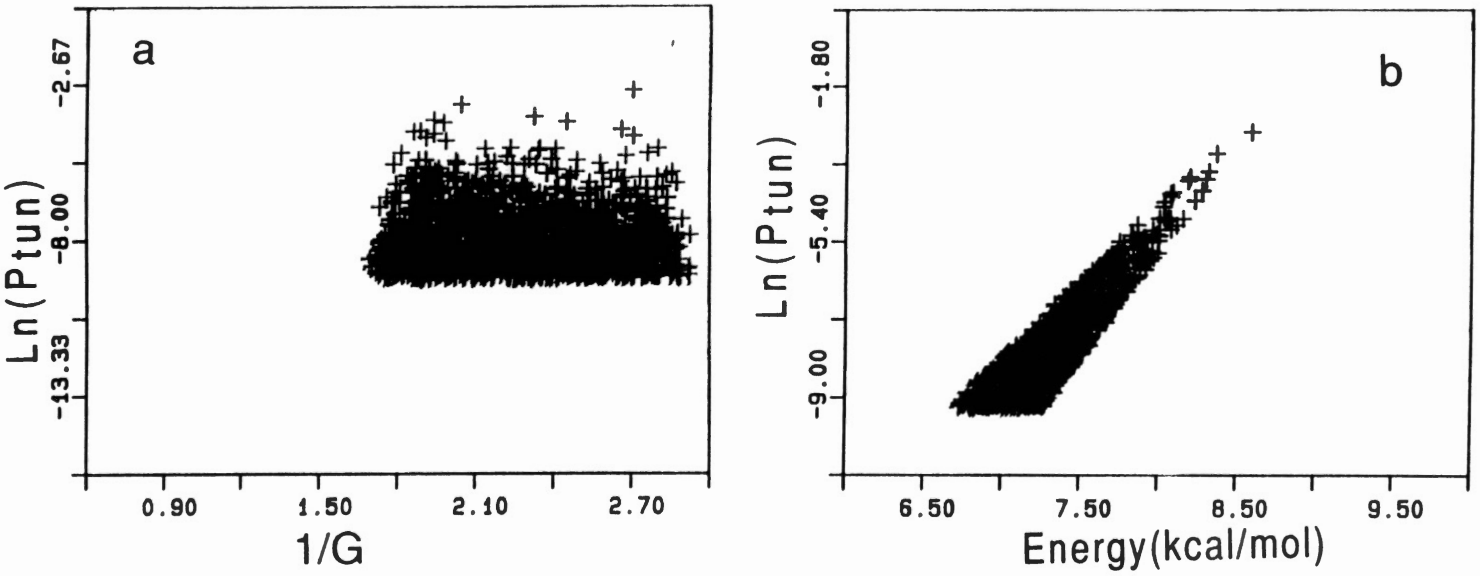

Figure 13. Same as Fig. 9 Except for *Cis–>Trans* Process.

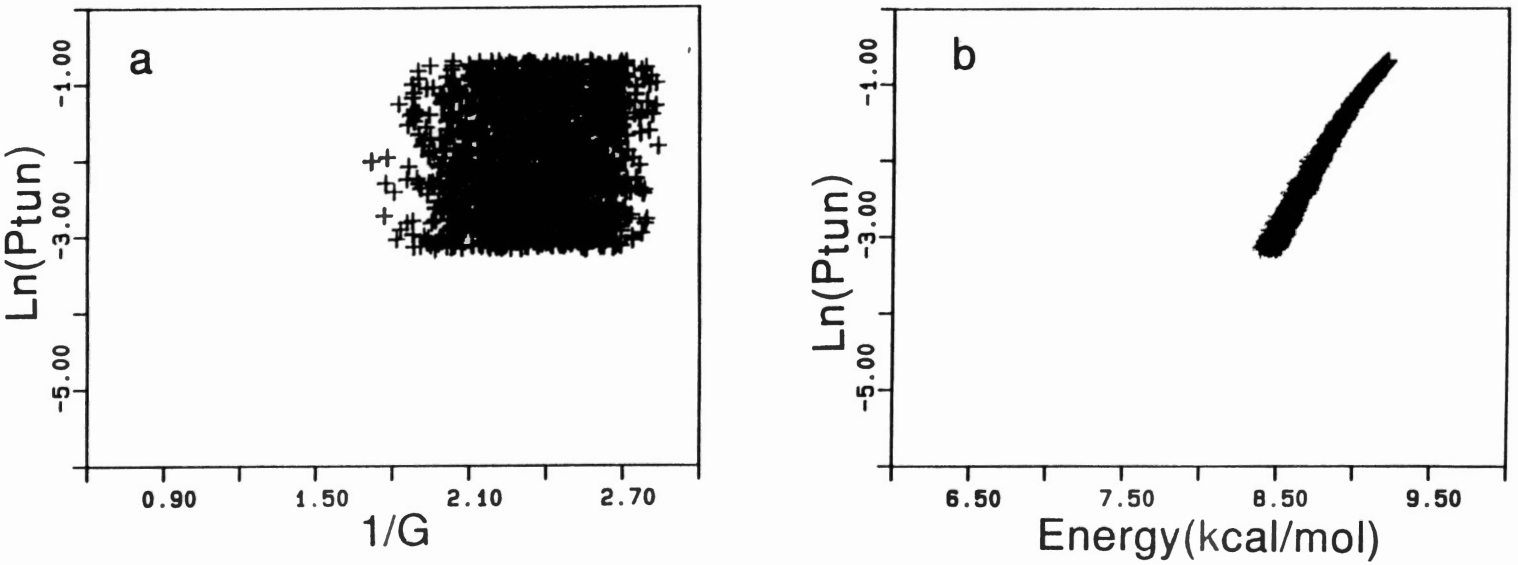

Figure 14. Same as Fig. 10 Except for *Cis–>Trans* Process.

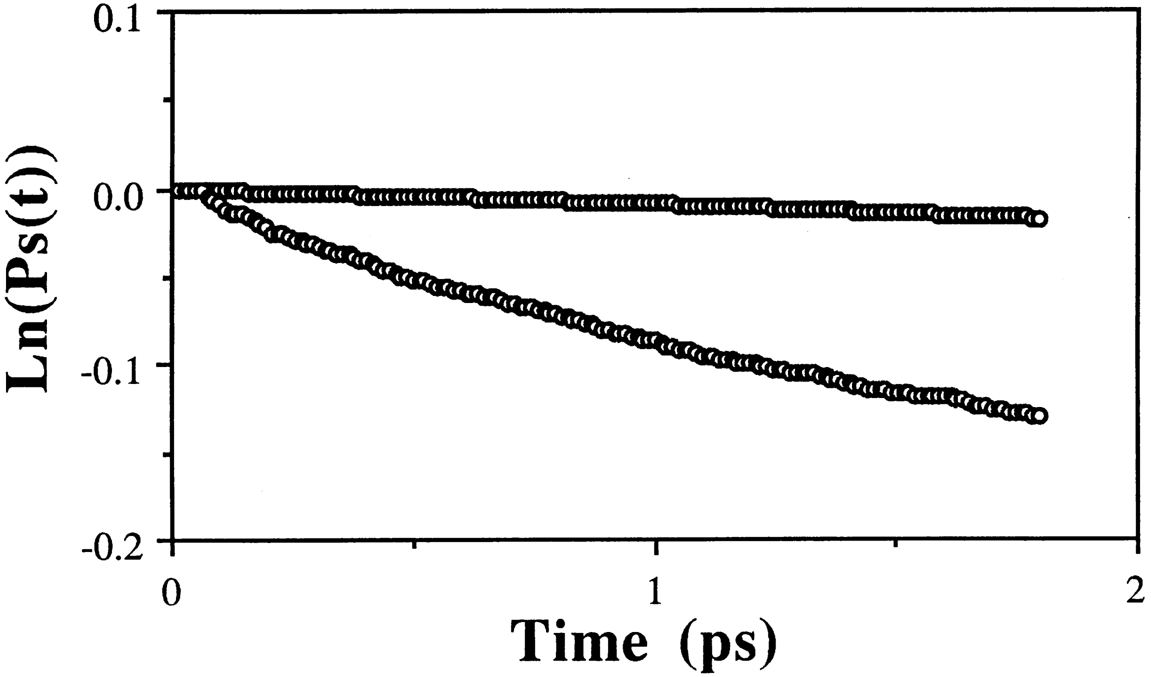

Figure 15. The Natural Logarithm of the Average Survival Probabilities as a Function of Time for the Initial Excitation $\nu_{N\text{-}O}=1.7$, and $\nu_{\tau}=3$ with Total Energy 13 kcal/mol. The Upper Curve for *Trans→Cis* and the Lower Curve for *Cis→Trans*.

Although the isomerization rates for the *cis→trans* are generally larger than the *trans→cis*, the tunneling effects seem more significant for the *trans–>cis* than for the reverse process. In order to determine the tunneling contribution, we deleted all the trajectories that classically isomerized and analyzed the rest of the trajectories that contributeed to the isomerization by tunneling only. In Fig. 15 we plotted the average pure tunneling survival probability as a function of time for both *cis–>trans* (lower curve) and *trans→cis* (upper curve) with the same initial energy distribution (excitation of the N-O single bond stretch). The ratio of the slope of the lower curve to the upper curve is 3.5, which means that the tunneling effect for the *cis* is more significant than that for the *trans*. However, the ratio of the classical-plus-tunneling and classical rate coefficients is a factor of 2 for the *cis→trans* and a factor of 3.3 for the *trans→cis*.

Another important point to note regarding to the results of Tables VII and IX is mode specificity. The significant mode specific behaviors were observed in our early calculations by Guan *et al.*[52,53] In the present study, in which the total energy of the system is much lower than before, we expected to see stronger mode specificity. For the same total energy but different initial energy distribution the rates coefficients can be up to four orders of magnitude difference. For instance, the OH bond stretch excitation (ν_{O-H}=0.5) yields the slowest rate coefficients, $8.4\text{x}10^{-4}$ ps^{-1} and $1.7\text{x}10^{-6}$ ps^{-1} for the *cis→trans* and *trans→cis* isomerization processes, respectively. The most efficient excitation is the N-O single bond excitations (ν_{N-O}=1.7) which yield the largest rate coefficients 1.1 ps^{-1} and $1.5\text{x}10^{-2}$ ps^{-1} for the *cis→trans*, and *trans→cis*, respectively. In both *cis→trans* and *trans→cis* cases, the differences in rates for various initial energy partitions are significant (see Tables. V to IX).

The zero-point-energy effects seem to have little effect on the tunneling in our calculations, since the initial conditions for Tables V and VII are quite similar except that the zero-point-energy partitions are different (with the full ZPE included in the Table V, and only a quarter of the ZPE in Table VII) and the torsional mode is excited to ν_{τ}=1 in

Table. VII. Comparison of the results summarized in Table V with the corresponding ones in Table VII may give some qualitative pictures of the zero-point-energy effect upon tunneling. The largest ratio of the purely classical to the classical-plus-tunneling are 1.3 (see Table V for full ZPE results) and 1.4 (see the fourth column of Table VII for results of one-quarter ZPE). Furthermore, the largest ratios of the rate coefficient computed with and without tunneling correction are 1.9 with full ZPE (see Table VI) and 2.4 with one-quarter ZPE (see Table VIII), respectively. Those results indicate that the zero-point-energy has some effect on intramolecular energy transfer but it is not a serious effect in our system.

Isotopic Substitutions of HONO

The effects of isotopic substitution on the rates of isomerization in HONO were investigated. The computed values of the frequencies of DONO and $HO^{18}NO^{18}$ were given the Table X. The differences in the zero-point-energy for the HONO and DONO were 926 cm^{-1}(*cis*) and 976 cm^{-1} (*trans*). To account for the differences in the zero-point energies between the HONO and DONO, we excited the DO stretch mode to $\nu_{D\text{-}O}=0.686$ and the torsional mode to $\nu_\tau=3.75$ for the *cis* -DONO and $\nu_{D\text{-}O}=0.655$, $\nu_\tau=3.975$ for *trans*-DONO (see Table X). Thus, we obtained nearly the same relative distribution of energy as in HONO. The calculated rate coefficient for *cis*-DONO is 2.0×10^{-5} ps^{-1}, which is 42 times smaller than the analogous for HONO. The reverse process shows even greater sensitivity to D substitution. The tunneling rate computed for the *trans*→*cis* isomerization in DONO is 2×10^{-8} ps^{-1}. This is 85 times slower than the tunneling rate of HONO with the corrsponding set of initial conditions.

TABLE X

COMPUTED NORMAL MODE FREQUENCIES (cm^{-1}) FOR THE DONO AND HO^{18}NO^{18}

	ν_1(D-O)	ν_2(N=O)	ν_3(DON)	ν_4(O-N)	ν_5(ONO)	$\nu_6(\tau)$
trans						
experiment[a]	2648	1692	1014	737	586	416
calculated	2614	1664	1025	767	538	407
cis						
experiment[a]	2525	1625	1008	814	504	601
calculated	2500	1626	1008	900	509	512

	ν_1(H-O^{18})	ν_2(N=O^{18})	ν_3(DO^{18}N)	ν_4(O^{18}-N)	ν_5(O^{18}NO^{18})	$\nu_6(\tau)$
trans						
experiment[a]	3571	1666	1251	779	564	537
calculated	3577	1659	1252	834	515	535
cis						
experiment[a]	**	1606	**	840	576	631
calculated	3414	1603	1287	891	514	624

a. Reference 79.

** No data available.

TABLE XI

COMPUTED ISOMERIZATION RATE COEFFICIENTS FOR DONO WITH 1/4 ZERO-POINT-ENERGY

	Initial distribution						Total energy	k (ps^{-1})
	$\nu_{D\text{-}O}$	$\nu_{D=O}$	ν_{DON}	$\nu_{N\text{-}O}$	ν_{ONO}	ν_{τ}	(kcal/mol)	(tunneling)
cis-trans	0.686	0	0	0	0	3.75	13	$2.0\text{x}10^{-5}$
trans-cis	0.655	0	0	0	0	3.975	13	$2\text{x}10^{-8}$

TABLE XII

COMPUTED ISOMERIZATION RATE COEFFICIENTS FOR $HO^{18}NO^{18}$ WITH 1/4 ZERO-POINT-ENERGY

Initial distribution							k (ps^{-1})
	$\nu_{H\text{-}O^{18}}$	$\nu_{N=O^{18}}$	$\nu_{HO^{18}N}$	$\nu_{N\text{-}O^{18}}$	$\nu_{O^{18}NO^{18}}$	ν_{τ}	tunneling
cis–>trans	0.5	0	0	0	0	3	$5.6\text{x}10^{-4}$
trans–>cis	0.5	0	0	0	0	3	$1.2\text{x}10^{-6}$

Table XII reported the rate coefficients of the oxygen eighteen substitution of HONO, since the frequencies of the $O^{18}H$ stretch mode and the torsional mode are almost the same as in the HONO. Thus, we partitioned the $HO^{18}NO^{18}$ in the same manner as in the HONO. For the $\nu_{O\text{-}H}$=0.5 and ν_{τ}=3 initial energy partition, the tunneling rate calculated is $5.6\text{x}10^{-5}$ ps^{-1}, which is 15 times slower than the tunneling rate of *cis* HONO. For the reverse process the rate is almost the same as the rate of HONO. We note that in our calculations, the potential energy surface is very simple, and we used the VAZC approximation, ignoring the reaction path curvature effects which are important for some systems.[10-14]

The present results are in qualitative accord with the data reported by Pimentel *et al.*[48,49] In their first experiment they could not observe any interconversion of DONO. Furthermore, even oxygen eighteen substitution significantly slows the isomerization, though this substitution can make very small changes in the reduced moment of inertia for the internal rotation associated with the torsional mode. Pimentel and co-workers pointed out that this extremely mass-sensitive isomerization rate implies tunneling effects.[48] In later work,[49] they reported that the value of the rate coefficient for *cis→trans* isomerization of HONO is about a factor of 10 times faster than the *trans–>cis* isomerization.

Summary

Tunneling effects in HONO isomerization have been studied using the Waite-Miller method to calculate semiclassical tunneling corrections. An approximate, analytic solution to the WKBJ tunneling integral was developed to replace the actual action integral. The approximation yields good results and a considerable reduction in expense, compared to results obtained by numerically solving the tunneling integral using the actual action integral. The rate coefficients for *cis→trans* isomerization are generally larger than those for *trans→cis*. Combination excitation of torsional and N-O stretch modes yields the largest rate coefficient for both *cis→trans* and *trans→cis* processes. Tunneling effects can not be neglected in the HONO interconversion process. The calculated classical-plus-tunneling rates are larger by a factor of 2 to 3 than those purely classical rates. Significant mode-specific behavior was observed in our calculations. The range of calculated rate coefficients (for the same total energy but different initial energy distributions) was found differ by 4 orders of magnitude.

The zero-point energy effects seem to have little effect on the tunneling for HONO. The largest ratios of the rate coefficient with and without tunneling correction are 1.9 with all the zero-point-energy and 2.4 with a quarter of zero-point energy, respectively. Those results indicate that the zero-point energy has some effect on intramolecular energy transfer.

The rate of the energy flow into the tunneling coordinate controls the tunneling rate, while the tunneling frequency and the effective mass play minor roles in determining the magnitude of the tunneling rate.

Isotopic substitutions were investigated. The initial rate of isomerization of *trans*-HONO is approximately 85 times faster than that of *trans*-DONO. The initial rate of isomerization of *cis*-HONO is about 42 times faster than that of *cis*-DONO. Oxygen-eighteen substitution in HONO is also studied. The tunneling rate for *cis*→*trans* isomerization of $H^{18}ON^{18}O$ is about slower times than the rate of $H^{16}ON^{16}O$ for the same initial energy distribution. These results are qualitatively in good agreement with experimental data[48-50] and earlier theoretical calculations.[52-54]

CHAPTER V

TUNNELING EFFECTS IN HYDROXYSILYENE *CIS–TRANS* INTERCONVERSIONS

We have incorporated the semiclassical tunneling corrections into the general classical trajectory code[66] and investigated the tunneling effect on the HSiOH isomerization process. The difficult part of this method is defining the tunneling direction and the tunneling coordinate.[30,32] It is difficult to find the tunneling direction in the sense of the "shortest distance" between the two configurations[32] (*cis* and *trans*) on the potential energy surface when the system involves more than two degrees of freedom. An alternative way to deal with such a system is to assume separability of the tunneling modes with rest of the vibrational modes during the tunneling process.

The available *ab initio* calculations[36,38-39] have indicated that the tunneling processes possibly involved the HOSi in-plane bend as well as the internal rotation coordinates. The Hamiltonian of the system in the representation of the internal coordinates is defined by Eq. (II-19) except the potential part for the HSiOH molecule, which is defined by Eqs. (III-5) to (III-12). We assumed that the tunneling processes are independent for the two individual tunneling coordinates. Furthermore, the vibrational zero curvature approximation was assumed[9] to be applicable for the tunneling process via the individual tunneling coordinates. That is, whenever a trajectory experienced extremum (a maximum or minimum) in the motion along the tunneling coordinates (the dihedral or HOSi in-plane bends), we stopped the trajectory and calculated the tunneling probability at that instant in time using Eqs. (IV-3) and (IV-4) (except, of course, the potential for HSiOH). The calculation procedure has been discussed in Chapter IV in detail. The only difference is that the tunneling coordinates involves both the HOSi bend and torsional motions for the present calculations.

Ensembles of 250-1000 trajectories were calculated for each set of initial conditions. The trajectories were propagated in a lab-fixed Cartesian coordinate system until a total of 100 turning points were encountered.

Classical Results

Classical isomerization of HSiOH was not observed through the HOSi in-plane bending mode, although the potential barrier for that channel is 0.25 kcal/mol lower than that of the torsional barrier. This is not surprising, since zero-point energy is initially partitioned into the torsional mode, nonzero angular momentum L(t) is induced along the Si-O bond and the hydrogen atom of the OH bond is subjected to a centrifugal force proportional to $L^2(t)/(r\sin(\theta'_{HOSi}))^3$, which is directed radially outward. When the HOSi bending angle approaches to 0^o or 180^o, the centrifugal force becomes infinitely large. Thus, the isomerization cannot occur via the HOSi in–plane bending coordinate. Spears and Hutchinson reported the same result for *trans*-diimide.[79]

Microcanonical rate coefficients for unimolecular isomerization of HSiOH have been computed at 32 kcal/mol total energy. A total of 250 trajectories were computed for each set of initial conditions. The calculated first-order rate constants were summarized in Table XIII.

TABLE XIII

COMPUTED ISOMERIZATION RATE COEFFICIENTS OF HSiOH WITH 32 KCAL/MOL TOTAL ENERGY

Initial distribution						k (ps^{-1})	
$v_{O\text{-}H}$	$v_{Si\text{-}H}$	v_{HSiO}	$v_{Si\text{-}O}$	v_{HOSi}	v_{τ}	*cis→trans*	*trans→cis*
0.47	0.92	1.80	2.0	0	0	2.6×10^{-1}	9.9×10^{-2}
2	0	0	0	0	0	3.2×10^{-2}	1.5×10^{-2}
0	4	0	0	0	0	1.4×10^{-1}	1.6×10^{-1}
0	0	7	0	0	0	1.0×10^{-1}	1.9×10^{-2}
0	0	0	8	0	0	3.0×10^{-1}	1.6×10^{-1}

The results shown in the first row of Table XIII are for calculations in which the excitation energy was "uniformly" distributed among all the coordinates except the HOSi bending and torsion coordinates, which are assumed to be the reaction coordinates. The calculated rate constants are 2.6×10^{-1} and 9.9×10^{-2} ps^{-1} for the *cis→trans* and *trans→cis*, respectively. The ratio of the rates for the *cis→trans* to the *trans→cis* is about 2.6. When the excitation energy was partitioned into the individual normal coordinate, the ratio of the rate of isomerization for *cis–>trans* to *trans–>cis* range from 1 to 5 depending on the mode that is excited. For instance, when the OH bond stretch was excited to $v_{OH}=2$, the calculated rate constants are 3.2×10^{-2} (*cis–>trans*) and 1.5×10^{-2} ps^{-1} (*trans–>cis*) while the rate constants corresponding to the Si-O bond stretch excitation ($v_{SiO}= 8$) are 3.0×10^{-1} ps^{-1} and 1.6×10^{-1} ps^{-1}. The rate constants for the Si-O stretch excitation is about an order of magnitude larger than for O-H stretch excitation at the same total energy Excitation of the O-H stretch yields the slowest rate coefficients for both *cis–>trans* and *trans–>cis*. When the Si-O stretch is initially excited, the largest isomerization rate coefficients are obtained for both *cis–>trans* and the *trans–>cis*. Since the total energy of the system is the same, the only difference is the excitation sites, these results must be due to the couplings between the vibrational modes. First, the O-H stretch mode is a good "local mode". The initial excitation places more than 99% of the excitation energy in the O-H in-plane stretch and the result is slow isomerization. However, the Si-O stretch normal mode is a "delocalized mode", thus, when the Si-O stretch is excited only about 75% of the excitation energy is in the Si-O stretch and the remainder is in the other in-plane modes. Further more that the kinetic couplings of the in-plane bending modes with the out-of-plane torsion mode are much stronger than the couplings of the stretch modes with the torsion mode.[80] Thus, the rate of energy transfer from bath modes to the torsional mode might be faster when the Si-O stretch is excited than when the OH stretch is excited. Second, the Si-O stretch is coupled strongly with the HOSi and HSiO bends and the relaxation of overtones of the Si-O stretch is significantly faster than the relaxation of the overtones of the OH stretch. Those results indicate that the excitation site and the extent of the interactions of the vibrational modes govern isomerization rate.

It is interesting to note that when the Si-H stretch is initially excited, the calculated rate coefficient ($1.6\text{x}10^{-1}$ ps^{-1}) for trajectories initiated in the *trans*-well is significantly larger (about a factor of 8) than the rate constant corresponding to the HSiO bending excitation ($1.9\text{x}10^{-2}$ ps^{-1}) for the same process. This indicates that the energy transfer path of the initially excited Si-H stretch does not simply follow the "stretch-bend-dihedral" model as we observed in the HONO isomerization[52-54].

Classical-Plus-Tunneling Results

The main purpose of the present study is to explore the importance of tunneling effects on the HSiOH isomerization processes. Since the two isomerization channels were open, the tunneling coordinates are taken to be the HOSi bending and dihedral angles. In the calculations, we monitored both tunneling coordinates. Whenever tunneling coordinates, for example, the θ_{HOSi} experienced a maximum, we stopped the trajectory and calculated the tunneling probability at that point then continued to propagate the trajectory until the desired number 100 of the tunneling events were collected. Since the dihedral angle is two-fold degenerate, thus the turning points were determined whenever the dihedral angle τ experienced either a minimum or a maximum.

Both classical and classical-plus-tunneling rate constants were computed for various initial conditions. These results are in Tables XIV–XVII. The overall rate coefficients k were obtained by least squares fitting the slope of the tunneling decay curves described by Eq. (II-55). The values of the "branching ratio" were calculated by using the overall rate coefficients and Eqs. (II-56) and (II-57). The average survival tunneling probabilities leading to isomerization via HOSi in-plane bend, $<P_{HOSi}>$, and internal rotation, $<P_{\tau}>$, were evaluated by using Eq. (II-16). A total of 400-1000 trajectories were calculated for each set of initial conditions.

The rate constants for *cis–>trans* and *trans–>cis* isomerization are listed in Tables XIV and XV, respectively. The total energy is 20 kcal/mol. Since the tunneling rate is normally slow process, and a long time is needed to observe significant tunneling results. In order to reduce the CPU time, we put a small amount of the energy into the tunneling coordinates to make the process faster. We partitioned 0.6 and 0.7 kcal/mol into the HOSi and torsional modes, respectively, and excited one of the remaining normal modes to some quantum number (a fraction or integral number) such that the total energy (excitation plus

ZPE) is close to desired the total energy. Then the coordinates and momenta were scaled to the desired total energy.

TABLE XIV

COMPUTED ISOMERIZATION RATE COEFFICIENTS OF
HSiOH (*CIS–>TRANS*) WITH 20 KCAL/MOL
TOTAL ENERGY

initial distribution						k(ps^{-1})		
$v_{O\text{-}H}$	$v_{Si\text{-}H}$	v_{HSiO}	$v_{Si\text{-}O}$	v_{HOSi}	v_τ	k_C (ps^{-1})	k_{C+T} (ps^{-1})	k_{C+T}/k_C
0.12	0.24	0.48	0.52	0.62	0.73	$1.4\text{x}10^{-2}$	$4.1\text{x}10^{-2}$	2.9
0.5	0	0	0	0.62	0.73	a	$1.4\text{x}10^{-2}$	
0	1	0	0	0.62	0.73	a	$1.6\text{x}10^{-2}$	
0	0	2	0	0.62	0.73	$3.0\text{x}10^{-2}$	$4.8\text{x}10^{-2}$	1.5
0	0	0	3	0.62	0.73	$3.0\text{x}10^{-2}$	$1.4\text{x}10^{-1}$	4.7

a. The rate is too slow to be evaluated on the timescale of the calculations.

In the first row of the Table XIV, we show the rate constants for the purely classical and classical-plus-tunneling calculations where the excitation energy is "equally" partitioned into the six vibrational modes. The calculated rate constants are $1.4\text{x}10^{-2}$ and $4.1\text{x}10^{-2}$ ps^{-1} for the purely classical and classical-plus-tunneling rates, respectively. The ratio of the decay rate with tunneling to that without tunneling is 2.9. When the OH stretch mode was excited to v_{OH}=0.5, the tunneling rate is as large as $1.4\text{x}10^{-2}$ ps^{-1} (see the second row of Table XIV). The purely classical rate is not given since we observed only 2 trajectories out of 400 trajectories classically surmounted the barrier.

The ratios of the classical-plus-tunneling rate to that of classical range from 1.5 to 4.7 depending on the initial energy distribution. When the Si-O stretch is initially excited to $\nu_{Si-O}=3$, the purely classical rate constant is $3.0\text{x}10^{-2}$ ps^{-1} and the tunneling corrected rate constant is $1.4\text{x}10^{-1}$ ps^{-1}, a factor of 4.7 larger than purely classical rate. Those results show that tunneling plays an important role in *cis–>trans* isomerization of hydroxysilyene.

We also investigated the *trans–>cis* interconversion process (see Table XV). The trends in Table XV are similar to those in Table XIV. Excitation of the OH stretch mode ($\nu_{OH}=0.5$) yields the slowest rate coefficient ($1.8\text{x}10^{-4}$ ps^{-1}) while excitation of the Si-O stretch mode ($\nu_{SiO}=3$) gives the largest rate, $1.3\text{x}10^{-2}$ ps^{-1}. Again, when the Si-H stretch is excited, the tunneling rate is $3.5\text{x}10^{-3}$ ps^{-1}, which is about 2.6 times larger than that of the HSiO bending excitation. This result is consistent with the classical results discussed above. An interesting result is that classical rate is very small. Very few or no trajectories classically crossed the torsional barrier (less than three out of 800 trajectories). The tunneling rates shown in Table XV are relatively large. For instance, when the Si-O stretch was excited, the calculated tunneling rate is as large as $1.3\text{x}10^{-2}$ ps^{-1}. For the initial excitations of other normal modes, the tunneling rates vary from $1.8\text{x}10^{-4}$ to $3.5\text{x}10^{-3}$ ps^{-1}.

TABLE XV

COMPUTED ISOMERIZATION RATE COEFFICIENTS OF HSiOH (*TRANS-CIS*) AT THE TOTAL ENERGY OF 20 KCAL/MOL

initial distribution						k (ps^{-1})	
v_{O-H}	v_{Si-H}	v_{HSiO}	v_{Si-O}	v_{HOSi}	v_τ	k_C	k_{C+T}
0.12	0.24	0.48	0.52	0.62	0.73	0.0	2.1×10^{-3}
0.5	0	0	0	0.62	0.73	0.0	1.8×10^{-4}
0	1	0	0	0.62	0.73	0.0	3.5×10^{-3}
0	0	2	0	0.62	0.73	0.0	9.1×10^{-4}
0	0	0	3	0.62	0.73	0[a]	1.3×10^{-2}

a. The rate is too slow to be evaluated on the timescale of the calculations.

One of the reasons that the tunneling contributions are so significant is that the tunneling modes were initially excited. From Eq. (II-22) we know that the individual tunneling probability is directly related to how much energy is in the tunneling coordinates. Since a small amount of the energy (about 1 kcal/mol) was partitioned into each of the tunneling coordinates at the beginning of the trajectories, we wanted to determine how much the tunneling rate was facilitated by this initial energy. This was done by a simple model calculation. We assumed that the HOSi bending and torsional modes were isolated from other vibrational modes so that we could directly evaluate the tunneling probability by computing the action integral of Eq. (II-22). Due to the fact that the averaged tunneling rate along the HOSi bending channel is significantly larger than the rate along the torsional channel (the details are addressed in the next two paragraphs), we only considered the HOSi bending channel. The same amount of the energy (ZPE plus the excitation energy) was partitioned into the HOSi bending mode as it was done in the calculations shown in Table XV. The effective mass of the HOSi bend was assumed to be the same as the value evaluated at the equilibrium geometry for 1/G(HOSi,HOSi); the tunneling probability was then calculated to be 1.02×10^{-12} via the HOSi channel. This result indicates that the initial "excited" tunneling modes are, at least qualitatively, not a major factor in the tunneling effect. Thus, we needed to look further to determine other factors such as the potential energy surfaces, the effective mass, and the rate of the intramolecular energy transfer.

The potential energy surface used opens both the HOSi in-plane bend and the internal rotation channels for the interconversion. It might be interesting to ask questions such as "Do the two isomerization channels play the same roles?" if not "Which channel is more important ?" We discussed previously that no trajectories classically surmounted the HOSi bending barrier due to the centrifugal force. We may then immediately conclude that the torsional channel is dominant, however, our results indicate that the HOSi in-plane bend plays a more important role than does the torsional channel, especially for the *trans*→*cis* isomerization at low excitation energy levels.

The computed values of the "branching ratio" for the two isomerization channels (HOSi in-plane bend and torsion) are shown in Table XVI.

TABLE XVI

THE BRANCHING RATIO OF HSiOH ISOMERIZATION AT 20 KCAL/MOL TOTAL ENERGY

initial distribution						k_{HOSi}/k_{τ}	
$\nu_{O\text{-}H}$	$\nu_{Si\text{-}H}$	ν_{HSiO}	$\nu_{Si\text{-}O}$	ν_{HOSi}	ν_{τ}	*cis→trans*	*trans→cis*
0.12	0.24	0.48	0.52	0.62	0.73	1.3	4
0.5	0	0	0	0.62	0.73	0.7	4
0	1	0	0	0.62	0.73	1.1	14
0	0	2	0	0.62	0.73	0.5	18
0	0	0	3	0.62	0.73	2.4	21

The largest "branching ratio" k_{HOSi}/k_{τ}, is 21 when the Si-O stretch is initially excited to $\nu_{Si\text{-}O}=3$ for the trajectories initiated in the *trans*-well. Overall, the rates of isomerization via the HOSi bending are 4 to 21 times larger than via the torsional channel for *trans–>cis*. These results suggest that the interactions between the torsional and other vibrational modes are relatively weak, the HOSi bend, on the other hand, strongly interacts with rest of the modes. The rates of tunneling through the torsional mode are very competitive to the rates through the HOSi in-plane bending mode for *cis→trans*. The branching ratio k_{HOSi}/k_{τ} for the *cis–>trans* varies from a factor of 0.6 to 2.5 depending upon the mode initially excited.

Why is the tunneling effect via HOSi in-plane bending channel so large that it almost governs the rate of isomerization of HSiOH although the HOSi bending barrier height is only 0.25 kcal/mol lower than that of the torsional barrier? There are a couple of factors which can explain this. First, the width of the HOSi barrier (see Fig. 2) is narrower than that of the torsional barrier (see Fig. 3). From Eq. (II-22) we know, the narrower the barrier, the larger the tunneling probability. Second, HSiOH belongs to the C_s point group. Five in-plane vibrational modes have A' symmetry and the torsion is the only out-of-plane mode with A" symmetry.[58,59] The interactions between the modes of the same symmetry type are much stronger than those different symmetry types. That is, the energy transfer between the in-plane modes is much faster than that between the in-plane modes and the out-of-plane mode of the molecule. Those results indicate that we cannot simply ignore the HOSi isomerization channel even if it is "inactive" in the sense of the classical point of views especially when the excitation energy is low.

Since the tunneling rate is proportional to the turning frequency in the direction of the tunneling coordinate and the imaginary tunneling integral, which is a function of the energy and the effective mass $G^{-1}(\tau,\tau)$ as we addressed in chapter IV, it seems important for us to analyze the local properties of the system at the turning points in order to answer questions such as "Which factors: energy, effective mass, or the turning frequency affect the tunneling probability the most ?" We have done this by computing distributions of E_i, $G^{-1}{}_{ii}$ (i corresponding to the HOSi bending or the torsional coordinates), and the times between turning points τ_{tp} in the tunneling coordinates. Figures 16 and 17 show the distributions for bending and torsional tunneling coordinates, respectively, for trajectories initiated in the *cis*–well with OH stretch excitation (ν_{OH}=0.5) and 20 kcal/mol total energy; panels (a)-(c) are the distributions of E_{HOSi}, $G^{-1}(HOSi,HOSi)$, τ_{tp}. Figures 18 and 19 contain the same quantities as Figs. 16 and 17 except the Si-O stretch is initially excited ($\nu_{Si\text{-}O}$=3).

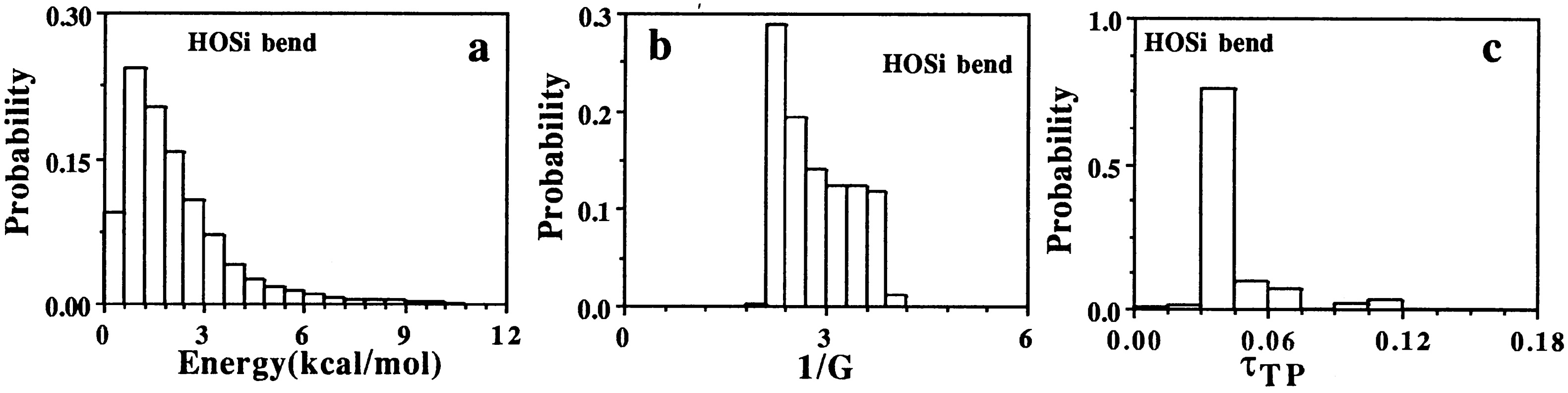

Figure 16. Plots of the Normalized Distributions for Trajectories Initiated in the *Cis*–well and the OH Stretch Being Excited to v_{OH}=0.5 with Total Energy 20 kcal/mol. (a) Energy in the HOSi Bend Coordinate at the Turning Points (b) Same as (a) Except that the Distribution is for the Effective Mass. (c) Same as (a) Except that the Distribution is for the Times Between the Turning Period.

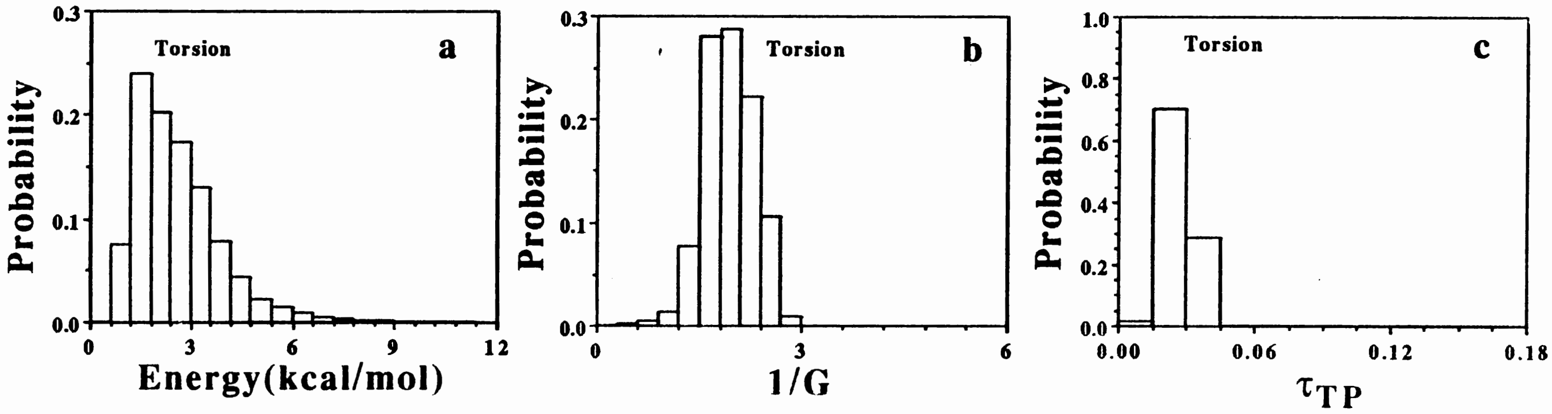

Figure 17. Same as Fig. 16 Except that the Distributions are for the Torsional Coordinate.

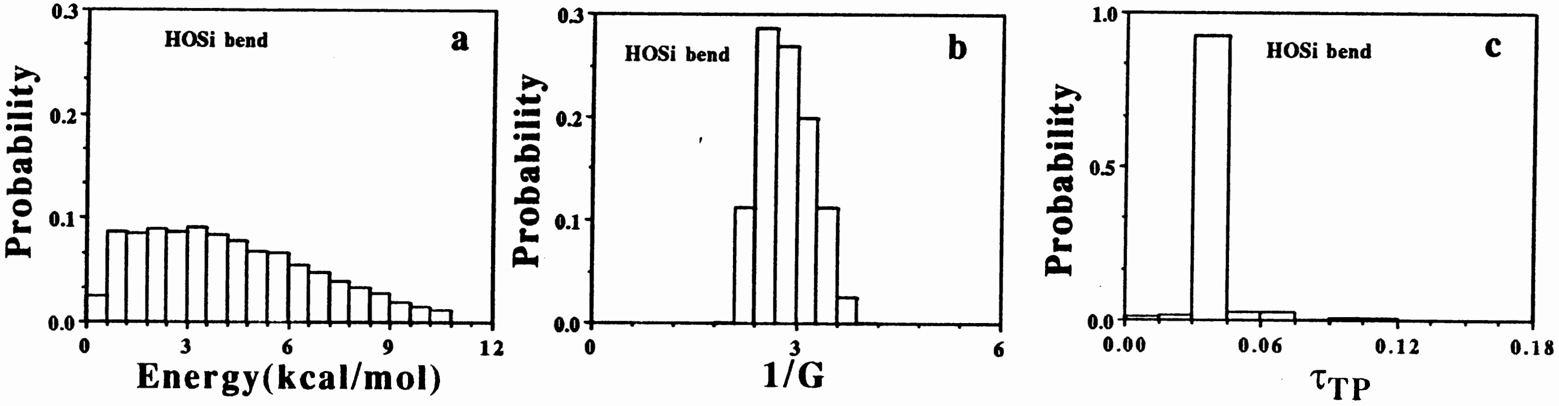

Figure 18. Same as Fig. 16 Except that the Si-O Stretch is Initially Excited to $\nu_{Si\text{-}O}=3$.

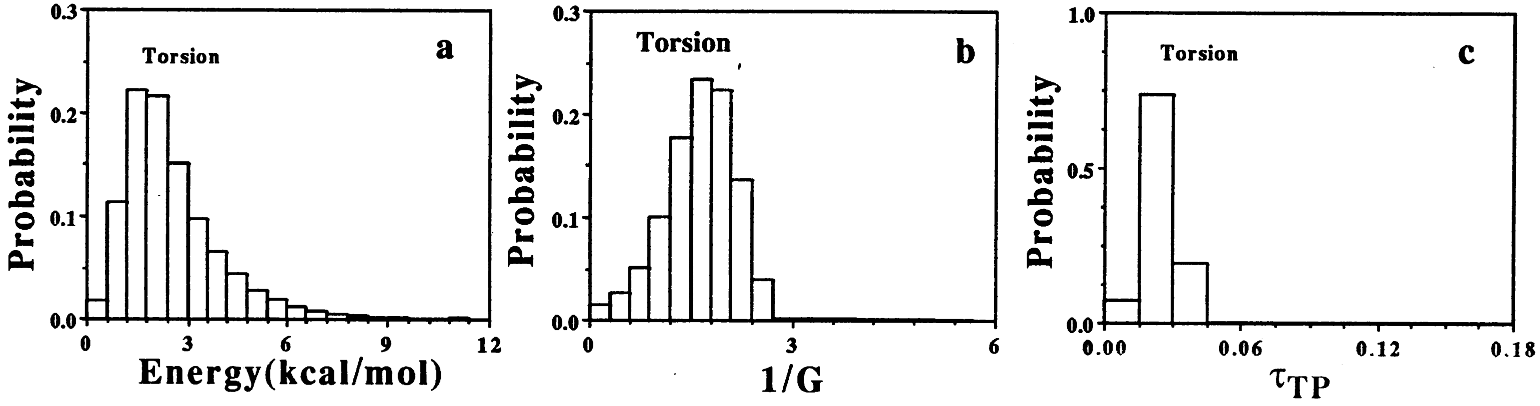

Figure 19. Same as Fig. 17 Except that the Si-O Stretch is Initially Excited to $v_{Si\text{-}O}=3$.

Although the total energy of the ensembles from which Figs. 16 to 19 are derived is the same, the tunneling rates differ by an order of the magnitude and the "branching ratio" of the two channels varies from a factor of 0.7 to 2.4 (see Table XVI). Comparison of the individual panels of Figs. 16 and 17 with the corresponding ones in Figs. 18 and 19 help to explain the large difference in the tunneling rates and branching ratios.

The normalized distribution of energy in the HOSi bending channel (see panel (a) of Fig. 16) is similar to the distribution of the out-of-plane torsion channel (see panel (a) of Fig. 17). The most probable values are 1.2 kcal/mol and 1.8 kcal/mol for panel (a) of Figs. 16 and 17, respectively. However, the distributions of the energy in panel (a) of Figs. 18 and 19 are quite different. As is evident from panel (a) of Fig.18, the overall shape of the distribution is much broader than panel (a) of Fig.19. This indicates that more energy flows into the HOSi bending coordinate when the Si-O stretch was excited initially (see panel (a) of Fig. 18) than it does when the O-H stretch was populated (see panel (a) of Fig. 16). The distribution of the panel (a) of Fig. 17 is slightly broader than that of the corresponding one in Fig. 19. This also shows that the intramolecular energy transfer is significantly favored by the interactions between the in-plane modes but little favored by the interactions between the in-plane modes and out-of-plane mode. The stronger the interactions between the excited modes and the tunneling modes are, the broader the distribution of the energy in the tunneling coordinate. Consequently, the tunneling probability is significantly increased along the HOSi bending coordinate.

The distribution of the effective mass along the tunneling coordinates is more interesting. Panels (b) of the Figs. 16 to 19 represent the distributions of the effective mass for trajectories initiated in the *cis* well. When the OH stretch was excited, the ranges of the effective mass is from 0.025 to 2.85 au^{2}amu for the torsional channel (see panel (b) of Fig. 16) and 1.95 to 4.05 au^{2}amu for the HOSi bending channel (see panel (b) of Fig. 17), respectively. Equation (II-22) indicates that the smaller the effective mass is, the larger the tunneling probability. That is, the magnitude of tunneling along the torsional channel will be facilitated by the effective mass of the torsional channel. The numerical results indicate that the branching ratio k_{HOSi}/k_τ is 0.7 (see the second row of the Table XVI). That is, the tunneling rate via torsional motion is about 1.4 times larger than the tunneling via HOSi bend.

The distributions of the effective mass G^{-1}(HOSi, HOSi) of the HOSi bending channel and $G^{-1}(\tau,\tau)$ of the torsional channel are in panels (b) of Figs. 18 and 19, respectively, for the Si-O stretch initial excitation $v_{Si\text{-}O}=3$. The distribution in panel (b) of Fig. 18 is slightly shifted to the right. This shift corresponds to decreasing the tunneling probability. The distribution of the effective mass $G^{-1}(\tau,\tau)$ of the torsional channel is significantly shifted to lower values. Consequently, the tunneling along the torsional channel is greater. The numerical results indicate that the tunneling rate along the HOSi bending channel is 2.4 times larger than that along the torsional channel when the Si-O stretch is initially excited (see Table XVI) although the distributions of effective mass G^{-1}(HOSi,HOSi) is not in favor of the tunneling via the HOSi bending channel. These results shows that the magnitude of the energy in the tunneling coordinate plays an important role in determining the magnitude of the tunneling rate.

Further insight into the tunneling mechanism can be obtained by from the distribution of times between turning points τ_{TP} for an ensemble of trajectories. Panels (c) of Figs. 16 and 17 show the distributions of the τ_{TP} along the HOSi bending and the torsional coordinates, respectively. The most probable values are 0.025 ps (panel (c) of Fig. 17) and 0.0375 ps (panel (c) of Fig. 16) although the value of the fundamental vibrational frequency of the torsional mode is lower than that of the HOSi bending mode. The torsional mode is two-fold degenerate, thus the τ_{TP} along the torsional channel is much shorter than along the HOSi bending channel. It can be seen that the distribution along the dihedral coordinate (see panel (c) of Fig. 17) is much narrower than along the HOSi bending coordinate (see panel (c) of Fig. 16). This indicates that the torsional mode is relatively decoupled from the rest of the modes of the molecule because the symmetries are different. Since the excitation energy in this set of calculations were relatively low (about 7 kcal/mol), the symmetries of the modes may be very important for vibrational energy transfer. Similar pictures are obtained when the Si-O stretch was excited (see Panels (c) of Figs. 18 and 19). The differences between the panel (c) of Fig. 16 and the corresponding one in Fig. 18 are small and they are even smaller between panels (c) Figs. 17 and 19, though the tunneling rate constant for the Si-O stretch excitation is an order of the magnitude larger than for the O-H stretch excitation. Those results suggests that the individual tunneling probabilities play a more important role than the times between turning points τ_{TP}.

We also examined the same quantities for *trans–>cis* isomerization of HSiOH. Figures 20–23 are the same as Figs. 16–19 except for the former the trajectories were initiated in the *trans*-well. The main characteristics of Figs. 20–23 are essentially the same as Figs. 16–19 except that the distributions in Figs. 20–23 are relatively narrower than those in Figs. 16–19. This is simply because that the potential and kinetic couplings are stronger and the rate of the energy transfer is faster in the *cis–>trans* process than those of the *trans→cis*.

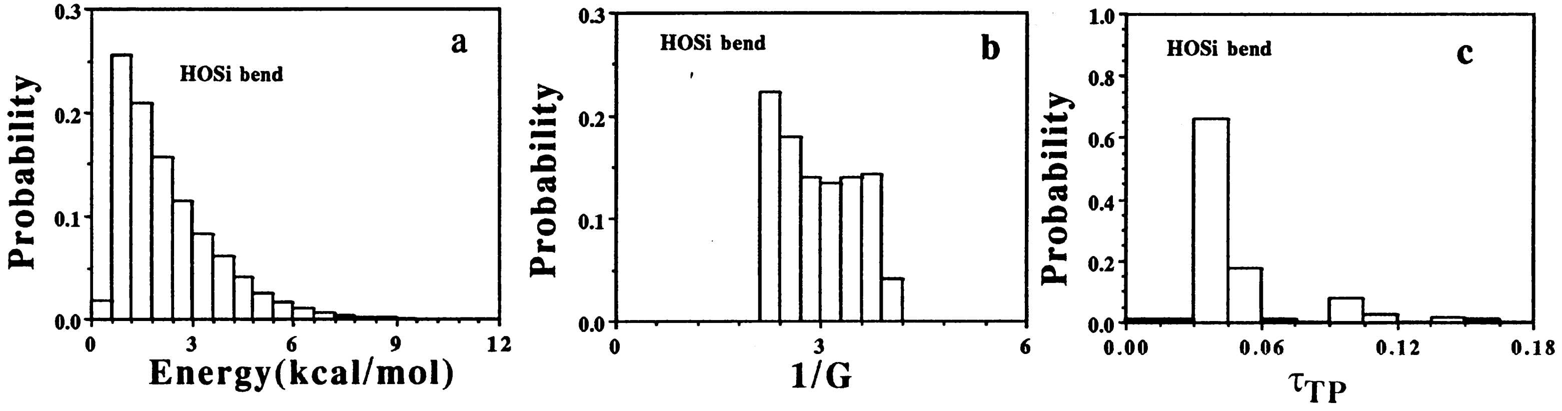

Figure 20. Same as Fig. 16 Except for the Trajectories Initiated in the *Trans*–well.

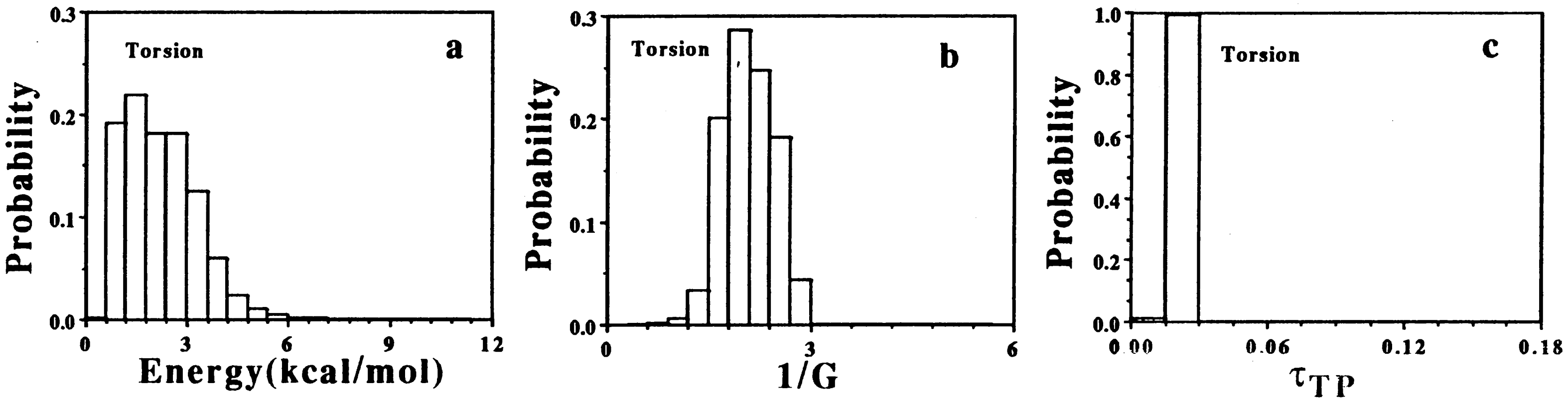

Figure 21. Same as Fig. 17 Except for the Trajectories Initiated in the *Trans*–well.

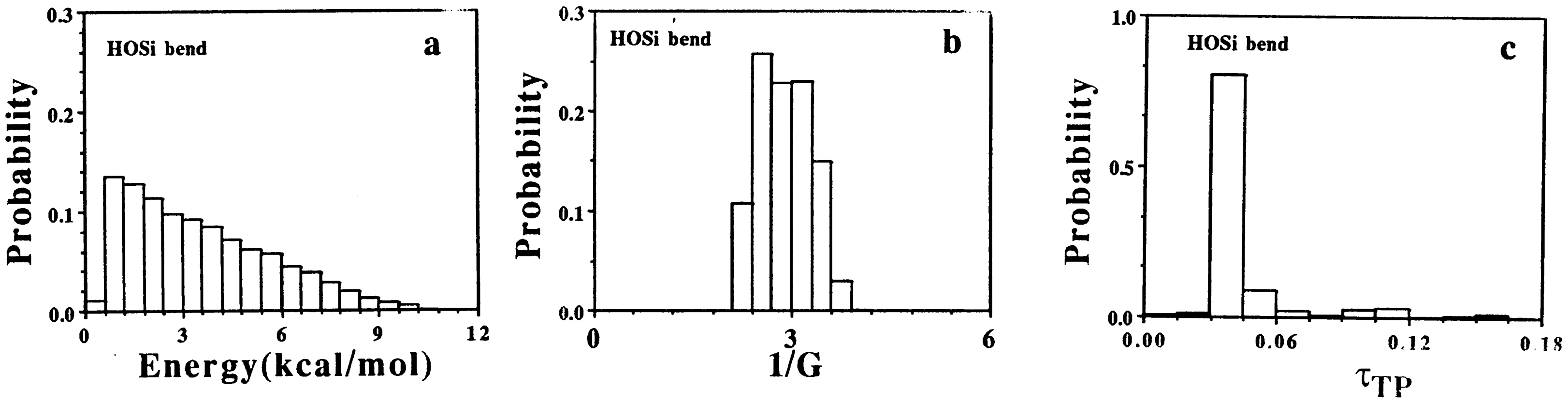

Figure 22. Same as Fig. 18 Except for the Trajectories Initiated in the *Trans*–well.

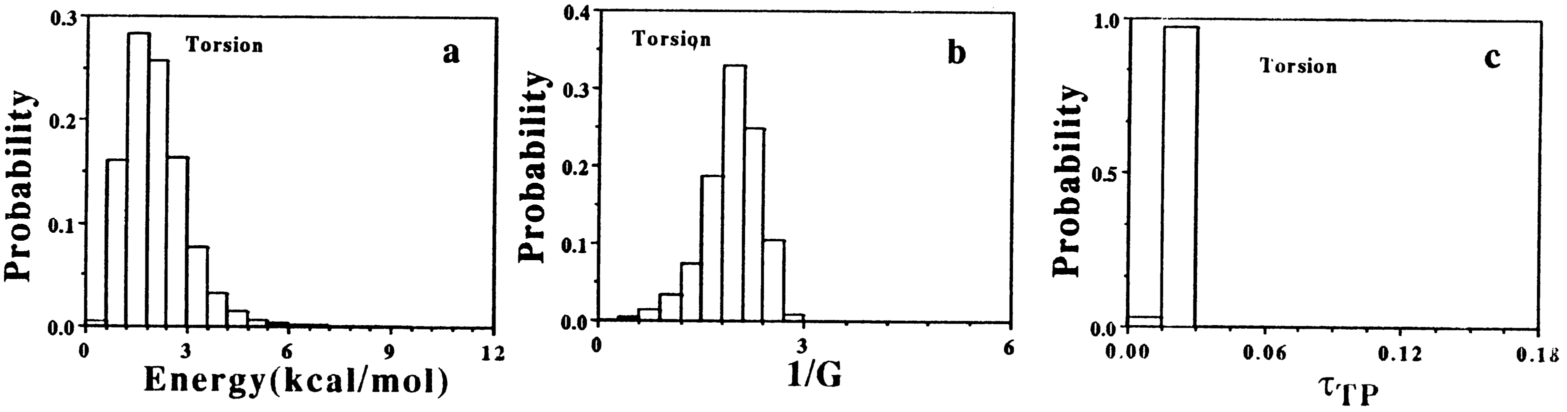

Figure 23. Same as Fig. 19 Except for the Trajectories Initiated in the *Trans*–well.

The above results give qualitative information of the roles of the energy in the tunnel modes, the effective mass, and the times between turning points in the tunneling coordinates for the tunneling rates. In order to get more quantitative knowledge of the tunneling process, the tunneling probabilities are plotted as a function of the effective mass and the energy in the tunneling coordinates at the turning points. There were 20000-50000 turning points collected in each ensemble of the trajectories. It is difficult to plot such a large number of points on a single graph and the range of the individual tunneling probability spans roughly 14 orders of magnitude (from e^{-30} to 1). Thus, we did not attempt to represent the full set of data since the contributions of the many individual tunneling probabilities were very small from an ensemble of the trajectories and plotted them.

Figures 24 and 25 are the "scatter plots" of the natural logarithm of the individual tunneling probabilities versus the energy in the tunneling coordinate (see panels (a) of Fig. 24 and 25) and the effective mass (see panel (b) of Fig. 24 and 25) of the tunneling coordinates. The initial conditions are the same as in Fig. 16. The tunneling probability approximately "monotonically" increases with increasing energy in the HOSi tunneling coordinate (see the panel (a) of Fig. 24). When the value of the tunneling probability is less than e^{-10}, the effective mass G^{-1}(HOSi,HOSi) begins to play a role and becomes more important. Thus, the $\ln(P_{tun})$ versus energy shows "spread". That is, the $\ln(P_{tun})$ no longer "linearly" depends on the amount of energy in the tunneling coordinate. Similar behavior is found when we examine the $\ln(P_{tun})$ versus energy in the torsional mode (see Panel (a) of Fig. 25) except that the points are more "scattered" in the torsional channel than in the HOSi bending channel. We note that there are some turning points with a small amount of energy but large tunneling probabilities due to the effective masses.

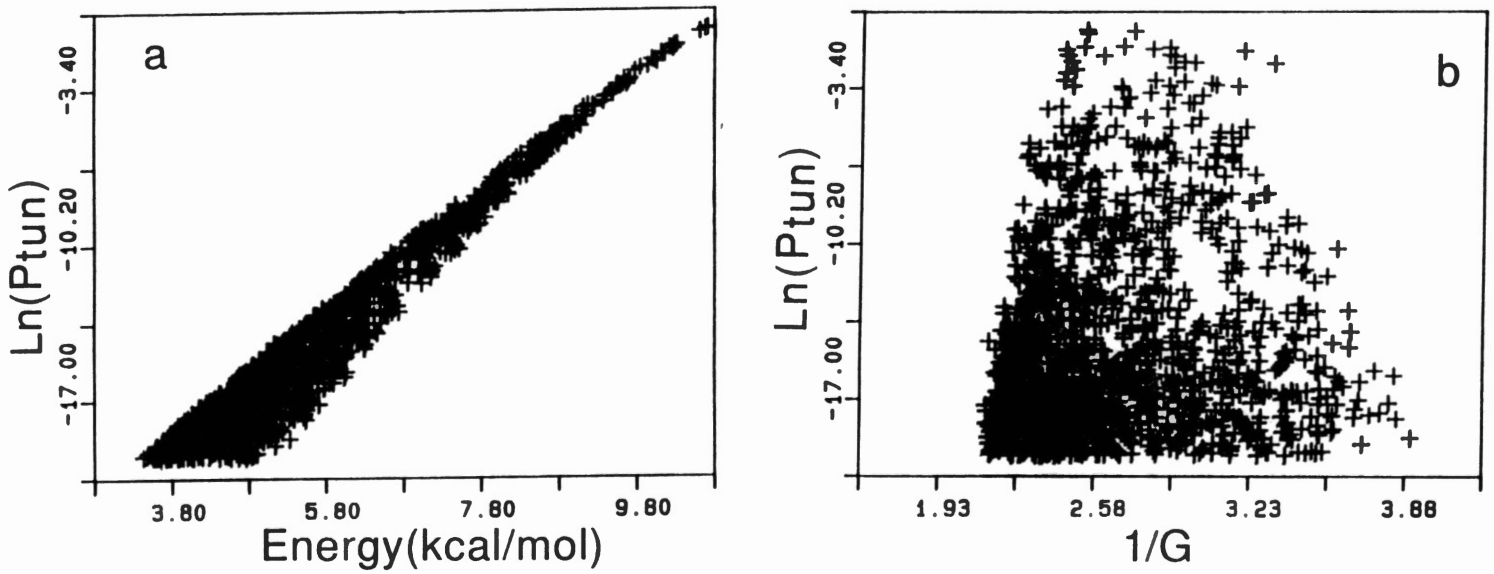

Figure 24. Scatter Plots for *Cis*–HSiOH Initially Excited to v_{OH}=0.5. (a) The Natural Logarithm of the Tunneling Probabilities versus the Energy of the HOSi Bending Coordinate (b) Same as (a) Except that Abscissa is the Effective Mass of the HOSi Bending Coordinate Evaluated at the Classical Turning Points.

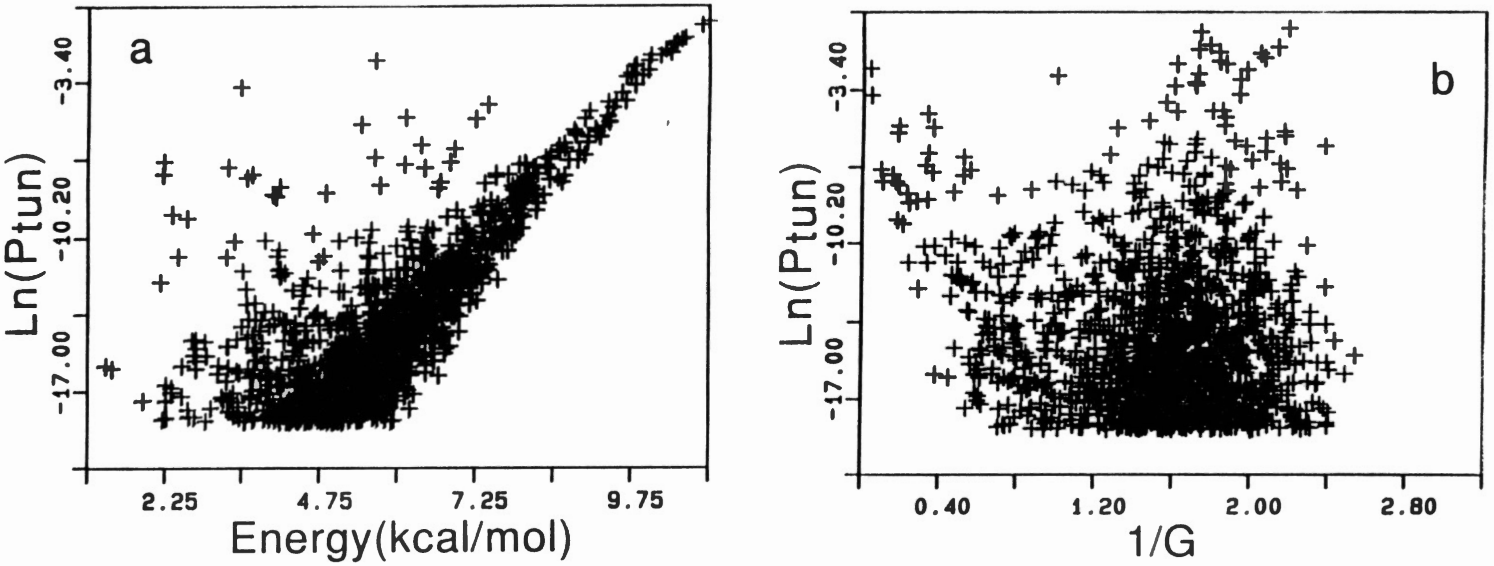

Figure 25. Same as Fig. 24 Except that the Scatter Plots are Corresponding to the Torsional Coordinate.

Figures. 26 and 27 are the same as Figs. 24 and 25 except that the Si-O stretch is initially excited to $v_{Si\text{-}O}=3$. It is helpful to make comparisons between Figs. 24 and 26 as well as Figs. 25 and 27 to refine our knowledge of the tunneling process. When the Si-O stretch was excited, the plot of the $\ln(P_{tun})$ versus the energy in the HOSi bending coordinate (panel (a) of Fig. 26) looks like similar to the corresponding one in Fig. 24. The scattered points in panel (a) of Fig. 26 are limited to a smaller and narrower region than those in panel (a) of Fig. 24. There are more tunneling points in the top or close to the top of the HOSi bending potential barrier for the Si-O stretch excitation than those for the O-H stretch excitation. Thus the tunneling rate for the later case (the Si-O stretch excitation) is expected to be larger than in the former case (the O-H stretch excitation).

The same conclusion can be drawn when comparisons of plots of $\ln(P_{tun})$ versus effective masses are made for different initial conditions. In general, the values of the effective mass of the HOSi bending coordinate 1/G(HOSi,HOSi) vary from 2.1 to 3.8 au^2amu for most of the selected turning points. This indicates that the effective masses along the HOSi bending coordinate do not favor tunneling. Instead, the values of the effective masses along the torsional coordinate are much favorable to the tunneling because the magnitude of the effective masses is significantly smaller in the torsional channel than that in the HOSi bending channel. The distribution of the effective mass $G^{-1}(\tau,\tau)$ in panel (b) of Fig. 24 is similar to those in the corresponding panel of Fig. 26 except that the points are more compressed in the upper region (with large tunneling probabilities) of Fig. 26 than those in panel (b) of Fig. 24. This result suggests that the magnitude of the effective masses of the HOSi channel is relatively independent of the initial excitation. Consequently, the rate of the energy transfer from bath modes to the HOSi bending mode dominates the tunneling rate. The distribution of the effective mass of the torsional channel $1/G(\tau,\tau)$ is, however, significantly shifted along in the direction of lower magnitudes of $1/G(\tau,\tau)$ for the Si-O stretch initial excitation, which can be seen by comparing panel (b) of

Fig. 25 to the corresponding panel of Fig. 27. That is, the effective masses of the torsional coordinate significantly facilitate tunneling.

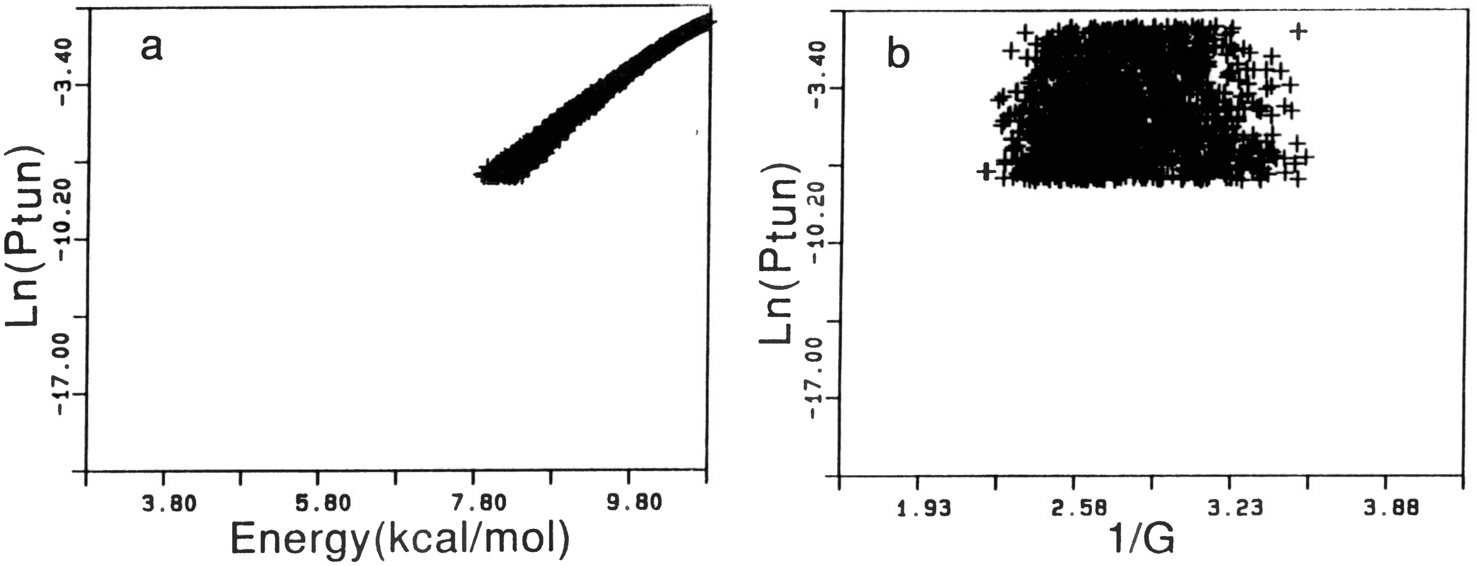

Figure 26. Same as Fig. 24 Except that the Si-O Stretch is Initially Excited to $\nu_{Si\text{-}O}=3$.

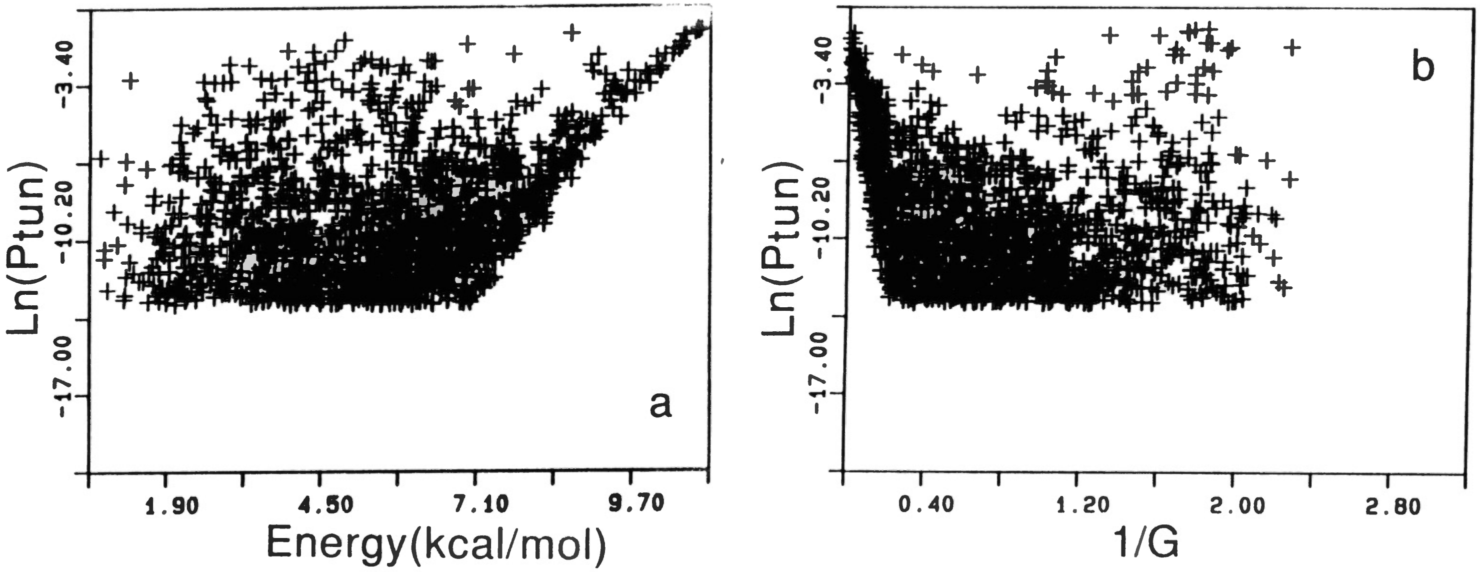

Figure 27. Same as Fig. 25 Except that the Si-O Stretch is Initially Excited to $\nu_{Si\text{-}O}=3$.

Since the effective mass is such important to the tunneling along the torsional channel we would like to explore the quantities of $1/G(\tau,\tau)$. We can write $G^{-1}(\tau,\tau)$ as a function of the internal coordinates[71]:

$$
\begin{aligned}
G(\tau,\tau) = {} & \left(\frac{1}{r_{H\text{-}Si}\sin(\theta_{HSiO})}\right)^2\left(\frac{1}{m_{Si}}+\frac{1}{m_H}\right) + \left(\frac{1}{r_{H\text{-}O}\sin(\theta_{HOSi})}\right)^2\left(\frac{1}{m_O}+\frac{1}{m_H}\right) \\
& + \frac{1}{r^2_{Si\text{-}O}}\left[\cot^2(\theta_{HSiO})+\cot^2(\theta_{HOSi})\right]\left(\frac{1}{m_{Si}}+\frac{1}{m_O}\right) \\
& + \frac{2\cos(\tau)}{r^2_{Si\text{-}O}}\cot(\theta_{HSiO})\cot(\theta_{HOSi})\left(\frac{1}{m_{Si}}+\frac{1}{m_O}\right) \\
& - \frac{2\cos(\tau)}{r_{Si\text{-}O}}\left[\frac{\cot(\theta_{HOSi})}{r_{H\text{-}Si}\sin(\theta_{HSiO})m_{Si}}+\frac{\cot(\theta_{HSiO})}{r_{H\text{-}O}\sin(\theta_{HOSi})m_O}\right. \\
& - \frac{2}{r_{Si\text{-}O}}\left[\frac{\cot(\theta_{HSiO})}{r_{H\text{-}Si}\sin(\theta_{HSiO})m_{Si}}+\frac{\cot(\theta_{HOSi})}{r_{H\text{-}O}\sin(\theta_{HOSi})m_O}\right].
\end{aligned}
\tag{V-1}
$$

From Eq. (V-1), we know that when the value of the θ_{HSiO} or θ_{HOSi} or both approaches 0° or 180°, the value of $G(\tau,\tau)$ becomes very large and the inverse of $G(\tau,\tau)$, therefore becomes extremely small. From Eqs. (II-17) and (II-22) we know that the tunneling probability depends not only on the amount of the energy in the tunneling coordinate, but also on the value of the effective mass at the turning points. The above analysis suggest that the change of the effective mass due to the dynamics may facilitate or hinder the tunneling probability significantly.

Similar plots were obtained when the trajectories were initiated in the *trans* well. They are shown in Figs. 28–31. The characteristics of Figs. 28–29 and 30–31 are essentially the same as the corresponding ones of Figs. 24–25 and 26–27 except that the magnitudes of the tunneling probabilities in Figs. 28–29 and 30–31 are smaller than those of Figs. 24–25 and 26–27 due to the fact that the interactions of bath modes to the tunneling modes of the *cis* HSiOH are stronger than those of the *trans* HSiOH.

Another interesting point regarding these results are mode-specific effects. Since the total energy of the system are the same, the RRKM theory predicts that the same isomerization rate should be observed. However, the rate constants corresponding to the Si-O stretch excitation are one and two orders of magnitude larger than those of the OH stretch excitation for the reactant initiated in the *cis* and *trans* wells, respectively. The O-H stretch excitation results in the slowest isomerization rate while the Si-O stretch excitation yields the largest rate constant in both *cis*→*trans* and *trans*→*cis* isomerizations. These conclusions are valid for both classical and classical-plus-tunneling results. That is, both *cis*–>*trans* and the reverse process are highly mode specific.

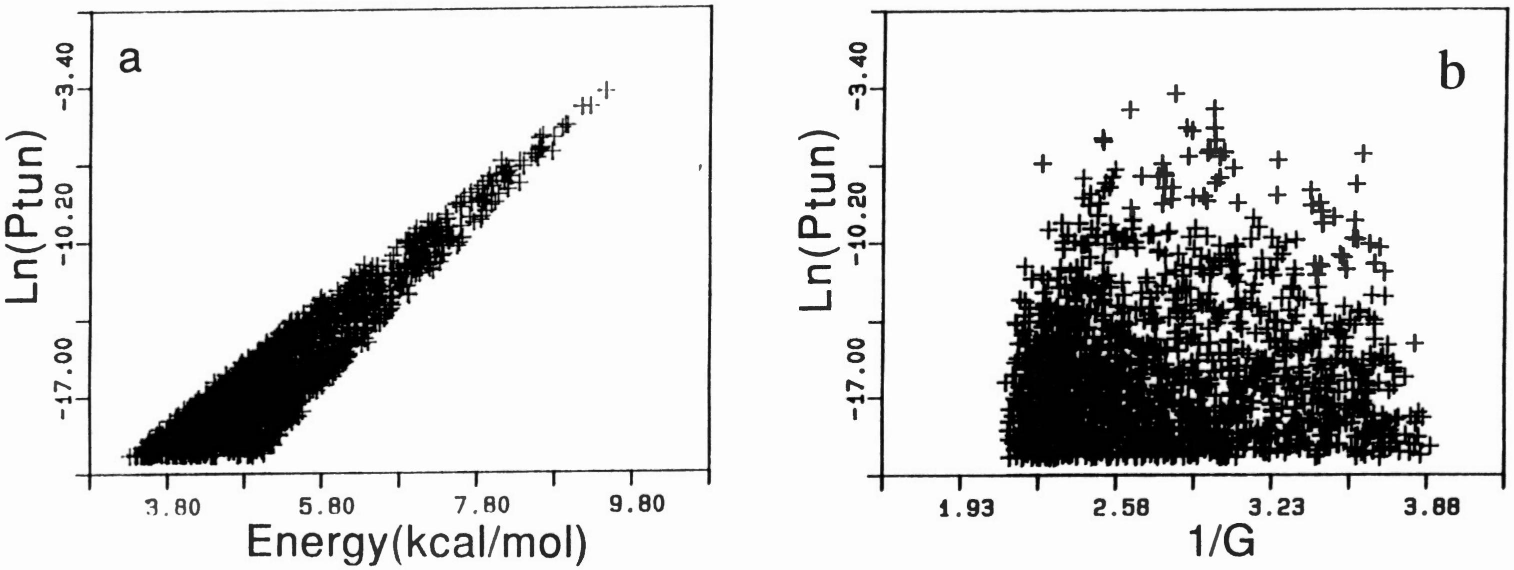

Figure 28. Same as Fig. 24 Except for the Trajectories Initiated in the *Trans*–well.

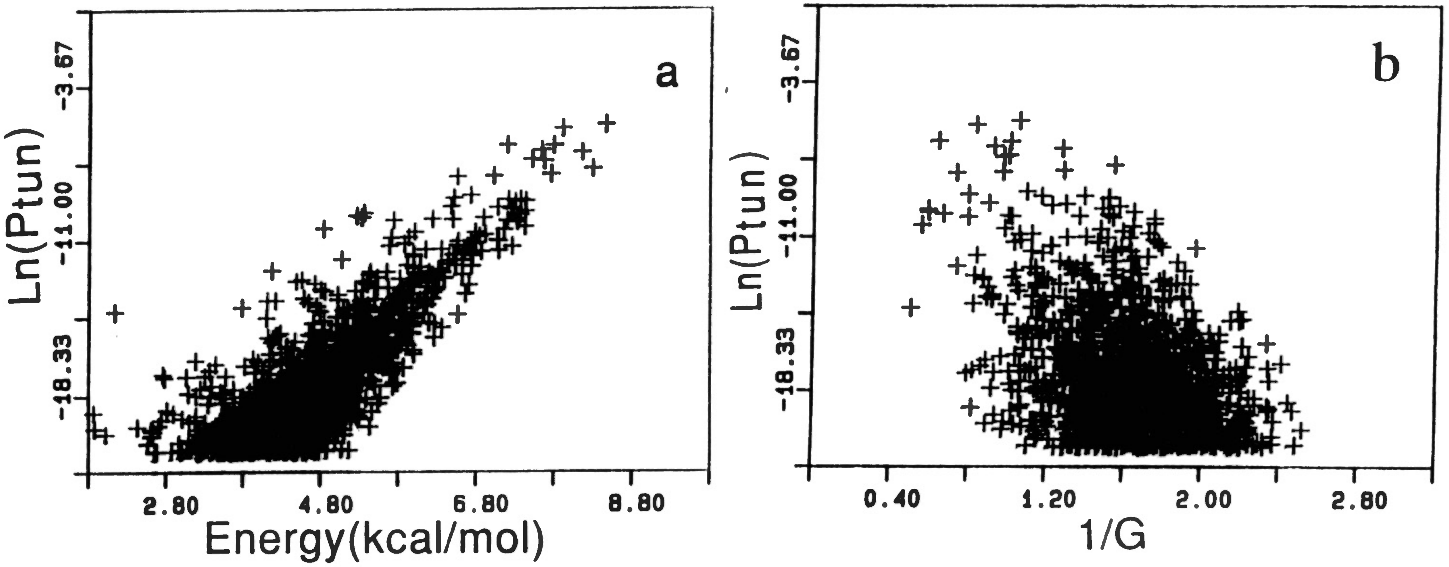

Figure 29. Same as Fig. 25 Except for the Trajectories Initiated in the *Trans*–well.

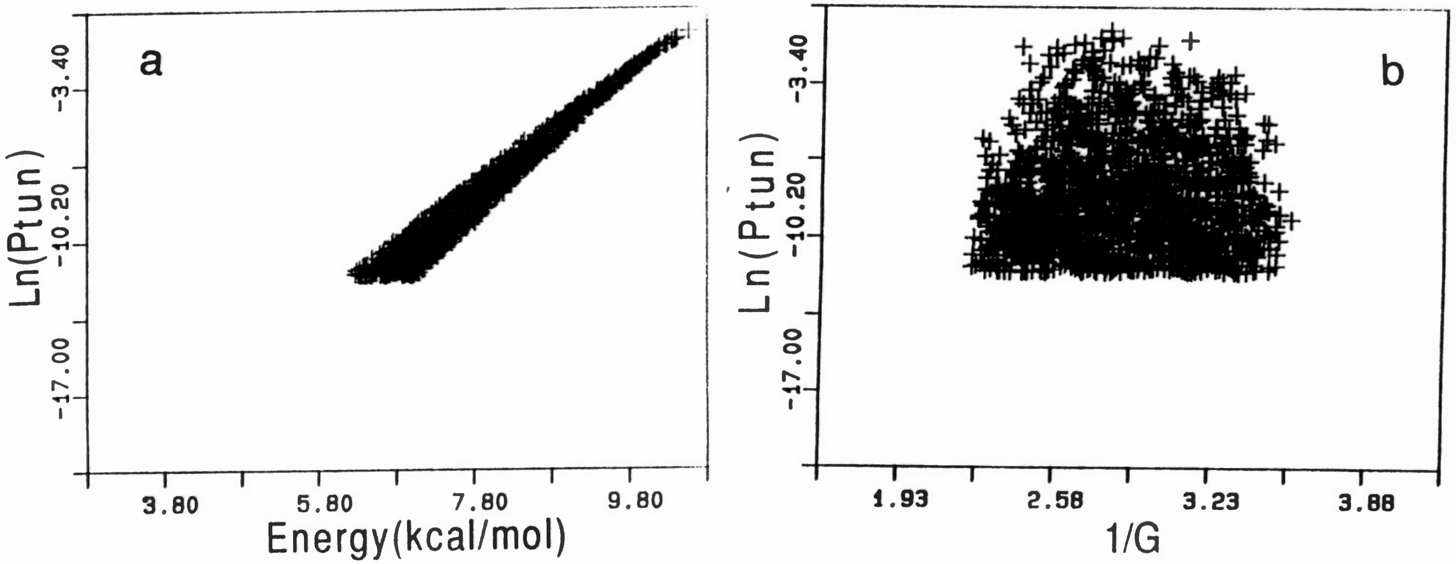

Figure 30. Same as Fig. 26 Except for the Trajectories Initiated in the *Trans*–well.

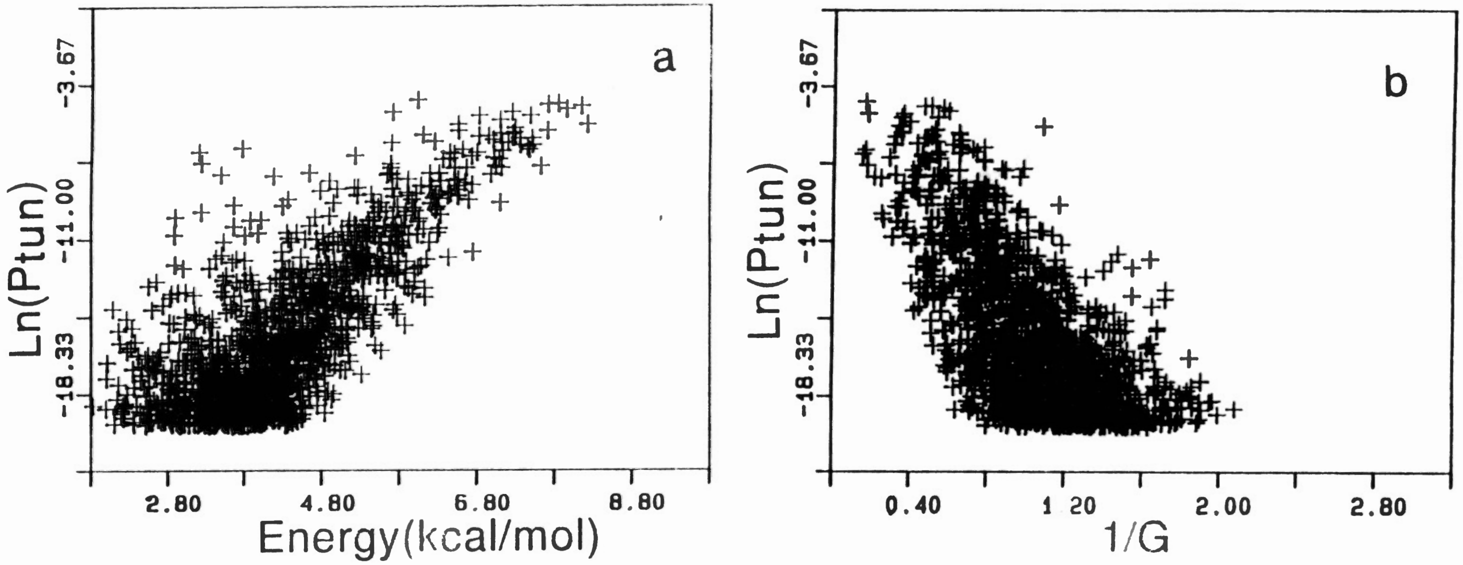

Figure 31. Same as Fig. 27 Except for the Trajectories Initiated in the *Trans*–well.

Excitation Energy Effects

It is well-known that tunneling effects are strongly dependent on the energy of the system.[2] We calculated the isomerization rate constant as a function of the energy to investigate how the magnitude of excitation energy affects the tunneling rate. Table XVII summarizes our results.

TABLE XVII

COMPUTED ISOMERIZATION RATE COEFFICIENTS OF HSiOH VERSUS TOTAL ENERGY

Energy (kcal/mol)	*cis->trans*			*trans->cis*		
	k_C	k_{C+T}	k_C/k_{C+T}	k_C	k_{C+T}	k_C/k_{C+T}
15	0.0	$1.5x10^{-3}$	0.0	0.0	$8.0x10^{-7}$	
20	$7.4x10^{-3}$	$5.4x10^{-2}$	7.3	0.0	$1.8x10^{-4}$	
25	$6.0x10^{-2}$	$2.4x10^{-1}$	4.0	0.0	$1.1x10^{-2}$	
30	$1.8x10^{-1}$	$5.2x10^{-1}$	2.9	$2.7x10^{-2}$	$1.1x10^{-1}$	4
35	$4.0x10^{-1}$	$6.7x10^{-1}$	1.7	$1.8x10^{-1}$	$3.3x10^{-1}$	1.8

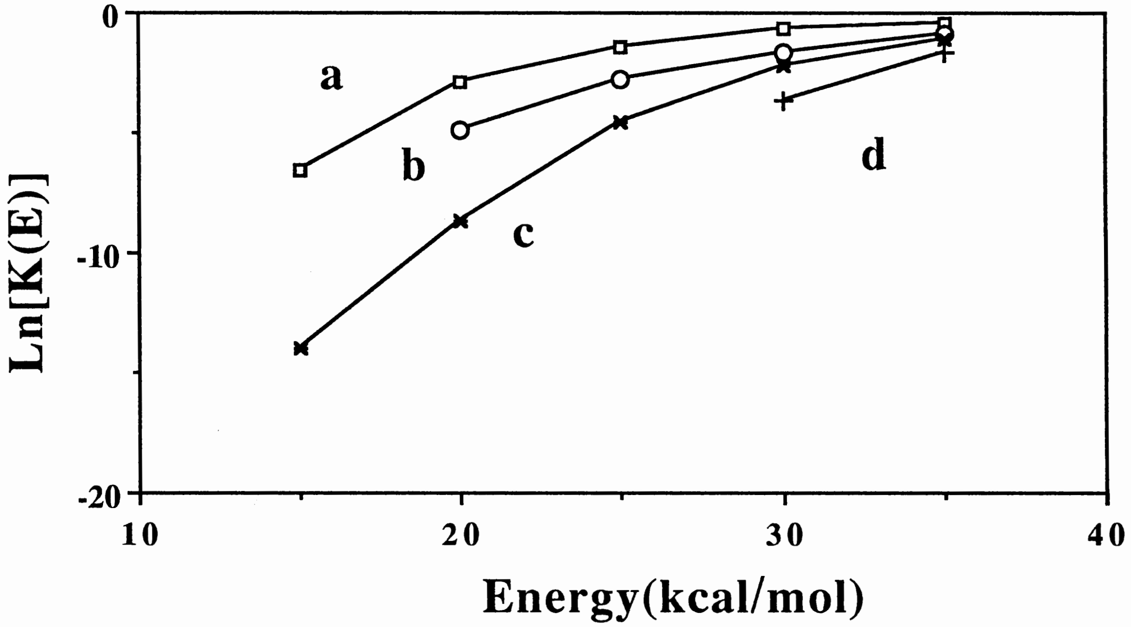

Figure. 32 A Plot of the Rate Constants Versus Total Energy. Curves (a) and (b) are Corresponding to Classical-plus-tunneling and Purely Classical Rate Constants for Trajectories Initiated in the *Cis* well and Curves (c) and (d) are the same as Curves (a) and (b) Except Trajectories Initiated in the *Trans* well.

In order to make a more direct comparison, we plotted the nature logarithm of the decay rate constants ln(k(E)) as a function of the total energy of the system (see in Fig. 32). Ensembles of 800-1000 trajectories were calculated and the excitation energy was equally partitioned into all the vibrational modes except the HOSi bending and the torsional modes. Curve (a) of Fig. 32 represents the classical-plus-tunneling rate constant for trajectories initiated in the *cis* well versus the total energy of the system, and curve (b) is the purely classical results. Curves (c) and (d) correspond to curves (a) and (b) except the trajectories initiated in the *trans* well. Curve (b) approaches curve (a) as the total energy increases. That is, the tunneling correction becomes less important with the increasing total energy. The same behaviors is seen in curves (c) and (d).

Curve (c) approaches curve (a) when the total energy of the system increases. That is, the ratio of the tunneling rate of the *cis–>trans* to the *trans–>cis* decreases to unity with the increase of the total energy of the system. For instance, the ratio of the tunneling rate of *cis→trans* to the *trans→cis* is 18x10^2 when the total energy of the system is 15 kcal/mol and the ratio goes down to 2 when the total energy of the system increased to 35 kcal/mol.

Figure 32 also shows that the ratio of the classical-plus-tunneling rate to pure classical rate decreases from 7.3 to 1.7 when the excitation energy increases from 7.6 kcal/mol to 22.6 kcal/mol, respectively, for *cis–>trans* isomerization. The same behavior is also found for the *trans–>cis* isomerization. These results indicate that when the HSiOH system is equilibriated, the *trans* isomer will be a dominant species in the system if we assume the equilibrium constant can be represented by:

$$k_{eq}=(k_{cis\text{–>}trans})/(k_{trans\text{–>}cis}) \qquad \text{(V-2)}$$

Supposing the interconversion of *cis→trans* and *trans→cis* is the last step of the reaction Si(^{3}P) + H_2O→HSiOH, and both *cis* and *trans* isomers exist, then our results can be used for partially explaining why the experimentlists[37] failed to observe the *cis* HSiOH in the reaction of Si(^{3}P)+H_2O→HSiOH. Since the calculated tunneling rate is significantly larger for the *cis–>trans* than that of the reverse process, the *cis* HSiOH is supposed to convert to the *trans* HSiOH by tunneling but the reverse process very slow at low temperature.

The branching ratio of the tunneling via HOSi bending channel and the torsional channel and summarized in Table XVIII.

TABLE XVIII

THE BRANCHING RATIO OF THE ISOMERIZATION RATE COEFFICIENTSOF HSiOH VERSUS TOTAL ENERGIES

Energy (kcal/mol)	k_{HSiO}/k_{τ}	
	cis->trans	*trans->cis*
15	$16\text{x}10^2$	$39\text{x}10^2$
20	7	$34\text{x}10^1$
25	2	5
30	1	2
35	0.9	1

It is easy to see from Tables XVII and XVIII that the tunneling effects govern the rate of the isomerization when the total energy of the system is below 25 kcal/mol. When the energy of the system reaches to 30 kcal/mol or above, the isomerization which occurs along the torsional channel becomes important and starts to compete with the HOSi in-plane bending channel. This is reflected by the change of the branching ratio k_{HOSi}/k_{τ} from a factor of $16\text{x}10^2$ to less than one for the *cis–>trans* (see Table XVIII). When the energy of the system is above 35 kcal/mol, however, the large number of classical "events" are a dominant contribution for HSiOH isomerization. The tunneling effects are, eventually, "diminished" by classical results. In other words, the tunneling correction becomes less and less important with increasing excitation energy. The torsional channel will eventually become a dominant reaction path by increasing the total energy of the system. The same behaviors are observed for the *trans→cis* process. When the total energy of the system equals 15 kcal/mol, the ratio of the rate constants k_{HOSi}/k_{τ} is as large as $39\text{x}10^2$. That is, the tunneling via HOSi in-plane bend plays a major role for the *trans-cis* isomerization even though the HOSi in-plane bending channel is classically forbidden.

Summary

We have investigated the *cis-trans* interconversion processes of hydroxysilyene by using classical trajectories with tunneling corrections on a model potential energy surface. The potential energy surface is based upon the available experimental and theoretical data. Two isomerization channels, HOSi in-plane bend and out-of-plane torsion, are allowed

Strong mode-specific behavior is observed. When the total energy is fixed at 20 kcal/mol, the ratio of the rate constants for *cis→trans* to *trans→cis* vary from a factor of 1.5 to 4.7 depending upon the mode initially excited. The Si-O stretch excitations yield the largest rate constants, which are about 10 and 72 times larger than those of the O-H stretch excitation for the *cis→trans* and *trans→cis*, respectively. The OH stretch excitation yields the smallest rate constants for both *cis→trans* and *trans→cis.*

The tunneling effects are found to play an important role for the interconversion in HSiOH. When the total energy is 20 kcal/mol or above, the ratio of the microcanonical rate coefficient with and without tunneling correction is as large as 7.3 for the *cis–>trans* isomerization. Tunneling via HOSi in-plane bending channel is found to be a dominant channel for isomerization at low excitation energy (15~30 kcal/mol). The "branching radio" of the isomerization via HOSi bend to torsional channels k_{HOSi}/k_{τ} is changed from a factor of 4 to 21 depending upon the mode which is initially excited for the *trans–>cis* isomerization. For the trajectories initiated in the *cis* well, the calculated values of the k_{HOSi}/k_{τ} vary from 0.5 to 2.4. These results indicate that the HOSi in-plane bending motion actually governs the tunneling rate of the isomerization in most of the cases. Therefore, the HOSi bending channel cannot be ignored even though it is classically forbidden.

Several important factors, such as the effective mass, the inverse G-matrix element ($G^{-1}(\tau,\tau)$ and G^{-1}(HOSi,HOSi)), and the energy of the tunneling coordinates at the turning points, are examined in detail. The magnitude of the effective mass along the HOSi bending coordinate, 1/G(HOSi, HOSi), are generally larger (about 2 to 4 au^2amu) than the values along the torsional coordinate (0.02 to 3 au^2amu). The effective mass along the torsional coordinate, $1/G(\tau,\tau)$, significantly facilitates the tunneling rate. The efficient intramolecular energy transfer between the HOSi in-plane bending mode and rest of the vibrational modes significantly increases the tunneling rate. Furthermore the interactions between the modes with the same symmetry type is significantly stronger than the modes with the different symmetry types when the excitation energy is low.

We also investigate the tunneling rate as a function of the excitation energy. When the total energy of the system is low (15 kcal/mol or lower), the computed tunneling rate coefficient is three orders of magnitude larger for the *cis→trans* than that for the *trans→cis*. Thus, the *trans*-isomer is a dominant species when the isomerization approaches the equilibrium. The ratio of the tunneling corrected rate to the purely classical rate increases with the decreasing total energy of the system. The branching ratio k_{HOSi}/k_{τ} decreases with increasing excitation energy. These results are in good agreement with the results reported by Ismail[37]. That is, the tunneling is an important factor for the isomerization of HSiOH. When the energy of the system reaches to 30 kcal/mol or above, the tunneling effects becomes less significant and the rates calculated with tunneling correction approach the rates without tunneling correction due to the fact that large number of classical "events" "diminished" tunneling. The ratio of the isomerization rate constants for the *cis→trans* to the reverse process also approaches unity.

CHAPTER VI

CLASSICAL DYNAMICS STUDY OF HONO USING CONSTRAINED TRAJECTORIES

Since the tunneling rate is directly associated with the intramolecular vibrational energy transfer (IVR) we carried out constrained classical trajectory calculations to refine our knowledge of the intromolecular vibrational energy redistribution, *cis–trans* isomerization, and rotation–vibration interactions in HONO. Relaxation of the OH bond stretching mode, initially excited to the second overtone state, was monitored by using a local mode approximation (see Eq. (II–8)). In order to determine the roles of the various modes in the IVR and *cis–trans* isomerization, the dihedral, HON bending, or ONO bending angle was dynamically constrained by incorporating Lagrangian multipliers into Hamilton's equations of motion. The procedure of how to incorperate the constraint into the classical trajectories has been addressed in Chapt II. The potential energy surface used in this study is the same as we described in Eqs. (III-1) to (III-4).

The IVR Mechanism

We have calculated the energy transfer out of the OH stretching mode initially excited to the v = 3 level in *cis*-HONO with unrestricted vibrational motion and with the torsional motion constrained. Trajectories were calculated for initial conditions in which the angular momentum is parallel to the torsional motion since this orientation has the greatest effect on IVR.[53] Ensembles of 30 or 60 trajectories were computed for each set of initial conditions. The total energy of the system was fixed at 1.7 eV. All of the calculations reported here are for HONO initially in the *cis* configuration. We have done the present studies for only the *cis* isomer since the qualitative behavior is essentially the same for the two conformations, although there are significant differences in the rates of IVR and isomerization for the *cis* and *trans* conformers.[52,53]

The ensemble average of the energy in the OH bond, initially excited to the v = 3 level, in nonrotating HONO calculated with and without constrained torsional motion is plotted in Fig. 33(a) as functions of time. The upper curve is for the case where the torsional motion is constrained. The rates of the energy flow out of the OH mode is initially almost the same in both cases; about one-third of the energy initially deposited in the excited mode flows out in about 0.5 ps. However, after this initial period, the rate of energy transfer is much faster in the trajectories in which the torsional motion is included (lower curve in Fig. 33(a)). Thus, the torsional mode plays a significant role in the relaxation of OH overtones in nonrotating HONO on a timescale of several picoseconds.

The results in Fig. 33(b) show the influence of rotation and the effect of constraining the torsional mode on the relaxation of the OH overtone. The lower curve shows the energy in the OH bond as a function of time for unconstrained HONO with molecular rotation about the N-O bond. The rotational energy is 0.04 eV and the total energy is 1.7 eV. The upper curve in Fig. 33(b) is obtained when the torsional motion is constrained. Constraining the torsional motion causes a significantly slower rate of energy transfer after about 0.5 ps; the rate of energy transfer is about the same during that initial period of 0.5 ps for both cases. The frozen torsional motion results in a significant decrease in the relaxation. Only about half as much energy flows out of the OH stretching mode in 4.5 ps when the torsional mode is constrained as does when it is active. The similar rates of energy transfer in the first 0.5 ps suggest that the torsional mode is not involved in the initial relaxation of the OH stretch, but begins to play a role once other modes become populated. The initial step in the relaxation involves transfer of energy to the HON bend, followed by transfer involving the torsional mode. Below we present results that show the influence of bending motion on the energy transfer.

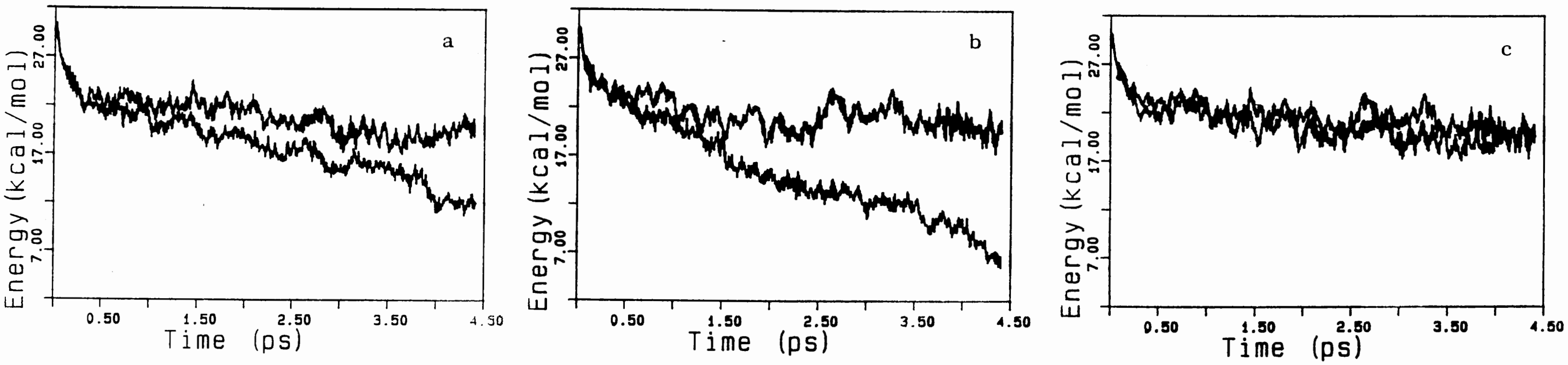

Figure 33. Plots of Ensemble Average of the OH Local–Mode Energy as a Function of Time. (a) The OH Stretch is Initially Excited to v_{OH}=3 in Nonrotating *Cis*–HONO. Upper Curve: Torsional Motion Constrained. Lower Curve: no Constraints. (b) Same as (a) Except 0.04eV of Rotational Energy is Partitioned Parallel to the N-O Bond. (c) Same as (a) Except that the Upper Curve Corresponds to Unstrained Dynamics and Zero Angular Momentum and the Lower Curve is for 0.04 eV of Rotational Energy Parallel to the N-O Bond with the Torsional Motion Constraint.

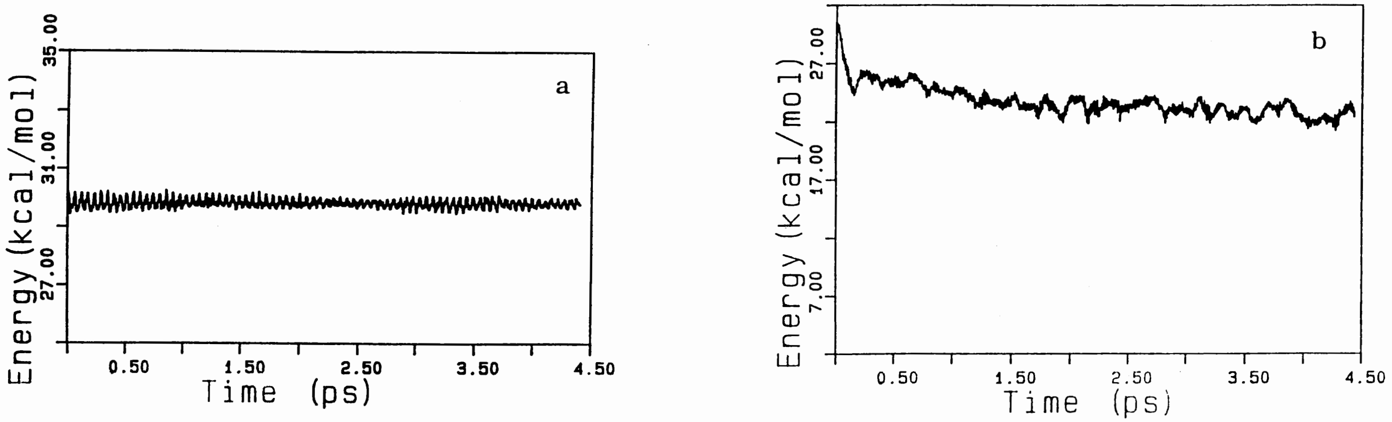

Figure 34. Plots of Ensemble Average of the OH Local–Mode Energy as a Function of Time for The OH Stretch Being Excited to the Second Overtones in Nonrotating *Cis*-HONO. (a) The HON Bending Motion is Constrained. (b) Same as (a) Except that the ONO Bending is Constrained.

It is interesting to compare the energy transfer in nonrotating HONO with that in rotating HONO in which the torsional motion is absent. These results are shown in Fig. 33 (c). Again, the rotational energy is 0.04 eV and the total energy is 1.7 eV. The rotation is parallel to the torsional motion, the orientation that gives the greatest enhancement of IVR.[53] The two curves shown in Fig. 33(c) are essentially identical. Removing the torsional motion eliminates the influence of rotation on the IVR.

These results show that the torsional motion plays an important role in the relaxation following an initial stage (~0.5 ps) of the energy flow from the OH stretch. The initial energy transfer occurs via the OH-HON stretch-bend coupling. The importance of the HON bend can be illustrated by constraining its motion. Figure 34(a) shows the energy in the OH stretch as a function of time for an ensemble of trajectories in which the HON bend is constrained to its equilibrium value. Almost no energy is lost from the OH stretching mode in the 4.5 ps that the trajectories were followed. The same result is obtained whether or not the molecule is rotating. The interaction between the OH stretch and HON bending is very strong and accounts for the relaxation of the OH overtone.

We also examined the influence of the ONO bending on the relaxation of the OH overtone. Figure 34(b) shows the energy in the OH mode as a function of the time with the ONO bending motion constrained. The behavior of this plot is similar to that obtained when the torsional motion is constrained (see the upper curve in Fig. 33(a), except the energy transfer is somewhat slower (Fig. 34(b)).

The fundamental vibrational frequencies of the HON bending and torsional motions are close to a 2:1 resonance, which would seemingly cause efficient energy transfer for the HON relaxation. However, the results show that the rate of OH relaxation is slower when the ONO bending motion is constrained than when the torsional motion is constrained. This suggests that the "nonresonant" interactions between the in-plane ONO and HON bending modes are stronger than those between the in-plane HON bend and the out-of-plane torsional mode. Since the HON bend is the "gateway mode" for the OH relaxation, the mode which couples most strongly with the HON bend would presumably be expected to enhance the OH relaxation.

We have calculated power spectra to aid in understanding the IVR mechanism. Power spectra of the internal coordinates were computed by using Eqs. (II-58) and (II-59) for ensembles of 14 to 30 trajectories. "Cumulative" spectra were obtained by summing the intensities of the spectra of the individual internal coordinates. The resulting spectra are shown in Figs. 35–36; the resolution for each is 11 cm^{-1}. Figure 35(a) serves as a reference spectrum for comparisons with the other spectra in Figs. 35–36. It corresponds to an unconstrained, low-energy trajectory (0.5 kcal/mol) for *cis* -HONO. Figures 35(b)–36 are the spectra for *cis*-HONO with the OH stretching mode initially excited to the second overtone. Panel (b) of the Fig. 35 is for unconstrained HONO, (c) is for HON bending motion constrained, (d) is for the dihedral angle constrained, and (e) is for the ONO bending angle constrained. Panels (a) and (b) of the Fig. 36 are for individual trajectories with the HON bend constrained and initial excitation of the OH stretch to $v_{OH}= 3$.

The spectrum of unconstrained HONO, Fig. 35(b), has broad peaks, indicating strong interactions among the various vibrational modes as well as perhaps some effects due to variations in initial conditions (as discussed below). There is a broad band centered at 2796 cm^{-1}, corresponding to the OH stretch, and five other strong peaks at 1551, 1258, 879, 627, and 527 cm^{-1} corresponding to the N=O stretching , HON bending, N-O stretching, torsional, and ONO bending modes, respectively. All the frequencies are red-shifted due to the anharmonicity of the potential (we will address this problem in more detail below). The six fundamental frequencies are given in Table III for comparison.

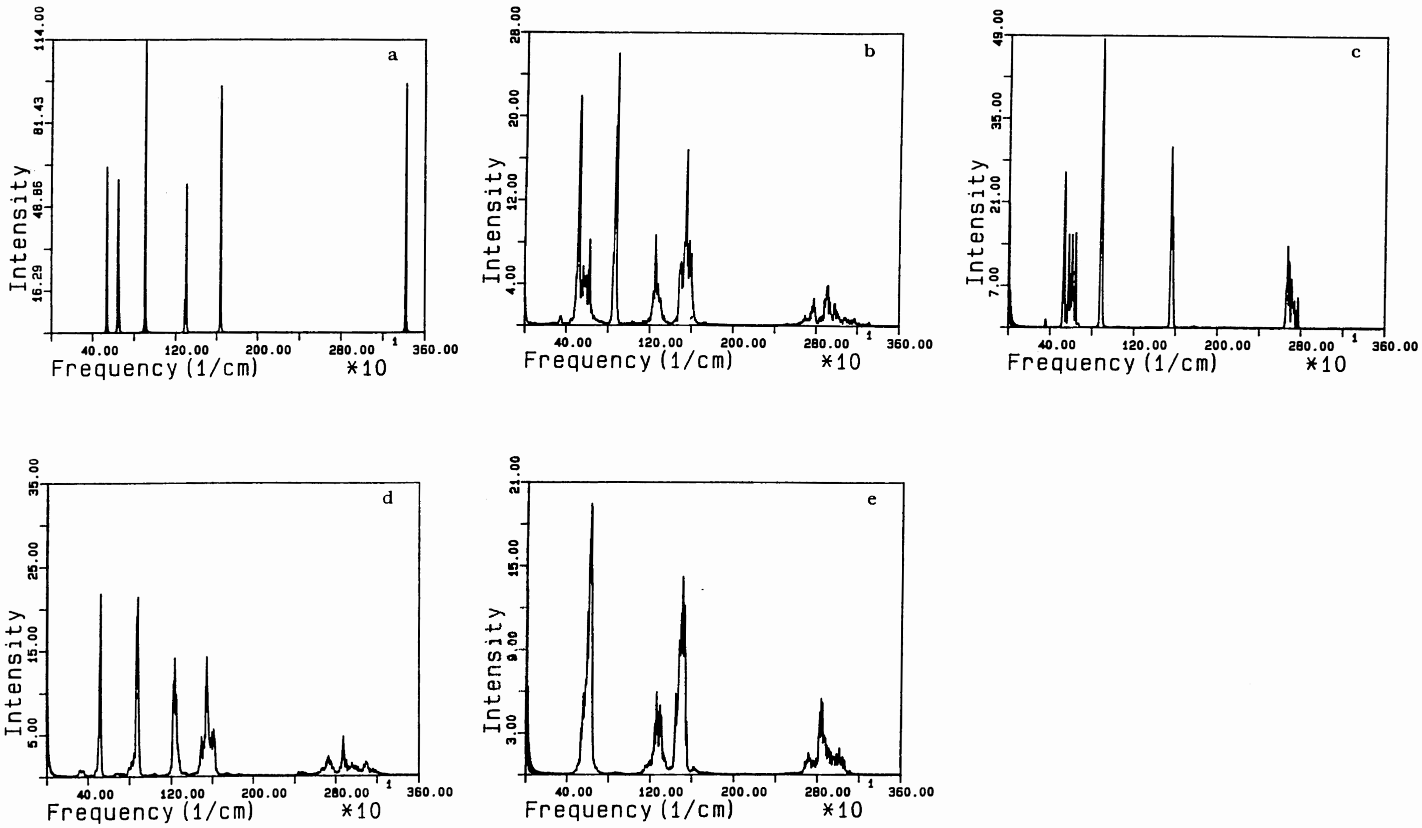

Figure 35. Power Spectra for an Ensemble of 30 Trajectories of Nonrotating *Cis*–HONO. (a) 0.5 kcal/mol Total Energy. (b) The OH Stretch is Initially Excited to the Second Overtones with 1.7 eV Total Energy. (c) Same as (b) Except the HON Bend is Constrained. (d) Same as (b) Except that the Torsional Motion is Constrained. (e) Same as (b) Except that the ONO Bending is Constrained.

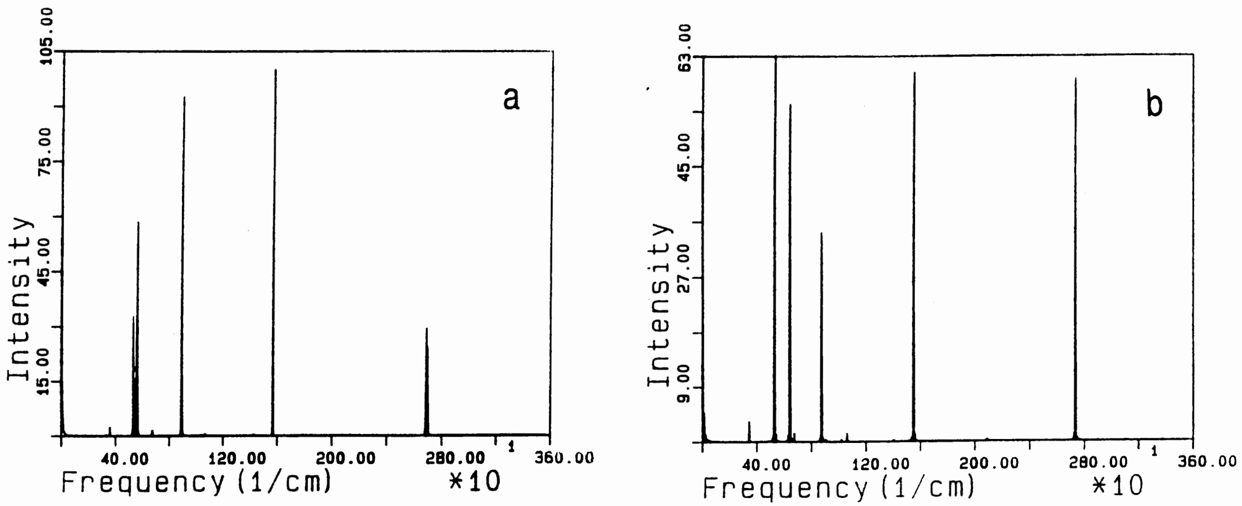

Figure 36. Power Spectra for a Single Trajectory of Nonrotating *Cis*–HONO. (a) The HON Bending Motion is Constrained and the OH Stretch is Initial Excited to the Second Overtones with 1.7 eV Total Energy, and Zero Angular Momentum. (b) Same as (a) Except Different Initial Vibrational Phases.

When the HON bending motion is constrained (see Fig. 35(c)) the width of the OH stretching band is much narrower. It is about 1/3 the width of the OH band for unconstrained motion (see Fig. 35(b)). This suggests that the OH stretching motion becomes more quasiperiodic when the HON bend is constrained. The interactions between the N=O stretch, N-O stretch, and ONO bend are significantly restricted by constraining the HON bending mode. The OH stretching-HON bending interaction is the principal "gateway" for relaxation of an excited OH overtone. When the torsional motion is constrained (see Fig. 35(d)) two peaks, which correspond to the ONO bending (centered at 525 cm^{-1}) and N-O stretching modes (centered at 879 cm^{-1}), respectively, are much narrower. That is, the interaction between the ONO bend and N-O stretch as well as the rest of the molecule is significantly decreased by constraining the torsional motion.

The frequencies of some of the vibrations decrease with increasing energy due to anharmonicity in the potential-energy surface. For a Morse oscillator, the effective frequency is given by[82]

$$\nu = \nu_0 \sqrt{1 - \frac{E_{vib}}{D_e}} \qquad \text{(VI–6)}$$

where the ν_0 is the fundamental vibrational frequency, E_{vib} is the total energy in the oscillator, and D_e is the depth of the potential. For excitation of the OH stretch to $v_{OH}=3$, the expected effective frequency is 2681 cm^{-1}. The computed value (Fig. 35(c)) is 2673 cm^{-1}. Power spectra of individual trajectories in which the HON bending motion is constrained (see Fig. 36(a) and 36(b)) show that the bands corresponding to the ONO bending, N-O stretching, and N=O stretching modes (535, 890, and 1560 cm^{-1}, respectively) do not shift appreciably between independent trajectories. However, the spectra for the torsional and OH stretching modes exhibit considerable frequency shifts from one trajectory to another. This effect may be due in part to slight differences in the initial excitation of these two anharmonic coordinates. The method of initial excitation employed results in minor differences in the mode energies for the trajectories. The level of excitation (and anharmonicity) in the OH stretch is such that these relatively small differences result in some frequency shifts. Similar considerations also apply to the torsion, where the anharmonicity is quite large. The levels of excitation of the remaining modes are such that such anharmonic effects are not important. We observe two small sharp peaks centered at 579 and 619 cm^{-1}, respectively; these correspond to the torsional mode due to different initial conditions.

When the ONO bend is constrained the resulting spectrum (Fig. 35(e)) is similar to that obtained when the torsional motion is constrained (Fig. 35(d)). There are no peaks in the range 700 to 900 cm^{-1} (the region where the N-O stretch would appear) in Fig. 35(e) even though the constraint is applied to the ONO bend only. Examination of the power spectrum of the N-O bond reveals that the band corresponding to the N-O stretch is shifted to 620 cm^{-1}, which coincides wtih the band due to the torsional motion. This indicates that the motion of the N-O stretch is somehow altered due to the ONO bending constraint. However, the reason for this shift is unclear. The rate of energy flow out of the OH stretch is more hindered when the ONO bend is constrained than when the torsional motion is constrained. This is evidenced by both the relative average rates of OH relaxation in the case of ONO bending and torsional constraints (Fig. 33a, upper curve, and Fig. 34b, respectively) and the narrower width of the OH stretching band for the case of ONO constraint (Fig. 35(e)) as compared to that for constrained torsional motion (Fig. 35(d)).

In general, the characteristics of the spectra are consistent with the OH relaxation results discussed above. Once the energy of the initially excited OH stretch flows to the HON bending mode, the couplings between the HON mode and the remaining vibrational modes facilitate continued energy transfer until the relaxation of the OH stretch is complete.

Isomerization Calculations

The rates of *cis-trans* isomerization in non-rotating HONO were computed by fitting Eq. (II-54) for various initial energy distributions. The ONO and HON bending motions were constrained to determine their roles in the isomerizations. The total energy was fixed at 1.7 eV in all cases.

The rate constants computed using trajectories in which the HON bending motion was constrained are given in Table XIX.

TABLE XIX

COMPUTED ISOMERIZATION RATE CONSTANTS WITH CONSTRAINED HON BEND

Initial energy distribution					k (ps^{-1})	
v_{OH}	$v_{N=O}$	v_{N-O}	v_{NON}	v_τ	*cis→trans*	*trans→cis*
1	2	4	7	0	0.027	0.017
0	6	0	0	0	**	**
0	5	0	0	1	0.053	0.025
0	0	10	0	0	0.067	0.014
0	0	0	16	0	0.051	0.024

** No isomerization was observed in an ensemble of 60 trajectories of 4.7 ps duration.

The levels of excitation of the various modes is such that there is approximately the same excitation energy in each case. The first row gives the results for *cis→trans* and *trans→cis* isomerizations for initial conditions in which each of the normal modes (except the torsion, which has only ZPE) has approximately the same energy. The other results in Table XIX are for excitations to the levels indicated. The rates in all cases are significantly smaller (as much as an order of magnitude) than when the HON bend is not constrained (see Table VI of Ref. 52). For example, the rate of *cis→trans* isomerization for the "uniform" distribution of energy among the various modes of the molecule is only 0.03 ps^{-1} when the HON bend is constrained (Table XIX) compared to 0.9 ps^{-1} when it is not (Ref. 52). In our earlier study, in which all motions were allowed, we found large differences (as much as a factor of 22) in the rates of *cis→trans* and *trans→cis*, however, as the results in Table XIX show, when the HON bend is constrained the rates for the two processes are in closer agreement; the greatest difference (a factor of about 5) is for $\nu_{N\text{-}O}$ = 10. The kinetic coupling in the *cis* conformer is much greater than in the *trans*.[52,53] Freezing the HON bend significantly reduces the coupling. This would suggest that the major factor in the differences in the rates for the two processes is due to kinetic coupling involving the HON bend.

The mode selectivity in the isomerizations is significantly diminished when the HON bending motion is constrained. For example, the rate decreases by a factor of 14 when the excitation energy is initially localized in the N=O stretching mode compared with equipartitioning of the excitation energy in the case of *cis→trans* conversion when all motions are allowed,[52] whereas the rates differ by only about a factor of two (and, in the opposite direction!) when the HON bending motion is constrained (see Table XIX). There is a major qualitative change in the mode selectivity when the $\nu_{N=O}$ mode is excited; no isomerization was observed unless the ν_τ mode was assigned energy above the ZPE. The HON bend plays a role in the energy transfer between the torsion, the N-O stretch, the ONO bend.

The computed rate constants for constrained ONO bending are given in table XX.

TABLE XX

COMPUTED ISOMERIZATION RATE CONSTANTS WITH CONSTRAINED ONO BEND

Initial energy distribution					k (ps^{-1})	
v_{OH}	$v_{N=O}$	v_{HON}	$v_{N\text{-}O}$	v_{τ}	*cis→trans*	*trans→cis*
1	2	3	4	0	0.22	0.019
0	6	0	0	0	0.037	**
0	0	8	0	0	0.84	0.080
0	0	0	10	0	0.047	**

** No isomerization was observed in an ensemble of 60 trajectories of 4.7 ps duration.

Constraining the ONO bending motion has much less effect than does constraining the HON bending. There is some reduction in the magnitudes of the rates compared with the results for no constraints (see Table VI, Ref. 52). Furthermore, the processes show mode selectivity. For example, excitation of the HON bend gives rates significantly larger than does other excitations, as is the case for unconstrained dynamics.[52] Also, there are large differences in the rates of *cis→trans* and *trans→cis*. The results are not significantly affected by constraining this mode; it plays a minor role in the dynamics of the molecule.

Summary

We have investigated the roles of the various vibrational modes and molecular rotation on the IVR and *cis-trans* isomerization by dynamically constraining (by incorporating Lagrangian multipliers into Hamilton's equations of motion) the dihedral, HON bending, or ONO bending angle.

The effects of constraining the torsional and bending modes on the relaxation of the OH bond stretching, initially excited to the second overtone state, was studied. The results show that the ONO bending and torsional motions play important roles in the relaxation following an initial stage of the energy flow from the OH stretch. The initial energy transfer occurs via OH-HON stretch-bend coupling. When the HON bending motion is constrained almost no energy is lost from the OH stretching mode during the 4.5 ps that the trajectories were followed, whether or not the molecule is rotating. The interaction between the OH stretching and HON bending modes is intimately involved in the relaxation of the OH overtone. The influence of the ONO bending on the OH overtone relaxation is much less than that of the HON. However, the interaction between the in-plane ONO and HON bending modes is stronger than that of the HON bending mode with the out-of-plane torsion.

The influence of rotation and the effect of constraining the torsional mode on the relaxation of the OH overtone were investigated. Constraining the torsional motion in HONO when it is not rotating causes a significantly slower rate of energy transfer after about 0.5 ps. There is little effect during that initial period. Only about one-half as much energy flows out of the OH stretching mode in 4.5 ps when the torsional mode is constrained as does when it is active. The similar rates of energy transfer in the first 0.5 ps illustrates that the torsional mode is not involved in the initial relaxation of the OH stretch, but plays a role once other modes become populated. The initial step in the relaxation involves transfer of energy to the HON bend, followed by transfer involving the ONO bending, torisonal, or N-O stretching modes. Constraining the torsional motion eliminates the influence of rotation on the IVR.

The coupling between the HON bending and out-of-plane torsion modes is a major factor in causing *cis*-HONO to isomerize at significantly greater rates than *trans*-HONO.[52] Molecular rotation significantly enhances intramolecular vibrational energy redistribution (IVR), however, it has little effect when the torsional coordinate is constrained to its equilibrium value. The rate constants computed using trajectories in which the HON bending motion was constrained are significantly smaller (by as much as an order of magnitude) than when the HON bend is active.[52] The effect is greater in the case of *cis*→*trans*. The effect of constraining the HON bend is to decrease the magnitudes of the rates and also to diminish the mode selectivity. Constraining the ONO bending motion has much less effect than does constraining the HON bending, and mode selectivity is still present.

CHAPTER VII

CONCLUSIONS AND FUTURE WORK

We have studied the *cis–trans* interconversions in HONO and HSiOH by using classical trajectories with semiclassical tunneling corrections. The intramolecular energy transfer, tunneling effects, and the isomerization rates are investigated. Several factors associated with the tunneling rate such as the potential energy surface, the effective mass in the tunneling coordinates, the rate of the energy flow from bath modes to the tunneling modes, as well as the times between turning points of the tunneling coordinates are examined. Significant mode specific behavior is found in both these systems.

The rate coefficients for *cis→trans* isomerization are generally larger than those for *trans→cis* for HONO isomerization processes. The excitations of the OH stretch and N=O stretch yield the slowest *cis→trans* and *trans→cis* isomerization rates in HONO, while the excitations of the N-O stretch give the largest rate coefficients for both *cis→trans* and *trans→cis* isomerization in HONO. Tunneling effects are not negligible in the interconversion of HONO. The largest ratio of the classical-plus-tunneling rate to the classical rate is 3. The rate of the energy transfer from the bath modes to the tunneling mode is found to be a dominant factor in the tunneling rate. The more the energy flows into the tunneling mode from bath modes, the larger the tunneling probability. When the rates of the energy transfer between the bath modes and the tunneling mode are slow, the magnitude of the tunneling probability is directly associated with the value of effective mass of the torsional mode (tunneling mode).

Similar behaviors are found in the isomerization processes of HSiOH. The Si-O stretch excitation yields the largest the rate constants and the OH stretch excitation yields the smallest rate constants for both *cis–>trans* and the reverse process of HSiOH. The tunneling effects play an important role in the HSiOH interconversion. When the total energy of the system is 20 kcal/mol, the largest ratio of the rate coefficient with and without tunneling correction, k_{C+T}/k_C, is equal to 7.3 for the *cis–>trans*. The tunneling effects are even more important in the process of *trans–>cis* than that of *cis–>trans*. The tunneling via HOSi in-plane bending mode is found to be an important factor. The "branching radio" k_{HOSi}/k_τ is significantly larger for *cis–>trans* isomerization than for the *trans–>cis*. The efficient intramolecular transfer between the HOSi in-plane bending mode to the rest of the vibrational modes of the HSiOH significantly increases the tunneling via HOSi bending. The rates of the mode-to-mode energy transfer between the the same symmetry group are significantly faster than those of the modes with different symmetry when the excitation energy is relatively low. The values of the effective mass along the tunneling coordinate will facilitate or hinder the tunneling probability. The HOSi bending coordinate, 1/G(HOSi, HOSi), are generally larger (about 2 to 4 $(au)^2$amu) than the values along the torsional coordinate (0.02 to 3 $(au)^2$amu). Therefore, the effective mass along the torsional coordinate, $1/G(\tau,\tau)$ facilitates the tunneling rate significantly. The ratio of the decay rate computed by including tunneling to that without tunneling increases with decreasing total energy of the system, and the branching ratio of k_{HOSi}/k_τ decreases with the increasing excitation energy. Furthermore, the rate difference between the *cis→trans* and *trans→cis* decreases with increasing the excitation energy. When the energy of the system reaches 30 kcal/mol or above, the tunneling effects becomes less significant and the isomerization rates obtained by including tunneling approach the rate without tunneling due to the large amount of classical "crossing" contribution. The ratio of the isomerization rate constants for the *cis→trans* to the reverse process also approaches unity with increasing total energy.

We have investigated the roles of the various vibrational modes and molecular rotation in intramolecular energy transfer and in *cis–trans* isomerizations of HONO by using constrained classical trajectories. The results elucidate the importance of the ONO bending and torsional motions for the relaxation of the excited OH stretch. The initial energy transfer occurs via OH-HON stretch bend coupling. When the HON bending motion is constrained almost no energy is dissipated from the OH stretching mode in our integration timescale (4.5 ps), whether the molecule is rotating or not. The influence of the ONO bending on the OH overtone relaxation is much less than that of HON. However, the kinetic coupling between the ONO and HON bending modes is much stronger than that of the HON bending mode with the out-of-plane torsion. Constraining the torsional motion causes a significantly slower rate of energy transfer after 0.5 ps. The torsional mode does not involve in initial relaxation of the OH stretch but it plays a role once other modes become populated. Constraining the torsional motion eliminates the influence of rotation on the intramolecular vibrational energy relaxation. The interaction between the out-of-plane torsional and HON bending modes is a major factor in causing *cis*–HONO to isomerize at significantly greater rates than that of *trans*–HONO. The HON bending mode plays an important role for mode selectivity. The effect of constraining the ONO bending plays a much smaller role than does constraining the HON bending for decreasing magnitudes of the rate, and mode selectivity is still present.

The classical trajectory method has been demonstrated to be very useful tool. When the semiclassical tunneling treatment is incorporated into the classical trajectory method, it proves to be even more powerful in exploring the chemical reaction dynamics. We have employed this method to study the tunneling effects for isomerization processes of HONO and HSiOH. Noting that the potential energy surfaces used in our work are basically empirical, the tunneling rates are, however, strongly associated with the shape of the potential energy surfaces. It would be nice to have more accurate *ab initio* potential energy surfaces for our systems. Another problem associated with our calculations is that we were not able to test the accuracy of our calculations because only very limited theoretical studies have been carried out for our systems, even though our results are qualitatively in good agreement with some aspects of the experimental observations.

The constrained trajectories method used here has been demonstrated to be a useful approach to study the intramolecular energy transfer by introducing the Lagrangian multipliers into Hamilton's equations of motion to "remove" certain modes to determine their influence. Also we have studied the influence of rotation on the relaxation of overtones of OH local and normal modes. The main problem encountered is that our data cannot correspond to the experimental data directly because the real molecule is not rigid. Another unsatisfactory aspect of present work is that our results can only give some qualitative picture of the intramolecular energy transfer. The quantitative description of the intramolecular energy transfer is remains a challenge.

REFERENCES

1. G. C. Schatz, Ann Rev. Phys. Chem. **39**, 317 (1988); W. H. Miller, Chem. Rev. **87**, 19 (1987); G. C. Schatz, Chem. Rev. **87,** 81 (1987).

2. R. P. Bell, *The Tunnel Effects in Chemistry* (Chapman and Hall, New York, 1980).

3. D. Rapp, *Quantum Mechanics* (Holt, Rinehart, and Winston, Dallas, 1971); Nanny Froman and Perolof Froman *JWKB Approximation Contributions to the Theory* (North-Holland Publishing Company, Amsterdam, 1965).

4. D. G. Truhlar, A. D. Isaacson, and B. G. Garrett in: *Theory of Chemical Reaction Dynamics* , Vol. 4, ed. M. Baer (CRC Press, Boca Raton 1985).

5. E. Wigner, Z. Phys. Chem. B **19**, 203 (1932).

6. R. P. Bell, Trans. Faraday Soc. **55**, 1 (1959).

7. R. A. Marcus and M. E. Coltrin, J. Chem. Phys. **67**, 2607 (1977).

8. W. H. Miller, N. C. Handy, and J. E. Adams, J. Chem. Phys. **72**, 99 (1980).

9. R. A. Marcus, J. Chem. Phys. **46**, 959 (1967); R. E. Wyatt, J. Chem. Phys. **51**, 3489 (1969); D. G. Truhlar, J. Chem. Phys. **53**, 2041 (1976).

10. S. K. Gray, W. H. Miller, Y. Yamaguchi, and H. F. Schaefer III, J. Chem. Phys. **73**, 2733 (1980).

11. S. K. Gray, W. H. Miller, Y. Yamaguchi, and H. F. Schaefer III, J. Am. Chem. Soc. **103**, 1900 (1981).

12. S. M. Colwell and N. C. Handy, J. Chem. Phys. **82**, 1281 (1984).

13. R. T. Skodje, D. G. Truhlar, and B. G. Garrett, J. Phys. Chem. **85**, 3019 (1981); R. T. Skodje, D. G. Truhlar, and B. G. Garrett, J. Chem. Phys. **77**, 5955 (1982).

14. W. H. Miller, J. Phys. Chem. **83**, 960 (1979).

15. G. Herzberg, *Molecular Spectra and molecular Structure* II (van Nostrand, Princeton, 1945), p 223.

16. F. B. Brown, S. C. Tucker, and D. G. Truhlar, J. Chem. Phys. **83**, 4451 (1985).

17. B. C. Garrett and D. G. Truhlar, J. Chem. Phys. **79**, 4931 (1983).

18. G. C. Lynch, D. G. Truhlar, and B. G. Garrett, J. Chem. Phys. **90**, 3102 (1989).

19. J. G. Lauderdale and D. G. Truhlar, J. Chem. Phys. **84**, 4843 (1985).

20. B. M. Rice, L. M. Raff, and D. L. Thompson, J. Chem. Phys. **88,** 7221 (1988).

21. B. C. Garrett, D. G. Truhlar, A. F. Wagner, and T. H. Dunning, J. Chem. Phys. **78**, 4400 (1983); B. C. Garrett , N. Abusalbi, D. J. Kouri, and D. G. Truhlar, J. Chem. Phys. **83**, 2252 (1985).

22. T. Carringtom and W. H. Miller, J. Chem. Phys. **84**, 4364 (1986).

23. S. L. Baughcum, R. W. Duerst, W. F. Rowe, Z. Smith, and E. B. Wilson, J. Am. Chem. Soc. **103**, 6296 (1981); S. L. Baughcum, Z. Smith, E. B. Wilson, and R. W. Duerst, J. Am. Chem. Soc. **106**, 2260 (1984).

24. M. J. Frisch, A. C. Scheiner, H. F. Schaefer, and J. S. Binkley, J. Chem. Phys. **82** 4194 (1985).

25. N. Shida, P. F. Barbara, and J. E. Almlof, J. Chem. Phys. **91**, 4061 (1989).

26. E. Bosch, M. Moreno, J. M. Lluch and J. Bertran, J. Chem. Phys. **93**, 5685 (1990).

27. L. M. Raff and D. L. Thompson in: *Theory of Chemical Reaction Dynamics* , Vol. 3, ed. M. Baer (CRC Press, Boca Raton 1985).

28. B. A. Waite and W. H. Miller, J. Chem. Phys. **73**, 3713 (1980).

29. B. A. Waite, J. Phys. Chem. **88**, 5076 (1984).

30. J. M. G. Llorente and E. Pollak, Chem. Phys. **120**, 37 (1988); J. M. G. Llorente and E. Pollak in : *The Structure of Small Molecules and Ions* , ed. R. Naaman and Z. Vager (Plenum Press, New York , 1987).

31. A. Carrington and R. A. Kennedy J. Chem. Phys. **81**, 91 (1984); A. Carrington, J. Chem. Soc. Faraday Trans. II **82**, 1089 (1986).

32. N. Makri and W. H. Miller, J. Chem. Phys. **91**, 4026 (1989).

33. A. J. Illies, M. F. Jarrold, and M. T. Bowers, J. Am. Chem. Soc. **104**, 3587 (1982); M. F. Jarrold, A. J. Illies, and M. T. Bowers, Chem. Phys. Lett. **92**, 653 (1982).

34. E. J. Heller and R. C. Brown, J. Chem. Phys. **79**, 3336 (1983).

35. R. K. Preston and J. C. Tully, J. Chem. Phys. **54**, 4297 (1971); J. C. Tully and Preston, ibid. **55**, 562 (1971).

36. A. Tachibana, H. Fueno, M. Koizumi, H. Teramae, T. Yamabe, and K. Fukui, J. Phys. Chem. **92**, 935 (1988); A. Tachibana, H. Fueno, M. Koizumi, and T. Yamabe, J. Am. Chem. Soc. **108**, 4346 (1986).

37. Z. K. Ismail, R. H. Huage, L. Fredin, J. K. Kauffman, and J. Margrave, J. Chem. Phys. **77**, 1617 (1982).

38. T. Kudo and S. Nagase, J. Phys. Chem. **88**, 2833 (1984).

39. S. Sakai and K. D. Jordan, Chem. Phys. Lett. **130**, 103 (1986).

40. W. Siebrand, T. A. Wildman, and M. Z. Zgierski, J. Am. Chem. Soc. **106**, 4083 (1984); W. Siebrand, T. A. Wildman, and M. Z. Zgierski, J. Am. Chem. Soc. **106**, 4089 (1984);

41. T. Miyazaki and K. Lee, J. Phys.Chem. **90**, 400 (1986).

42. W. C. Gardiner, *Combustion Chemistry* (Springer-Verlag, New York, 1984); S. W. Benson and P. S. Nangia, Acc. Chem. Rev. **12**, 223 (1979).

43. D. C. Robie, S. Arepalli, N. Presser, T. Kitsopoulos, and R. J. Gordon, Chem. Phys. Lett. **134**, 579 (1987).

44. I. D. Reid, D. M. Lee, L. Y. Senba, D. J. Arseneau, and D. G. Fleming, J. Chem. Phys. **86**, 5578 (1987).

45. G. C. Schatz, J. Chem. Phys. **83**, 3441 (1985); D. M. Garner, D. G. Fleming, and R. J. Mikula, Chem. Phys. Lett. **121**, 80 (1985).

46. B. G. Garrett and D. G. Truhlar, J. Chem. Phys. **81**, 309 (1984).

47. N. J. Kirchner and M. T. Bowers, J. Phys. Chem. **91**, 2573 (1987).

48. J. D. Baldeschwieler and G. C. Pimental, J. Chem. Phys. **33**, 1008 (1960).

49. R. T. Hall and G. C. Pimental, J. Chem. Phys. **38**, 1889 (1963).

50. P. A. McDonald and J. S. Shirk, J. Chem. Phys. **77**, 2355 (1982); A. E. Shirk and J. S. Shirk, Chem. Phys. Lett. **97**, 549 (1983).

51. J. A. Darsey and D. L. Thompson, J. Phys. Chem. **91,** 3168 (1987).

52. Y. Guan, G. C. Lynch, and D. L. Thompson, J. Chem. Phys. **87**, 6957 (1987).

53. Y. Guan and D. L. Thompson, Chem. Phys. **139**, 147 (1989).

54. Y. Qin and D. L. Thompson, J. Chem. Phys., accepted.

55. J. M. Coffin and Peter Pulay, J. Phys. Chem. **95**, 118 (1991).

56. J. Murto, M. Rasanen, A. Aspiala, and T. Lotta, J. Mol. Struct. **122**, 213 (1985).

57. H. Goldstein, *Classical Mechanics*, (Addison-Wesley Publishing Company, Inc., Reading, Mass.), 1980.

58. E. B. Wilson Jr., J. C. Decius, and P. C. Cross, *Molecular Vibrations*, (Dover, 1980).

59. S. Califano, *Vibrational States*, (John Wiley and Sons, London, 1976).

60. W. H. Miller, W. L. Hase, and C. L. Darling, J. Chem. Phys. **91**, 2863 (1989).

61. K. L. Bintz, D. L. Thompson, and J. W. Brady, J. Chem. Phys. **85,** 1848(1986); Chem. Phys. Lett. **131**, 398 (1986); K. L. Bintz, M.S. Thesis, Oklahoma State University, 1986.

62. C. S. Sloane and W. L. Hase, J. Chem. Phys. **66**, 1523 (1977); W. L. Hase, D. G. Buckowski , and K. N. Swamy, J. Phys. Chem. **87**, 2754 (1983).

63. W. H. Miller, Adv. Chem. Phys. **25**, 69 (1974).

64. J. Jellinek and D. J. Kouri, in : *Theory of Chemical Reaction Dynamics*. Vol. 2, ed. M. Baer (CRC Press, Boca Raton, 1985), p 1; E. Pollak, Chem. Phys. Lett. **111**, 473 (1984).

65. C. E. Bolm and P. Pulay, Mol. Phys., **39**, 1537 (19080); P. Pulay, in: *Vibrational Spectra & Structure* , ed. James R Durig (Elsevier, Amsterdam, 1985), Vol. **14**, p 146-150.

66. General dynamics Code written by Karen and co-workers, see ref. 61.

67. L. M. Raff, J. Chem. Phys. **89**, 5680 (1988); L. M. Raff, J. Chem Phys. **90**, 6313 (1989).

68. J. I. Steinfeld, J. S. Francisco and W. L. Hase, *Chemical Kinetics and Dynamics* , (Pretice-Hall Inc., 1989).

69. T. D. Sewell and D. L. Thompson, J. Chem. Phys. **93**, 4077 (1990); T. D. Sewell and D. L. Thompson, J. Phys. Chem. **95**, 6228 (1991).

70. R. Roy, B. G. Sumpter, G. A. Pfeffer, S. K. Gray, and D. W. Noid, Phys. Lett. **205**, 109 (1991); B. G. Sumpter and D. L. Thompson, J. Chem. Phys. **86**, 2805 (1987); D. W. Noid, M. L. Koszykowski, and R. A. Marcus, Annu. Rev. Phys. Chem. **32**, 267 (1981)

71. J. S. Bendat and A. G. Piersol, in *Measurment and Analysis of Random Data* (Wiley, New York, 1971).

72. See, for example, A. Papoulis, *Probability, Random Variables, and Stochastic Processes* (McGraw–Hill, New York, 1965).

73. See, for example, D. G. Truhlar, R. Steckler, and M. S. Gordon, Chem. Rev. **87**, 217 (1987); S. Dasgupta and W. A. Goddard III, J. Chem. Phys. **90,** 7207 (1989).

74. B. G. Sumpter, D. W. Noid, and B. Wunderlich, J. Chem Phys. **93**, 6875 (1991); C. Getino, B. G. Sumpter, and J. Santamaria, Chem. Phys. **145**, 1 (1990); R. J. Wolf, D. S. Bhatia, and W. L. Hase, Chem. Phys. Lett. **132**, 1339 (1986); B. G. Sumpter and D. L. Thompson, J. Chem. Phys. **87**, 5809 (1987).

75. R. Walsh, Acc. Chem. Res. **14**, 246 (1981).

76. P. V. R. Schleyer and D. Kost, J. Am. Chem. Soc. **110**, 2105 (1988).

77. J. M. Bowman, B. Gazdy, and Q. Sun, J. Chem. Phys. **91**, 2859 (1989);

78. T. D. Sewell, D. L. Thompson, W. H. Miller, and D. Gezelter, in preparation.

79. G. E. McGraw, D. L. Bernitt, and I. C. Hisatsune, J. Chem. Phys. **45**, 1392 (1966).

80. L. G. Spears, Jr. and J. S. Hutchinson, J. Chem. Phys. **88**, 240 (1988); *ibid*. **88**, 250 (1988).

81. Y Qin and D. L. Thompson (manuscript in preparation).

82. D. W. Oxtoby, S. A. Rice, J. Chem. Phys. **65**, 1676 (1976).

VITA 2

Yue Qin

Candidate for the Degree of

Doctor of Philosophy

Thesis: SEMICLASSICAL TUNNELING CORRECTIONS FOR CLASSICAL DYNAMICS OF UNIMOLECULAR REACTIONS IN POLYATOMIC MOLECULES

Major Field: Chemistry

Biographical:

Personal Data: Born in Wuhan, P. R. China, March 27, 1958, the son of Baoshun Qin and Chaoping Zhang.

Education: Graduated from the First High School of Chen Jiang Conty, Yunnan, in August, 1975; Received Bachelor of Science Degree in Chemistry from Wuhan University in January, 1982; Received Master of Science Degree in Physical Chemistry from Jilin University in July, 1986; Completed requirements for the Doctor of Philosophy Degree at Oklahoma State University in May, 1992.

Professional Experience: Teaching Assistant, Department of Chemistry, Oklahoma State University, January, 1987 to December, May, 1989; Research Assistant, Department of Chemistry, June, 1989, to May, 1992.